Technische Universität München

Physik Department E20

Molecular Nanoscience and Chemical Physics of Interfaces

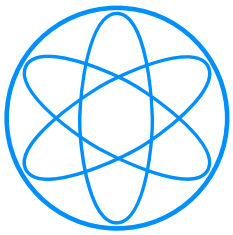

Two-dimensional nanoporous molecular networks: growth, dynamics and electron confinement

Dissertation

Nenad Kepčija

TECHNISCHE UNIVERSITÄT MÜNCHEN

Lehrstuhl E20 -
Molekulare Nanowissenschaften & Chemische Physik von Grenzflächen

Two-dimensional nanoporous molecular networks: growth, dynamics and electron confinement

Nenad Kepčija

Vollständiger Abdruck der von der Fakultät für Physik der Technischen Universität München zur Erlangung des akademischen Grades eines Doktors der Naturwissenschaften (Dr. rer. nat.) genehmigten Dissertation.

Vorsitzender:	Univ.-Prof. Dr. Norbert Kaiser
Prüfer der Dissertation:	1. Univ.-Prof. Dr. Johannes Barth
	2. Priv.-Doz. Dr. Markus Lackinger

Die Promotion wurde am 13.11.2013 bei der Technischen Universität München eingereicht und durch die Fakultät für Physik am 06.12.2013 angenommen.

Mojim roditeljima,
za svu ljubav, podršku i odricanje

Abstract

Fabrication of nanoarchitectures, understanding of their properties and control over them represents a major challenge and requires knowledge of solid state physics, supramolecular chemistry and material sciences. In this dissertation three important aspects of two-dimensional, surface-confined nanoporous networks are examined: dynamics, growth and electron confinement.

Bi-molecular networks consisting of sexiphenyl-dicarbonitrile and N,N-diphenyl oxalic amide, which are coupled via two different bonding motifs of different strength, were found to exhibit intriguing dynamic behaviour: the one-dimensional (1D) diffusion of the molecules of the weaker bond sublattice is guided by the more stable multimolecular superstructure. Furthermore, threefold symmetric *de novo* synthesized molecules with terminal alkynes were investigated. For the first time it was shown how these building blocks can be linked by covalent bonding into nanoporous structures in two dimensions. Both the diffusion in bi-component networks and the formation of covalently bound templates are rationalized by computational modeling. A systematic study of the electron confinement and analysis of the band structures for different systems is also presented and an insight into the origin of the spectral line shapes could be gained.

Contents

List of Figures

1 Introduction

Nanotechnology and nanosciences were conceived in the late fifties, more precisely in 1959, when Richard Feynman - six years later a Nobel prize laureate - introduced the idea of creating novel materials by direct manipulation of atoms and molecules within his talk "There is a plenty of room at the bottom" [1]. Independently from Feynman, Eric Drexler gave the field its name, by inventing the term "nanotechnology" in his 1986 book "Engines of Creation: The Coming Era of Nanotechnology"[2]. Fabrication of nanoarchitectures, understanding of their properties and control over them represent a major challenge requiring knowledge of solid state physics, supramolecular chemistry and material sciences. A constantly growing amount of the information that has to be processed and stored provoked a need for ever smaller storage devices and electronic building elements.

For the manufacturing of the nanoscale entities two approaches are employed: top-down and bottom-up. These very general concepts were originally applied in the information processing [3] and knowledge structuring and were afterwards naturally transfered to the area of management and organization [4], as well as nanosciences [5]. The top-down approach denotes a stepwise designing of structures, which means that a system is detached into subsystems, which are analyzed after an overview of the compound entity is given. In terms of formal logic, this approach is referred to as a deductive, analytical reasoning, i.e. is a way of concluding, in which a set of quite general statements leads to a specific conclusion. The bottom-up

approach, on the contrary, is related to a synthetic design, where constitutive ingredients build up the entire system. This reasoning is inductive: based on the characteristics of components, the conclusion about the integral system is reached. In the language of the information processing and computing top-down approach describes an all-encompassing understanding of the system, whilst bottom-up assumes an early-stage coding and testing and a subsequent linking of different moduli [3]. In the field of management and organization we speak either about decisions made by a superordinate person, which is then distributed over lower-level coworkers (top-down) or a large number of colleagues actively involved into the decision process (bottom-up) [4].

Nanosciences provide quite similar description of the above mentioned terms: top-down represents decomposing of the system into smaller parts, e.g. lithography can be used to reduce bulk material down to nanoscale pattern. On the contrary, bottom-up approach means that devices and composite structures are constructed from smaller building blocks, for instance by means of molecular self-assembly [6]. Bearing in mind a rich manifold of the fabricated nanostructures, we can say that the self-assembly opens up new possibilities for their rational design [7]. In general, supramolecular chemistry has evolved into one of the most important approaches for the engineering of novel functional materials [8, 9, 7, 10].

Profound investigations in the recent years have shown that metal surfaces provide suitable ground for the exploration and controlling of the self-assembly processes, enabling nanoporous networks to be formed on them. Network formation is usually governed by a fine interplay of two kinds of interactions. The first interaction is the one between individual molecules and the substrate, which pins the molecules with a definite crystallographic position and orientation. The lateral intermolecular interaction comprises the molecules only and together with the substrate-molecule interaction is responsible for the molecular ordering and thus, for the symmetry of the network.

A key role in the molecular nanoarchitecture formation belongs to functional groups. These are groups of atoms, which determine chemical properties and characteristic reactions of the molecules. In purely organic networks the interaction among tectons is realized via either non-covalent or covalent bonds; if the networks encompass metal atoms as well, we speak about the metal-organic coordination. To date, a wide palette of functional groups has been employed. The self-assembly of the molecules with carboxylic end group was intensively studied in the past decade [11]. Also, the carbonitrile group was successfully utilized for constructing of nanoarchitectures [12]. Furthermore, the direct anchoring of functional groups to surfaces (functionalization) opens up new possibilities for changing of the surface properties and making them more applicable, e.g. for hydrophilic coating for contact lenses [13]. The functional groups covalently link molecules, nanoparticles, proteins and DNA to the surface of metals or biochemical devices. A systematic, year-long investigation in the area of supramolecular chemistry yields hope for potential applications: as molecular switches and machines [14, 15, 16, 17], as sensors [18, 19, 20], for hydrogen storage [21], molecular recognition [22, 23] or in the field of nanomagnetism [24, 25, 26].

In the majority of the produced and studied supramolecular structures the non-covalent bonding is a prevalent type of bonding, i.e. hydrogen bond, $\pi - \pi$ interactions and van der Waals forces. The hydrogen bond is an attractive, directional interaction resulting from sharing a proton between an hydrogen donor (X-H) and a hydrogen acceptor (A) group. It is represented in a wide variety of organic molecules e.g. polymers, proteins, DNA (thymine and adenine are connected via an H-bridge; the same holds for guanine and cytosine). In the very recent time, a special type of bonding is characterized as a proton-acceptor ring interaction (PARI) [27] and the on-surface covalent linking of acetylenes was successfully implemented [28], which will be further referenced throughout this dissertation.

The most effective and most instructive way to research nanoarchitectures at the metal surfaces is scanning tunneling microscopy, which is closer explained in the next chapter. It enables insight into the morphology of clusters, surfaces and interfaces, as well as the conclusions draw on the electronic structure, based on the scanning tunneling spectroscopy. The picometer precision in the positioning of the tip renders possible to move single molecules with distinct manipulation protocols [29]. All mentioned possibilities that STM offers, represent in fact routes towards realization of the main ideas from the Feynman's lecture.

For the adequate utilization of objects from the nanoworld as compounds of machines and circuits, it is extremely important to investigate their electronic properties. In the context of the band structure, it is essentially to study surface states, arising from the symmetry breaking on the border between bulk material and vacuum. They were identified by Gartland and Slagsvold [30] by the angle resolved photo-emission spectroscopy (ARPES) and then in the coming period a series of theoretical and experimental works have illuminated more and more the physics of the surface states [31, 32, 33, 34]. It turns out that very often the length of constitutive molecules plays a decisive role in the positioning of the peaks in the local density of states of the entire network, which means that some conductivity characteristics can be achieved by varying the single molecule length. Again, the altering of the band structures of purely organic networks is feasible through adding metal coordination atoms.

In this dissertation three crucial aspects of the supramolecular networks are illuminated: growth, dynamics and electron confinement. For the first time it was shown how building blocks made of terminal alkynes can be linked by covalent bonding into nanoporous templates in two dimensions. Dynamics of bi-component networks were studied, as well as the diffusion of theirs constituent molecules that take place in such configuration. I provided a systematic study of the electron confinement for various metal surfaces and on top lying molecules.

The dissertation is organized as follows: in the second chapter experimental and theoretical methods are listed and explained, with the emphasis on the scanning tunneling microscopy. A summary of the basic concepts of the solid state physics, required for understanding of the surface states, theory of the states themselves and the solving of the Schrödinger equation for a potential barrier are given in the Chapter 3. Chapter 4 deals with a bimolecular ladder network and the diffusion processes that take place in it. A two-step protocol and two binding motifs are shown, as well as the rationalization of the network creation through the DFT calculations. In the fifth Chapter the self-assembly of the networks consisting of the molecules with terminal alkynes was analysed. I investigated two different types of molecules, phases that they build within the networks and the stability of such an ordering. Covalent bonding of the terminal alkynes is studied in the Chapter 6, where the STM, XPS and DFT data were combined, in order to gain a complete picture of a novel, planar binding motif. Quantum confinement in honeycomb nanoporous networks and the influence of particular network constituents, the band structure of the respective systems, as well as the possibilities to control and tune the electronic properties are thoroughly studied in Chapter 7. In the conclusion chapter, Chapter 8 I gave a summary of the thesis with possible implications on the future of the nanosciences.

2 Experimental And Theoretical Methods

2.1. Scanning Tunneling Microscopy

Scanning Tunneling Microscopy is a powerful technique for the imaging and investigation of surfaces with atomic resolution. The very first topographic images were obtained 1982 by Binnig and Rohrer in the IBM research laboratory in Zürich, Switzerland. Four years later in 1986, they were awarded the Nobel Prize in Physics. The discovery of the STM and scanning tunneling spectroscopy (STS) represents a groundbreaking step that opened up new vistas for the exploring of microscopic systems and enabled a deeper understanding of nanoscale phenomena. A big advantage of the STM is that this technique is reliable under a very wide spectrum of conditions - it can be used both in ultra-high vacuum (UHV) and under standard pressure, the temperature range varies from low temperatures (typically 5 K) up to few hundreds degrees Celsius. Apart from solid inter- and surfaces, STM suits very well for solid-liquid interfaces.

In order to understand how the STM works, it is necessary to get acquainted with its quantum mechanical background. The first concept, that I am going to deal with is the concept of tunneling.

2.1.1. Quantum mechanical tunneling

Quantum tunneling refers to the propagation of a particle through a potential barrier, which is not allowed by the laws of classical mechanics. Namely, in the classical picture the total energy E of an electron is described by the formula

$$E = \frac{p^2}{2m} + U(z), \tag{1}$$

where m is the electron mass, p classical momentum, $U(z)$ is the potential energy. As long as $E > U(z)$ holds, the electron possesses a non-negative momentum $p = \sqrt{2m(E - U(z))}$. If the energy of the electron is less than $U(z)$, it can not penetrate into that region. On the other hand, in quantum mechanics the motion of the electron is described by the Schrödinger equation

$$-\frac{\hbar^2}{2m}\frac{d^2}{dz^2}\psi(z) + U(z)\psi(z) = E\psi(z). \tag{2}$$

In the classical region solutions have the form of plane waves

$$\psi(z) = \psi(0)e^{\pm ikz} \tag{3}$$

where k, the wave vector equals $k = \frac{\sqrt{2m(E-U)}}{\hbar}$. From here it appears that the electron can move either in positive or negative direction of the z-axis with a momentum $p = \hbar k$ and velocity $v = \frac{p}{m}$, which corresponds to the classical case. In the region with $E < U(z)$ the solutions are given by an exponential function

$$\psi(z) = \psi(0)e^{\pm\kappa z}, \tag{4}$$

with $\kappa = \frac{\sqrt{2m(U-E)}}{\hbar}$. The function with the minus sign describes propagation of the electron through the barrier in the positive z-direction, while the plus sign depicts a decay in the negative direction. The probability for the electron to be found in a z position is $|\psi(z)|^2$, i.e. $|\psi(0)|^2 e^{-2\kappa z}$, thus non-zero in the barrier region, which means that the electron has a finite probability to tunnel through the barrier, although its energy lies lower.

Already this elementary model is good enough to describe basics of the metal-vacuum-metal tunneling. For that purpose it is convenient to consider the *work function* ϕ. This is the minimal energy required to remove an electron from the bulk to a very large distance from it or, equivalently, from the Fermi level to the vacuum. It is not only a characteristics of the material, but also depends on the surface properties (crystallographic orientation). The Fermi level is the highest level occupied by the electrons. If the vacuum level is the reference point of energy, one can write $E_F = -\phi$. Without the loss of generality we will suppose that both the tip and the sample have the same work functions. The tunneling can occur from the tip to the sample and vice versa. It is realized by applying a small bias voltage V, which enables tunneling current to flow. Only the states ψ_n with the energies E_n in the range from E_F and $E_F - eV$ have a chance to undergo tunneling. If we assume that the bias is much less than the work function ($eV \ll \phi$), then the energy of the tunneling states E_n is in the neighbourhood of ϕ. In other words, only the states around Fermi level are relevant for this process, Typically, one defines also a *transmission coefficient* T as a ratio of the current on the tip surface z to the current at $Z = 0$,

$$T = \frac{I(z)}{I(0)} = e^{-\kappa z}, \kappa = \frac{\sqrt{2m\phi}}{\hbar}. \tag{5}$$

Since only for a limited number of potential barriers it is possible to analytically solve the Schrödinger equation and therefore to compute the transmission coefficient T, many approximative methods were developed. One of the best-known is the Wentzel-Kramers-Brillouin (WKB) approximation. Here T is expressed as an integral of the decay rate $\kappa(z) = \frac{\sqrt{2m(U(z)-E)}}{\hbar}$ as $T = e^{-2\int_{z_1}^{z_2} \kappa(z)\, dz}$. This expression reduces easily to Eq. 42 by applying it to a square potential barrier (see below).

2.1.2. Bardeen theory and WKB approximation

One of the most widely employed theories of the tunneling phenomenon and STM is the Bardeen's transfer Hamiltonian Ansatz. Originally it was developed to make a connection between the energy spectrum of the superconductor and experimental findings by Giaever [35, 36]. The spectrum was predicted by the Bardeen-Cooper-Schrieffer (BCS) theory of the superconductivity [37], whilst the experiments were performed on metal-insulator-metal (MIM) tunneling junctions in order to verify the BCS theory. The MIM junction consists of an Al and Pb piece with an insulating film of sapphire in crystalline form in between. The main idea in the approach to the problem of the MIM junction is to solve the Schrödinger equation not for the whole system, but to treat it as two separate subsystems. It turns out that the amplitude of electron transfer or the matrix element M is determined by a surface integral of the unperturbed wave functions of the two subsystems at a separation surface. In the simpliest case of planar tunnel junctions this surface is only a plane between the electrodes at an arbitrary position. If M is almost constant in the observed energy range, then the tunneling spectrum is given as a convolution of the density of states of the two electrodes.

$$I \propto \int_o^{eV} \rho_A(E_F - eV + \epsilon)\rho_B(E_F + \epsilon)d\epsilon \tag{6}$$

The starting point of Bardeen's tunneling theory is that the two sets of wave functions are only approximately orthogonal,

$$\int \psi_\mu^* \chi_\nu d^3\vec{r} \approx 0 \tag{7}$$

With help of a definition of the tunneling matrix element as

$$M_{\mu\nu} = \int_{z>z_0} \psi_\mu U_B \chi_\nu^* d^3\vec{r} \tag{8}$$

one can derive an explicit formula for the tunneling current. Under assumption that the tunneling is elastic, i.e. a state from one electrode can

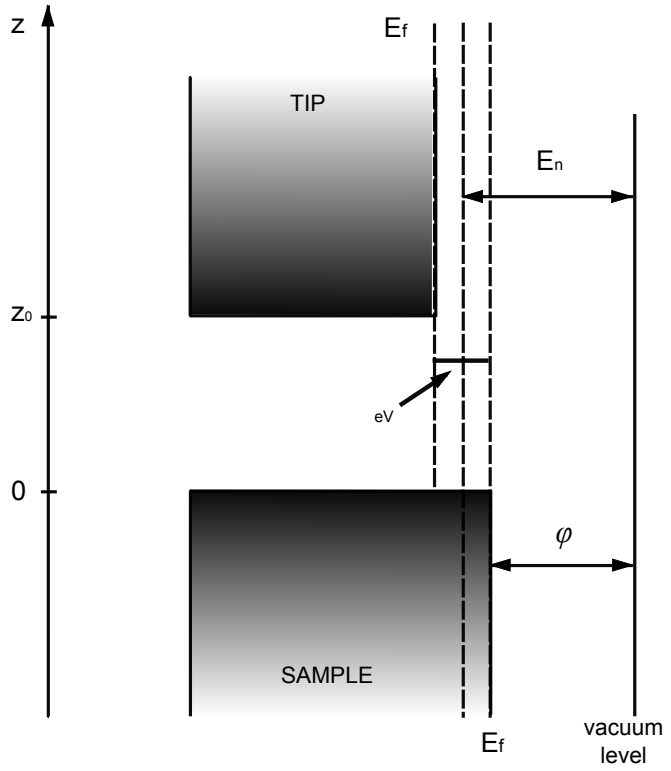

FIGURE 2.1. Energy diagram of the sample-tip system. A bias voltage V is applied. E_F denotes Fermi level, ϕ is the work function of the metal and E_n are eigenstates of the tip.

tunnel into states on another electrode with the same energy ($E_\mu = E_\nu$), and that the DOS does not vary significantly in a proximity of the Fermi level, for the tunneling current I it reads

$$I = \frac{2\pi e^2}{\hbar}|M_{\mu\nu}|^2 \rho_B(E_F)\rho_A(E_F)V, \tag{9}$$

where A and B denote the first and the second electrode, respectively. The matrix element $M_{\mu\nu}$ can be reformulated into a surface integral of the non-perturbed wave functions over the separation surface.

$$M_{\mu\nu} = \frac{\hbar^2}{2m}\int_{z=z_0}[\psi_\mu \frac{\partial \chi_\nu^*}{\partial z} - \psi_\mu \frac{\partial \chi_\nu^*}{\partial z}]dxdy \tag{10}$$

The current I is usually evaluated by summing over all relevant states. At finite temperatures the electrons in both electrodes obey the Fermi-Dirac distribution and this has also to be taken into account. At a bias

voltage V we have

$$I = \frac{4\pi e}{\hbar}\int_{-\infty}^{-\infty}[f(E_F - eV + \epsilon) - f(E_F + \epsilon)]\rho_A(E_F - eV + \epsilon)\rho_B(E_F + \epsilon)|M|^2 d\epsilon \tag{11}$$

If k_bT is sufficiently small, the Fermi-Dirac distribution is approximately a step function and the above integral becomes

$$I = \frac{4\pi e}{\hbar}\int_{0}^{eV}\rho_A(E_F - eV + \epsilon)\rho_B(E_F + \epsilon)|M|^2 d\epsilon \tag{12}$$

Further, Bardeen assumed that the magnitude of the matrix tunneling element does not change significantly in the relevant energy range and $|M|$ can be taken out of the integral. In other words, the tunneling current I can indeed be seen as a convolution of the DOS of two electrodes, as stated in the beginning of this subsection and quantitatively expressed in Eq.

In his original paper [38], Bardeen formulated the problem in the representation of the second quantization, which yields the following expression

$$I = \frac{2\pi e^2}{\hbar}V\sum_{\mu,\nu}|M_{\mu\nu}|^2\delta(E_\nu - E_F)\delta(E_\mu - E_F) \tag{13}$$

One year after the invention of the STM, Tersoff and Hamann developed a model based on Bardeen's tunneling theory [39]. As already stated, the tunneling current is proportional to the convolution of the density of states of the tip and the sample, but states of the tip are often unknown. For this reason Tersoff and Hamann supposed that the tip is a geometrical point, where the states are localized arbitrarily. This means further that the STM image bears the information not about of the tip-surface system, but of the surface properties only. So, the tip is modeled as a locally spherical potential well with a curvature radius R and center located at r_0, The tip is approaching very close to the surface, whereas the nearest distance amounts to d (Fig.2.2).

One can show that by summing up the sample states in the proximity of the Fermi level the formula for the differential conductance $G \equiv \frac{dI}{dV}|_V$

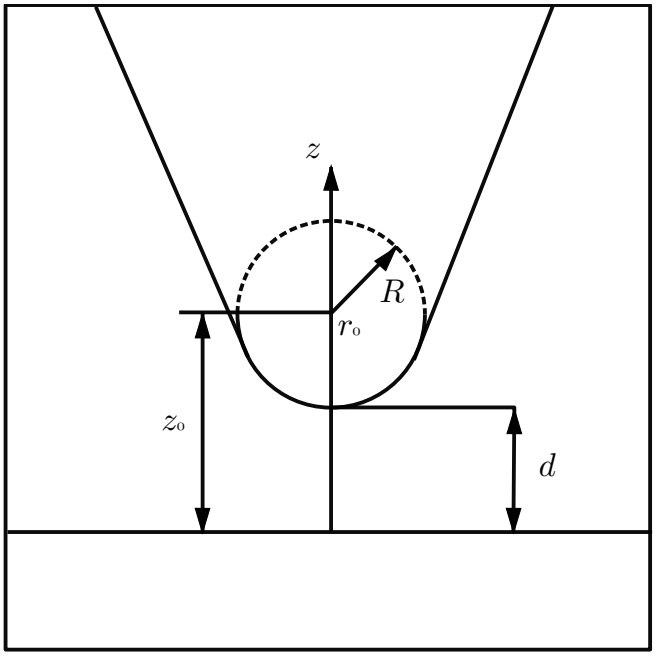

FIGURE 2.2. Visualization of the tip in the Tersoff-Hamann model. It is represented by a spherical potential well with a radius of curvature R. The center is located at r_0, and the tip is by d away from the surface.

gets the following form:

$$G \propto |\psi(\vec{r_0})|^2 \rho_S(E_F) \tag{14}$$

The right-hand side is the definition of the LDOS of the sample at the center of curvature of the tip and this is the central outcome of the Tersoff-Hamann model. If the tip state is spherically symmetric around $\vec{r_0}$, then it can be regarded as a geometrical point at $\vec{r_0}$. This further means that all the states except the ones of the s-type can be neglected and assumption is called s-wave tip model. There is no doubt that the model is very valuable, since it enables the STM images to be interpreted as landscapes of the electronic structure. On the other hand, it predicts that only superstructures of reconstructed surfaces with periodicities greater than 6 Å can be resolved, which is in contradiction with the high-resolution data obtained in the late 80s [39, 40, 41, 42], where individual atoms of the metal surfaces Au(111), Al(111), Cu(100) with the nearest-neighbour distances $2.5 - 3$ Å were imaged. This requires a modification of the underlying theory and

early attempts of the explanation in terms of mechanical interactions between tip and sample [43] could not give a satisfactory description of the experimental data [44, 45]. As all typically used materials in the tip fabrication (e.g. W, Pt, Ir) are d-band metals, e.g. in tungsten 85 percent of the DOS at the Fermi level comes from the d-states and it tends to form highly localized d_{z_2} bonds, Chen developed a theoretical model which includes d-states of the tip in the tunneling process [46, 47]. Newer models and a more realistic simulation of the STM operation were given by Hofer *et al.* [48].

To illustrate this we will start from the sample represented by a two-dimensional array of localized atomic orbitals, which exhibits hexagonal symmetry and then we will calculate the corrugation amplitude for different models of the tip electronic states. For such a system the surface charge density is given up to the lowest non trivial Fourier component by

$$\rho(\vec{r_0}) = \sum_{E \leq E_F} |\psi(\vec{r})|^2 \approx a_0(z) + a_1(z)\phi^{(6)}(k\vec{x}) \tag{15}$$

where $\vec{x} = (x, y)$ and $k = \frac{4\pi}{a\sqrt{3}}$ is the length of a primitive reciprocal lattice vector and a hexagonal cosine is defined as $\phi^{(6)}(\vec{x}) = \frac{1}{3} + \frac{2}{9}\sum_{j=0}^{2} \cos \vec{k}_j\vec{x}$ with $k_1 = (0, 1)$, $k_2 = (-\frac{1}{2}\sqrt{3}, -\frac{1}{2})$ and $k_3 = (\frac{1}{2}\sqrt{3}, -\frac{1}{2})$. For the first Fourier coefficients it suffices to consider the Bloch functions close to the high symmetry points of the Brillouin zone. The term a_0 comes from the Bloch functions at the Γ point and it behaves as $a_0(z) = e^{-2\kappa z}$, where κ is the decay constant. Theoretical expression of the topological STM image can be sought in the form:

$$z = z_0 + \delta z \phi^{(6)}(k\vec{x}), \tag{16}$$

where δz is the corrugation amplitude. Since the second term in the expression (15) is much smaller than the first one, it can easily be shown that:

$$\delta z(z_0) = -\frac{9a_1(z_0)}{2\frac{\partial a_0(z_0)}{\partial z_0}}, \tag{17}$$

It instructive to compare δz for different sample and tip states with δz for s/s-orbitals case, which we will set to 1. In case of a lattice with a period $a = 2.88$Å and work function $\phi = 3.8$eV, for the s/p sample-tip the ratio is 2.73, for s/d it is 12.9 and even 166 if d-states of both sample and tip are taken into account. With this we showed that the corrugation amplitudes for p- and d-states are significantly larger and they are in fact the origin of the atomic resolution of the STM images. It is now clear that a substantial condition for the achievement of the atomic resolution in STM is a localized tip state. In the case of metal surfaces those are d_{z^2} dangling-bond states, whereas for the semiconductors are p_z are relevant [49].

2.1.3. Principles of operation

Generally, there are two ways of operation of the STM - constant current and constant height mode. In constant current mode the feedback loop is open and as the current is proportional to the LDOS, the tip follows a contour of a constant density of states during scanning. In constant height mode the z-position remains unchanged, which can be seen as a slow or even disabled feedback loop. This mode is suitable for perfectly flat surfaces, otherwise the tip crash in unavoidable. An advantage of this mode is that the scanning frequency is very high unlike with constant current mode, where it takes several minutes to take one image.

Important prerequisites for high-quality scanning are ultra-high vacuum (UHV), low temperatures and good vibrational damping. UHV is necessary to keep the sample as uncontaminated as possible and typical pressure values amount to $<\approx 10^{-10}$ mbar. In order to minimize the thermal noise and mechanical motion low temperatures are essential, but the main goal is to obtain a good spectroscopy resolution, which is very temperature sensitive as well.

2.1.4. LT-STM experimental setup

The STM used for performing our experiments is a home-made Besocke beetle-type STM [50] made by Silvain Clair and all relevant details about it can be found in the references [51] and [52]. This setup is convenient for low temperature measurements below 10 K, which is reached by cooling with liquid helium and nitrogen, but also high temperature measurements up to 400 K by a simple heating up.

Our machine (Fig. 2.3) consists essentially of a preparation chamber and chamber where the scanning takes place (STM chamber). The chambers are under high-vacuum conditions and are separated from each other by a gate valve, which is kept closed during the scanning and the sample preparation. STM chamber is thereby pumped by an ion getter pump, and the preparation by a turbomolecular and one more ion pump. An additional titanium sublimation pump is creating the vacuum as well. The base pressure reached in the chambers is 10^{-11} mbar. The sample lies on a holder consisting of two rails and a fork, that can be released when changing or preparing the sample. The holder is placed at one end of the manipulator, with help of which the sample is transfered into the chambers. It can be moved both horizontally and vertically, but also can be rotated around its axis. The filaments for the sample heating are passing through the manipulator and end at the fork. The temperature is measured by a thermocouple directly behind the crystal, whereas the heating unit is attached to the front part of the manipulator.

Typically, before the molecules have been evaporated, the sample has to be properly cleaned and prepared. The molecules evaporate by an organic molecular beam epitaxy (OMBE) from a quartz glass crucible inside a Knudsen cell stabilized at a temperature T_{OMBE}. The cleaning is done by repeated cycles of Ar^+ sputtering and annealing (in the case of Ag(111) $T_{anneal} = 740$ K). If the sample is not present, the OMBE evaporates directly into a residual gas analyzer. It can detect partial pressure at the atomic mass of the molecules, which is used as a measure for the molecular

FIGURE 2.3. Image of the LT-STM setup. Parts of the UHV system are depicted: cryostat (blue), STM chamber (green), preparation chamber (red), sample manipulator (yellow), vibration isolation system (magenta).

flux. In UHV, the room temperature vapour pressure of the molecules is finite. As a result, the molecular flux obtained at a specific T_{OMBE} reduces with time after filling the crucible. During the molecule deposition, the sample is cooled by liquid nitrogen down to approximately 120 K and subsequently transfered into the scanning chamber, which is surrounded with two concentrically placed cryostats with liquid helium and nitrogen. Fully tanked reservoirs are enough for approximately two days.

2.2. X-ray Photoelectron Spectroscopy

Since a X-ray photoelectron spectroscopy (XPS) was also employed to complete STM measurements on the terminal alkynes in Chapter 6, I will give a brief overview of the XPS.

The XPS is a spectroscopy technique used to determine the chemical composition and the electronic structure of the elements that the material consists of. It requires UHV conditions and is based on the photoelectric effect, explained by Albert Einstein, for which he got the Nobel prize in 1905. Basically, the target material is irradiated by a beam of the X-rays, thereby the kinetic energy and number of the escaped electrons are simultaneously measured. Since the energy of the incident radiation E_{ph} is well-known, the binding energy E_b can be calculated using the following equation: $E_b = E_{ph} - (E_k + \phi)$. Kinetic energy of the electrons E_k is measured as well and ϕ is the work function of the spectrometer.

A typical XPS spectrum consists of the relative intensity, i.e. the number of the electrons detected plotted against the electron kinetic energy. The XPS spectrum is a fingerprint of each element: a set of peaks at certain binding energies corresponds to an electron configuration within an atom. The intensity of the peaks is directly related to the percentage of a compound in the entire investigated sample. It is important to note that only electrons originating from within the top 10 to 12 nm of the material are detected in the spectrometer. All deeper lying electrons are in another excited state.

A typical experimental setup is made of an X-ray source, which irradiates the sample in UHV-chamber. The chamber is equipped with an evaporator, a source of the molecules or material that has to be investigated, pumping system responsible for the UHV conditions, and an electron-analyzer. Our measurements were carried out at the HE-SGM monochromator dipole magnet beam line at the BESSY II synchrotron radiation source in Berlin, which provides light with a linear polarization of

90%. Samples were prepared *in situ* in ultrahigh vacuum, employing the procedure described above. The electrons were collected using a Scienta R3000 electron energy analyzer in perpendicular emission mode.

2.3. DFT Calculations

Density functional theory (DFT) calculations are another tool used as a significant support and an addition to our experimental data. The DFT is a quantum mechanical method for solving a many-body Schrödinger equation, or more precisely, for finding the ground state of the system. It is based on the Hohenberg-Kohn theorems [53] asserting that the ground state of the system is uniquely determined by a functional of the electron density, which depends on the spacial coordinates and that exactly in the ground state, the density functional has a minimum. However the theorem holds only for non-degenerated ground states in the absence of the magnetic field, but it is possible to extend it to the time-dependent density functional theory, in order to comprise excited states as well.

In this dissertation, periodic density functional theory calculations were carried out with the VASP code [54], with ion-core interactions described by the projected augmented wave (PAW) method [55, 56]. A variant of the van der Waals density functional [57] was used, with the exchange replaced by an optimized form of the Becke 86 exchange functional [58]. The plane waves were expanded to a cutoff of 500 eV and the Γ-point was used to sample the first Brillouin zone. A $p(77)$ and $p(109)$ unit cell were used in the calculations of TEB monomer and dimer, respectively. The Ag(111) surface was modeled by four layered slabs. All structures were relaxed until the forces on the atoms in the adsorbate and the two outermost layers of the slab were smaller than $0.01\frac{eV}{\mathring{A}}$. STM images were calculated using the Tersoff-Hamann approximation [59], as implemented by Lorente and Persson [60].

2.4. EBEM

All calculations concerning electron confinement were performed using Electron Boundary Elements Method (EBEM), which has been developed by F. J. García de Abajo and represents a scalar variant of the electromagnetic boundary element method extensively used for solving Maxwell's equations and optical response for arbitrary shapes [61]. It is suitable for the regions of constant potential that tessellate a plane, with the boundaries between regions being abrupt. The eigenstates of the systems are hereby expressed in terms of auxiliary sources on the region boundaries, whose propagation is described by Green's functions. Following the description of the formalism [62, 63] one can write the contribution of the σ_j source defined on the boundary of region j as $\psi_{scat}(\overrightarrow{R}) = \int_{S_j} ds\ G_j(\overrightarrow{R} - \overrightarrow{R_s})\sigma_j(s)$, where the integral extends over points $\overrightarrow{R_s}$ along the contour S_j defining region j. The total wave function is then imposed to be $\psi^{source} + \psi^{scat}$, where ψ^{source} describes an external source. The boundary sources are determined from the condition that both the wave function and its derivative must be continuous at the boundaries.

In this work, the main attention was given to the calculation of the local density of states (LDOS). The LDOS at a position $\overrightarrow{R_0}$ within a given region j can be derived by considering a point source at that position defined by $\psi^{source}(\overrightarrow{R}) = G_j(|\overrightarrow{R} - \overrightarrow{R_0}|)$. The LDOS is given by $\frac{m^*}{\pi\hbar^2} - \frac{2}{\pi} Im(\psi^{scat}(\overrightarrow{R_0}))$, where a factor of 2 accounting for spin degeneracy has been included.

For the band structure calculations, I successfully employed an additional part of the code, following the suggestion of J. E. Ortega to guide the analysis of the surface states, undergoing intriguing transformations in different interfacial dislocation networks [64, 65].

3 Theoretical concepts

3.1. Basics On Solid State Physics

In a perfect crystal the ions are arranged periodically, which means that the potential in which the electrons reside has also the periodicity of the underlying Bravais lattice and can be written in the form $U(\vec{r}) = U(\vec{r}+\vec{R})$, where $\vec{R}$ is a Bravais latiice vector. Due to a very high mass ratio of the nuclei and electrons, the Born-Oppenheimer, i.e. adiabatic approximation can also be applied on the ideal solid. It enables the total wave function to be broken into electronic and ionic component: $\psi_{total} = \psi_{electron} \otimes \psi_{ion}$, so that solutions for both parts can be sought independently. The problem of electrons in a solid is basically a many-body problem, meaning that both the interactions with the massive ions and electron-electron interactions have to be taken into account. In the approximation of the independent electrons, these interactions are represented by an effective periodic potential $U(\vec{r})$. Then it is natural that the eigenstates and eigenenergies arise from the Schrödinger equation

$$H\psi = (-\frac{\hbar^2}{2m}\nabla^2 + U(\vec{r}))\psi = E\psi. \tag{18}$$

Since the potential is periodical, it can be expanded in the plane waves basis and written as a Fourier series

$$U(\vec{r}) = \sum_{\vec{G}} V_{\vec{G}} e^{i\vec{G}\cdot\vec{r}}, \tag{19}$$

where $\vec{G}$ denotes the three-dimensional bulk reciprocal lattice vector. The wave functions are Bloch waves characterized by a 3D wave vector $\vec{k} = (k_x, k_y, k_z)$

$$\psi_{\vec{k}}(\vec{r}) = e^{i\vec{k}\cdot\vec{r}} U_{\vec{k}}(\vec{r}) = e^{i\vec{k}\cdot\vec{r}} \sum_{\vec{G}} u_{\vec{k},\vec{G}} e^{-i\vec{G}\cdot\vec{r}} = e^{i\vec{k}\cdot\vec{r}} \sum_{\vec{G}} u_{\vec{k}-\vec{G}} e^{-i\vec{G}\cdot\vec{r}}. \tag{20}$$

The function $U_{\vec{k}}(\vec{r})$, exhibiting the potential periodicity, has also been written as a Fourier series. Insertion of the Eq. 20 into the Schrödinger equation and exploitation the orthogonality of the plane waves $e^{-i\vec{G}\cdot\vec{r}}$ yields an infinite set of coupled linear equations for the Fourier coefficient $u_{\vec{k}-\vec{G}}$:

$$\{\frac{(\vec{k}-\vec{G})^2}{2} + V_0 - E\} u_{\vec{k}-\vec{G}} + \sum_{\vec{G}' \neq \vec{G}} V_{\vec{G}-\vec{G}'} u_{\vec{k}-\vec{G}'} = 0 \tag{21}$$

or

$$u_{\vec{k}-\vec{G}} = -\frac{\sum_{\vec{G}' \neq \vec{G}} V_{\vec{G}-\vec{G}'} u_{\vec{k}-\vec{G}'}}{\frac{(\vec{k}-\vec{G})^2}{2} + V_0 - E}. \tag{22}$$

One of the most common approaches in the solid state theory, which nicely introduces the concept of the band structure is the nearly free-electron (or "two-band") approximation. Namely, in the previous consideration only two basis vectors with $\vec{G}_1 = 0$ and $\vec{G}_2 = g$ are employed. The total electron wave function can be written as

$$\psi_{\vec{k}}(\vec{r}) = e^{i\vec{k}\cdot\vec{r}} (u_{\vec{k}} + u_{\vec{k}-\vec{g}} e^{-i\vec{g}\cdot\vec{r}}). \tag{23}$$

It is now convenient to write down the Eq.xx in the matrix form

$$\begin{pmatrix} \frac{\vec{k}^2}{2} + V_0 - E & V_{\vec{g}} \\ V_{\vec{g}} & \frac{(\vec{k}-\vec{g})^2}{2} + V_0 - E \end{pmatrix} \begin{pmatrix} u_{\vec{k}} \\ u_{\vec{k}-\vec{g}} \end{pmatrix} = 0. \tag{24}$$

Since there are only two Fourier coefficients of the potential $V_{\vec{g}}$ and $V_{-\vec{g}}$ and the space reversal symmetry holds ($V_{\vec{g}} = V_{-\vec{g}}$), the electrons in the state $\psi_{\vec{k}}$ are exposed to an effective pseudopotential

$$V(\vec{r}) = V_0 + 2V_{\vec{g}} \cos(\vec{g}\cdot\vec{r}). \tag{25}$$

In order for this equation to have a non-trivial solution, the determinant of the matrix must be zero, which all together with $V_{\vec{r}}$ leads us to two values of eigenenergies

$$E = V_0 + \frac{1}{2}\vec{k}^2 - \frac{1}{4}\vec{g}(2\vec{k} - \vec{g}) \pm \sqrt{|V_{\vec{g}}|^2 + \left(\frac{1}{4}\vec{g}(2\vec{k} - \vec{g})\right)}. \tag{26}$$

This means that we obtained two bands separated by a bandgap of width $2V_{\vec{g}}$, which is illustrated in Fig. 3.1 Theoretically, solids have infinitely many bands, but the highest ones are irrelevant, since their energy is too large and the electrons occupying these bands can be regarded as ionized. Depending on the band structure, all materials can be divided into three main groups: metals, semiconductors and insulators. In the case of metals, the highest allowed band (so called conduction band) is partially filled, so that the electrons from the valence band (the lowest allowed) can easily occupy empty levels and lead to the conductance of the material. On the contrary, semiconductors and insulators have the conduction band above the Fermi level and only very few electrons can become conducting. An essential difference between semiconductors and insulators is the band gap between valence and conduction band. In insulators it is smaller, which directly means smaller conductivity. It is noteworthy that the electrons can be excited to move to the conduction band by thermal excitations. This is the reason why the conductivity of semiconductors is strongly temperature dependent.

As already stated above, the described procedure applies to perfectly periodical, endless "bulk" materials. In the case of boundary regions and interfaces, i.e. when the symmetry breaking is present, the complete picture of the electron behaviour is substantially changed. In order to get a detailed insight into it, we will consider a model of a semi-finite solid: we chose the region $z < 0$ to be fully occupied by the bulk (z is directed parallel to the surface normal). It turns out that one can chose a point z_m which separates crystal region (for $z < z_m$) from the barrier one ($z > z_m$) and in these two regions the Schrödinger equation can be solved separately.

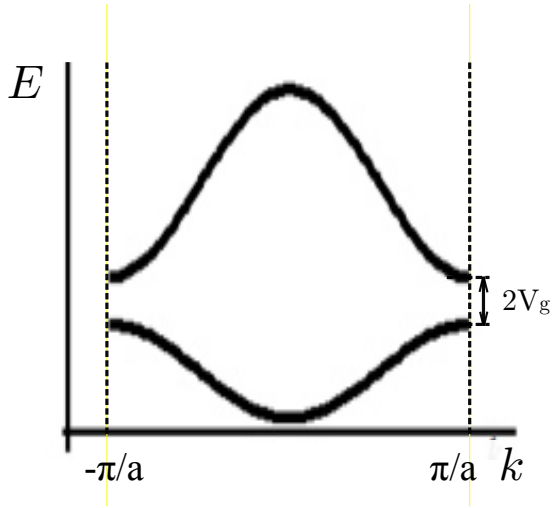

FIGURE 3.1. A simple picture of the electronic bands in one-electron approximation in one-dimensional case

The states in the $z < z_m$ region are in fact bulk states periodic in three dimensions. Contrary to that, the "barrier" region is now finite, thus the wave function is periodical only in two dimensions in the surface plane.

In the $z > z_m$ case potential and wave function can also be expanded into Fourier series, but with a restriction on two-dimensional reciprocal lattice vectors $\vec{G}_{||}$:

$$V(\vec{r}) = \sum_{\vec{G}_{||}} V_{\vec{G}_{||}}(z) e^{-i\vec{G}_{||}\cdot\vec{r}_{||}}, \tag{27}$$

$$\psi^B_{\vec{G}_{||}}(\vec{r}) = e^{i\vec{k}_{||}\cdot\vec{r}_{||}} \sum_{\vec{G}_{||}} B_{\vec{k}_{||}-\vec{G}_{||}} e^{-i\vec{G}_{||}\cdot\vec{r}_{||}}, \tag{28}$$

with the coefficients $\vec{G}_{||}(z)$ and $B_{\vec{k}_{||}-\vec{G}_{||}}$ being z-position dependent.

In the crystal region the potential is identical as in the bulk material, so the wave function can be represented as a superposition of three-dimensional plane waves $\Phi_{\vec{k}}(r)$ that exhibit the same energy E and parallel momentum component $\vec{k}_{||}$, whereas the normal component $\vec{k}_z$ is different:

$$\psi^C_{\vec{k}_{||}}(\vec{r}) = \sum_{\vec{k}=(\vec{k}_{||},\vec{k}_z)} \phi_{\vec{k}} \Phi_{\vec{k}}(r). \tag{29}$$

Bearing in mind that the projection of the 3D reciprocal lattice vectors onto the surface gives exactly $\vec{G}_{||}$-part of the basis, the above equation is easily transformed into a 2D variant:

$$\psi^{C}_{\vec{k}_{||}}(\vec{r}) = e^{i\vec{k}_{||}\cdot\vec{r}_{||}} \sum_{\vec{G}_{||}} C_{\vec{k}_{||}-\vec{G}_{||}}(z) \tag{30}$$

It is very important to notice that Bloch waves with complex $k_z = p - iq$ has to be considered as well, because for $q > 0$ the wave functions $\Phi_{\vec{k}}(\vec{r})$ become $\Phi_{\vec{k}}e^{qz}e^{ipz}(\vec{r}) = e^{-i\vec{k}_{||}\cdot\vec{r}_{||}}u_{\vec{k}}(\vec{r})$, having the maximal amplitude at the border plane $z = z_m$ and decaying exponentially towards the interior of the solid ($z \to \infty$). For this reason they are called evanescent waves. Although the momentum can be complex, the energy E is always real, which imposes reduction of the possible combinations of $p-q$ pairs; in the complex $\vec{k}$-space they build "real lines".

3.2. Surface states

We saw that surface states directly come out from the Schrödinger equation as a consequence of the symmetry breaking. They are essentially different from bulk states in solids and the pertaining wave functions decrease exponentially with the distance from the interface. Basically, there are two types of surface states. So-called Tamm states [66] exist if the periodic potential is distorted [67] and they are typically described within the one-dimensional Kronig-Penney model. By contrast, Shockley states [68] are present for potentials with a non-distorted periodicity. An earlier work has shown that the bands formed by surface states are to a good approximation parabolic [69]. In this dissertation I will focus on Shockley states only, encountered on Cu(111), Au(111) and Ag(111) surfaces [63].

As soon as the electrons posses less degrees of freedom, i.e. their movement is restricted to one or two dimensions, we speak about the electron confinement. In the one-dimensional case it is a textbook quantum well in which the states of the surface electrons are represented by standing

waves; in two dimensions these are space standing waves, whose shape depends on the shape of the well geometry. Two-dimensional confinement is typically realized by a controlled positioning of the adatoms on the surface and in that manner quantum corrals [70] of desired shape are produced, but the method turned out to be only locally applicable. For a surfacewide creation of potential barriers another method - self assembly method - has to be employed. By means of self-assembly it is possible to create regular nanoporous networks, where the pores play the role of the confining wells [63] and one has a possibility to entirely control and tune electronic properties.

We describe the surface state band with a constant effective mass m^* and thus a quadratic energy dispersion relation $E(\vec{k})$ (m^* is by definition the second derivative of $E(\vec{k})$). Hence the eigenenergies are written in the form

$$E_n = E_0 + \frac{\hbar k^2}{2m^*},$$

where E_0 is the onset energy of the surface state band and $\vec{k}$ is the wave vector parallel to the surface. The surface state also manifests itself in the STS measurements. When measuring the dI/dV_B signal at constant height, (i.e., the derivative of the tunnel current I with respect to the bias voltage V_B), it is approximately proportional to LDOS [39], as we saw in the Chapter 2. The surface state related DOS is given by $\rho_{surf} = \frac{m^*}{\pi\hbar^2}$ [71], and an abrupt rise of the LDOS is visible at E_0. From the Fig. 3.2 one can see that the spectral signature exhibits a clear stepwise jump of the LDOS at E_0.

Another important characteristics of the Shockley-type surface energy bands is the temperature dependence [73], which is to be ascribed almost exclusively to bulk effects. Namely, due to the temperature-induced variation of the bulk lattice constant, the energy gaps are shifted and this directly affects the position of the surface band energy.

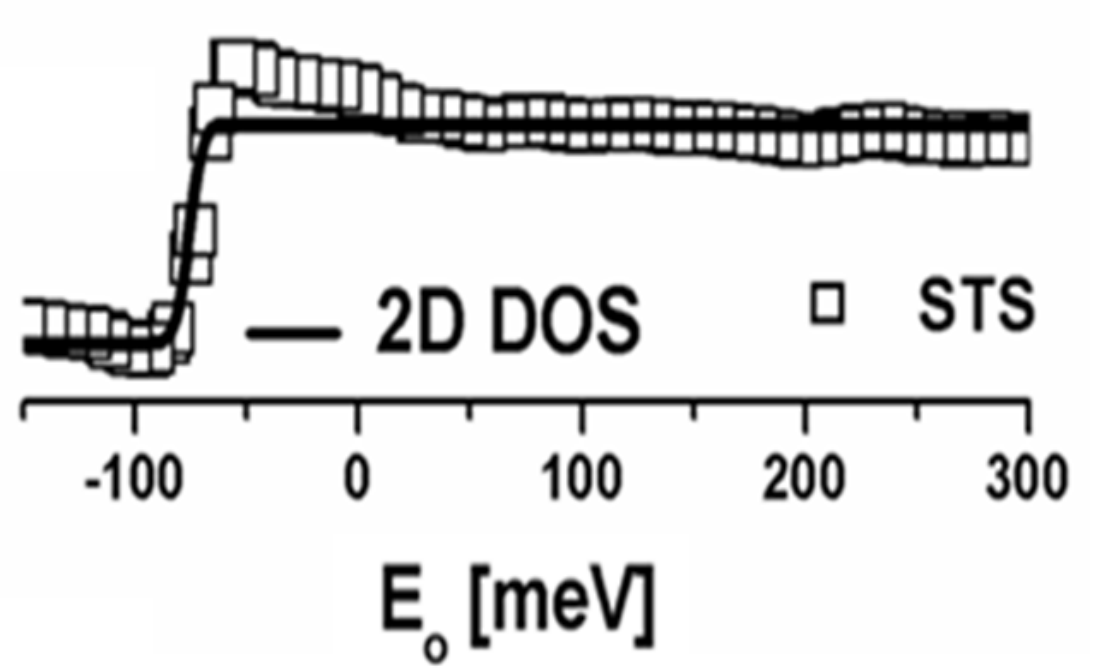

FIGURE 3.2. Spectroscopy signature of the Ag(111) surface. The full line is predicted by theory, dotted line came out from the STS measurements. In both cases a step at -65 meV, i.e. the energy offset of the surface state is visible. The illustration has been taken from the Ref. [72].

3.3. Calculation of the reflexion and transmission coefficient

Since the reflexion (R) and transmission (T) coefficient of the barrier were explicitly calculated in order to explain shape of the peaks in the LDOS spectrum (see Chapter 7), it is instructive to give a short overview of how these expressions are derived.

If a quantum barrier of a width a and height V is given (Fig. 3.3), then the wave functions in the three regions can be written as follows:

$$\psi_I(x) = Ae^{ikx} + Be^{-ikx} \tag{31}$$

$$\psi_{II}(x) = Ce^{\kappa x} + De^{-\kappa x} \tag{32}$$

$$\psi_{III}(x) = Fe^{ikx} + Ge^{-ikx}. \tag{33}$$

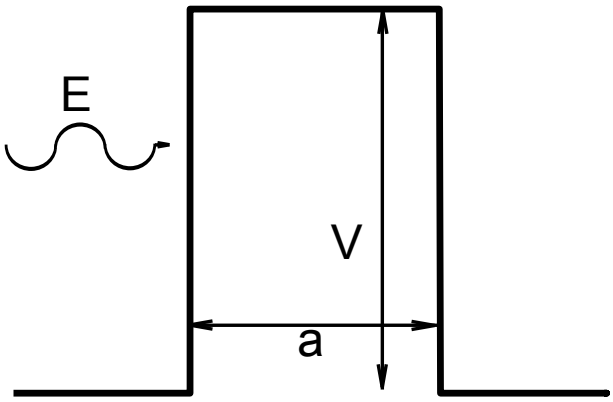

FIGURE 3.3. A simple one-dimensional quantum barrier. The height of the barrier is V and the width a. Energy of the incoming electron is E.

Coefficients in the functions are determined from continuity of both function and its derivative at the boundary points (in this case $x = 0$ and $x = a$):

$$\psi_I|_{x=0} = \psi_{II}|_{x=0} \tag{34}$$

$$\psi_{II}|_{x=a} = \psi_{III}|_{x=a} \tag{35}$$

and

$$\psi'_I|_{x=0} = \psi'_{II}|_{x=0} \tag{36}$$

$$\psi'_{II}|_{x=a} = \psi'_{III}|_{x=a} \tag{37}$$

Applying the boundary conditions on the wave functions gives the following restriction on the coefficients:

$$A + B = C + D \tag{38}$$

$$ik(A - B) = i\kappa(C - D) \tag{39}$$

$$Ce^{\kappa a} + De^{-\kappa a} = Fe^{ika} + Ge^{-ika} \tag{40}$$

$$i\kappa(Ce^{\kappa a} - De^{-\kappa a}) = ik(Fe^{ika} - Ge^{-ika}). \tag{41}$$

On the other hand, transmission coefficient T is defined as a proportion of the current density, i.e. modulus of the complex amplitude of the transmitted and incoming wave $T = \frac{|\vec{j}_{trans}|}{|\vec{j}_{in}|} = \frac{|F|^2}{|A|^2}$ and the reflexion coefficient as a quotient of $\vec{j}$ of the reflected and incoming wave: $R = \frac{\vec{j}_{refl}}{\vec{j}_{in}} = \frac{|B|^2}{|A|^2}$.

Assuming that there is no wave absorption we can claim that the two coefficients give in total 1: $R+T=1$. If the energy of the electron is greater than the barrier height, i.e. $E > V$, the following expression holds:

$$T(E) = \frac{1}{1 + \frac{V^2 \sinh^2(ka)}{4E(E-V)}}. \tag{42}$$

If the incoming electron wave possesses an energy that is smaller than the potential of the barrier, $E < V$, $T(E)$ then reads:

$$T(E) = \frac{1}{1 + \frac{V^2 \sinh^2(ka)}{4E(V-E)}}. \tag{43}$$

We clearly see that also in this case $T(E)$ has a non-zero value, which is a manifestation of quantum mechanical effect of tunneling, meaning that there is a certain probability that even particles with energy under barrier tunnel through it.

4 Hierarchically Organized Bimolecular Ladder-Network Exhibiting Guided One-Dimensional Diffusion

4.1. Introduction

Molecular self-assembly is ubiquitous in biological systems for the production and reproduction of functional units and even living species [74, 75]. Among the most important requirements for the formation of the highly complex supramolecular architectures is the presence of hierarchy in the bonding to allow multi-level assembly [76]. Adapting this strategy and creating novel molecular building blocks with the ability to self-assemble into supramolecular networks is a promising bottom-up technique in nanotechnology [6, 77, 7, 78]. Many studies show examples of artificial self-assembled molecular nanostructures; however they are often limited to only one level of order. Increasing efforts are dedicated to master the formation of ordered structure comprising a multi-level hierarchy [79, 80, 81, 82, 83]. At each level of organization novel functionalities can be expected to be realized [84]. For further improvement of the control over the resulting architecture, hierarchy has to be introduced in the bonding motifs itself [85, 86].

Here I show a bimolecular two-level hierarchic assembly process which leads to a ladder-shape two-dimensional (2D) network exhibiting intriguing dynamic behavior. In contrast to other heteromolecular approaches

[87, 88, 89, 90, 91, 92] the two organic species couple *via* two different bonding motifs of different strength leading to a 2D supramolecular architecture consisting of two sublattices. The stronger bound sublattice is organized and linked by a novel hydrogen bond motif. At elevated temperature the one-dimensional (1D) diffusion of the molecules of the weaker bond sublattice is guided by the more stable multimolecular superstructure.

4.2. Results

The two molecules used in this study, namely sexiphenyl dicarbonitrile (6DC) and N,N-diphenyl oxalic amide (DOA), are presented in Fig. 4.1. They were deposited from a double organic molecular beam epitaxy source onto a prepared Ag(111) substrate. Subsequent Scanning Tunneling Microscopy (STM) observations were performed at a substrate temperature (T_{sub}) as indicated, typically 10 K. Both organic species have at first separately been the subject of detailed studies regarding their behavior on Ag(111) or Au(111) substrates [93, 12]. It appears that DOA molecules (Fig. 4.1a) self-assemble into hydrogen-bonded 1D molecular wires[93, 94]. 6DC on the other hand (Fig. 4.1b) are found to arrange into a variety of highly regular, commensurate, and porous networks with various symmetries [12, 95]. Very recently, a study of open-porous networks consisting of both molecules was conducted [96]. Depending on the exact stoichiometry of the constituents different types of networks are found and the formation of the networks was assessed by theoretic modeling.

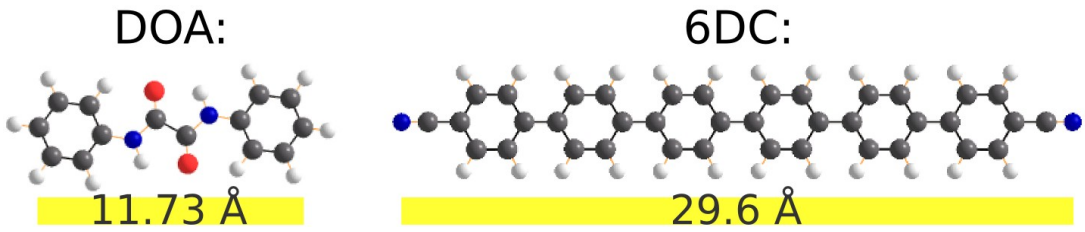

FIGURE 4.1. Molecular building blocks used: N,N'-diphenyl oxalic amide (DOA), sexiphenyl dicarbonitrile (6DC). Hydrogen in white, carbon in black, oxygen in red and nitrogen in blue.

As both molecules (6DC and DOA) are co-deposited on the Ag(111) surface, a different open-porous network arises, as shown by STM observation reported in Fig. 4.2. The ratio of 6DC to DOA molecules is just under 2:1 in the performed experiments (63% 6DC and 37% DOA in Fig. 4.2). The DOA molecules appear as two lobes and are shorter than the 6DC molecules which look like elongated sticks. The network consists of a series of 6DC-DOA chains ($6DC_{ch}$ and DOA aligned vertically in Fig. 4.2), which are connected by brighter 6DC molecules that can be seen as rungs ($6DC_{ru}$), making it reminiscent of ladders. The pore size of the rhombic cavities (highlighted by the yellow area) is approximately equal to 7 nm^2. When all rungs of the ladders are present, the ratio 6DC to DOA is exactly 2:1. However, we observe here that the number of $6DC_{ru}$ spacers between the different lines is variable and depends on the coverage of 6DC, thus impacting the density of rhombic cavities. Dimensions relevant to the ladder network are drawn in yellow in Fig. 4.2, including angles α, β, γ, δ and ϵ of the different units with respect to the substrate, and periodicities A and B of the network along two directions. Measured values are: α=15.7°; β=67.8°; γ=85.5°; δ=1.8°; ϵ=42.0°; A=33.3 Å; B=42.1 Å.

The ladder-shaped supramolecular structure exhibits chiral properties which result from the heteromolecular binding motif as indicated by lower coverage data of Fig. 4.3a. The STM image displays bimolecular chains that appear in five different directions (out of six observed in total) and can be classified in two enantiomeric variants (*Right* and *Left*). The analysis of the data demonstrates that the two enantiomorphs are evenly present in the samples and that the supramolecular chain formation is

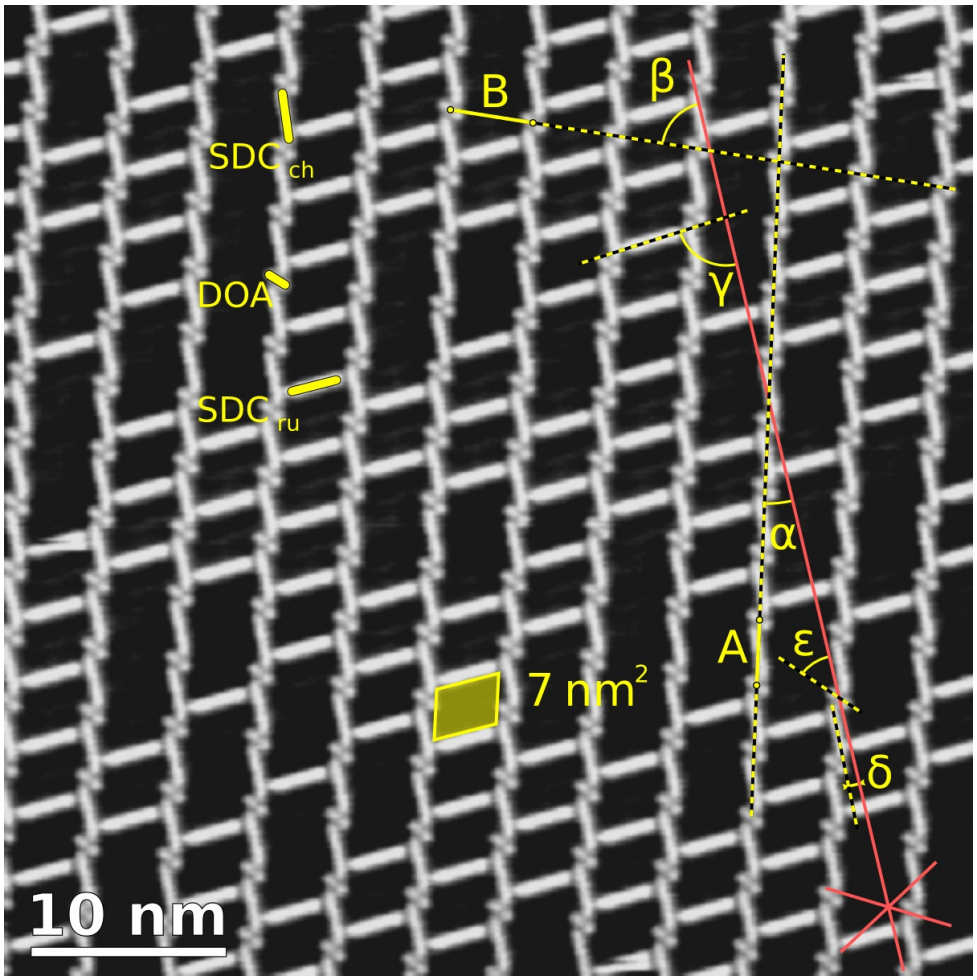

FIGURE 4.2. Overview STM topographic image of an open-porous network obtained after co-deposition of sexiphenyl dicarbonitrile (6DC$_{ch}$ and 6DC$_{ru}$) and N,N-diphenyl oxalic amide (DOA) molecules on the Ag(111) surface. The substrate high-symmetry directions are marked by the red star (bottom right corner), also in all our images. The different angles of the molecular units with respect to the indicated direction are noted α, β, γ, δ and ϵ. The periodicity in two different directions is defined by lengths A and B. (Bias voltage V_B=-1 V, tunneling current I=70 pA, substrate temperature T_{sub}=10 K).

controlled by the substrate periodicity. In addition, the energetic hierarchy behind the different bonds possible with the two organic species (Fig. 4.3b) becomes evident. In the network two different interactions are already distinguishable: 6DC$_{ch}$–6DC$_{ru}$ and 6DC$_{ch}$–DOA. Both of them involve the carbonitrile moiety of 6DC molecule. The 6DC$_{ch}$–6DC$_{ru}$ interaction is well known from earlier work [12] and involves a C-N$\cdots$H-C$_{ph}$ bond motif. The 6DC–DOA interaction on the other hand was not observed prior in self-assembly and will be discussed in more detail later. The last possible

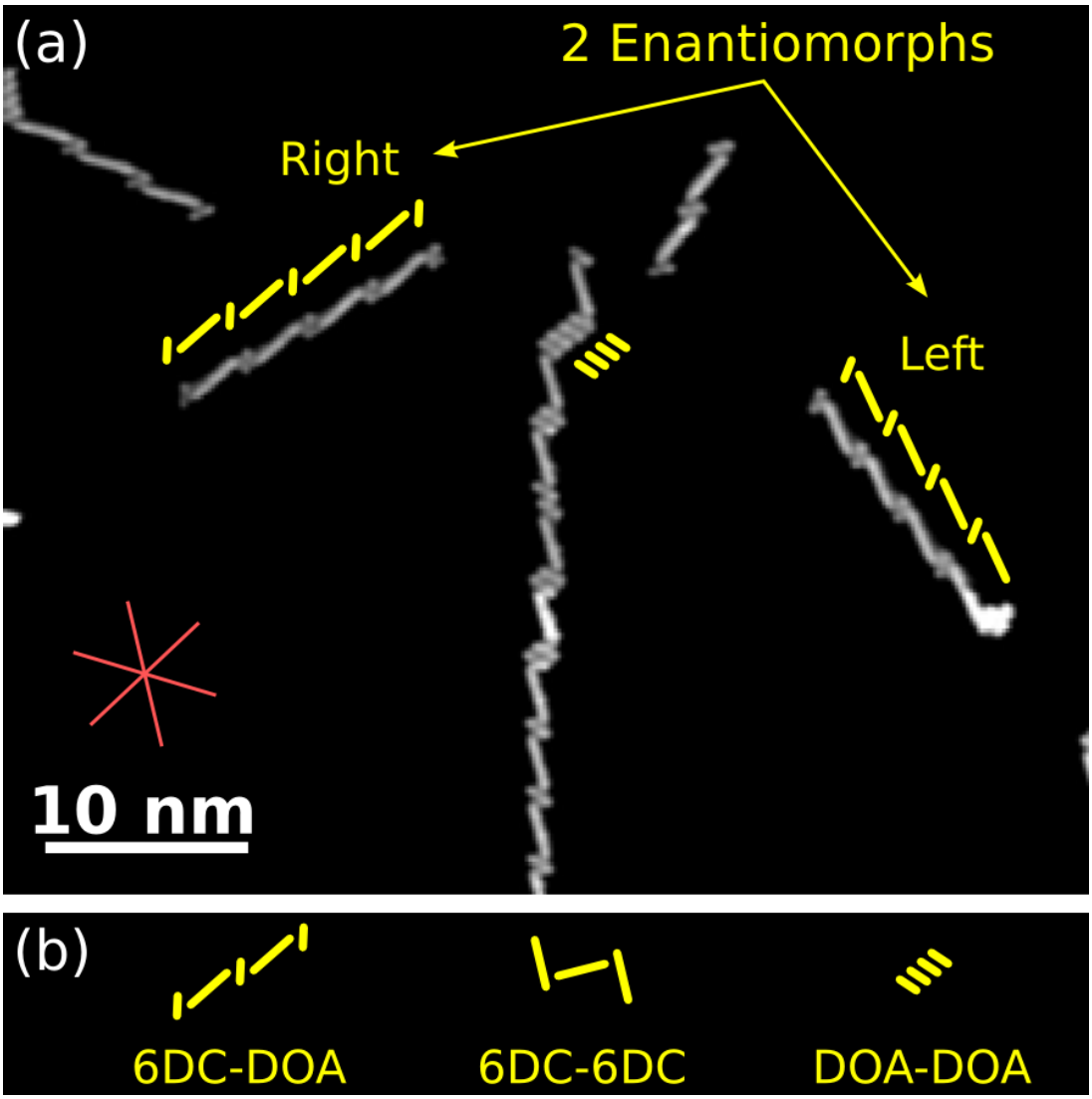

FIGURE 4.3. (a) STM topographic image of the chiral bimolecular chains at low coverage featuring the two enantiomorphs, *Right* and *Left*. (V_B=-1.16 V, I=80 pA, T_{sub}=10 K). (b) The 3 types of bonds observed: 6DC–DOA, 6DC–6DC and DOA–DOA. The preferred formation of alternate 6DC and DOA chains proves that the 6DC–DOA interaction is stronger in average than that between identical molecules (namely 6DC–6DC and DOA–DOA).

interaction, namely DOA–DOA, is not present in the ladder-network, but appears in sample with excess DOA, as shown in Fig. 4.3a. We can deduce from this that the 6DC–DOA interaction is stronger than the mean value of 6DC–6DC and DOA–DOA interactions.

4.2.1. Discussion

For a better understanding of the novel binding motif I start with the construction of a detailed model of the network. The apparent height of the two molecules in the STM images (∼1 Å, slightly depending on the tunneling conditions) is consistent with reported values for π-conjugated organic molecules in planar adsorption geometries [97, 98, 99, 100, 101]. Therefore, as a starting point, I consider only the flat conformations of both molecules to build the model displayed in Fig. 4.4.

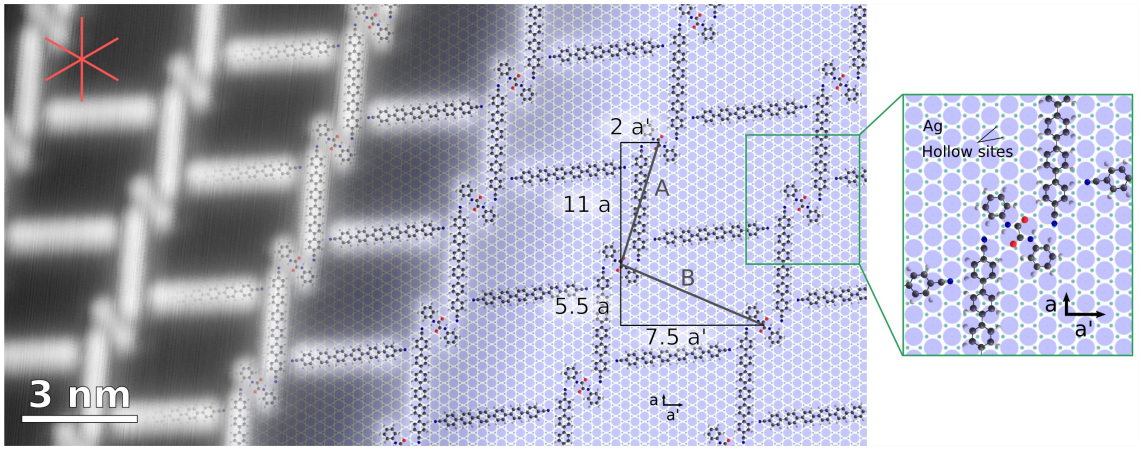

FIGURE 4.4. High-resolution STM data of the bimolecular open-porous network, superimposed with a ball-and-stick model of the molecules over the Ag(111) substrate. The original STM image has been geometrically corrected (shear and expansion ∼3%) to better fit the model. Major characteristics of the network are indicated in substrate lattice parameter scale a and a'. The zoomed area highlights the position of molecules over the Ag substrate, where hollow sites are marked with small green dots. (V_B=-1.12 V, I=60 pA, T_{sub}=10 K).

To derive this model, three different approaches were combined: (i) a thorough analysis of numerous STM images, especially regarding the measurement of angle α and δ, as well as the angle between 6DC–DOA chains of two different chiralities (as seen for example in Fig. 4.3a); (ii) the placement of CN groups of 6DC molecules at hollow sites of the Ag(111) surface, as exposed in a previous publication [12, 102]; (iii) the detailed understanding of bonding regions as unraveled by theoretical calculations presented below. Via this approach it was possible to create an accurate model which fits (within usual STM error) all the images, including the most peculiar configurations, *e.g.* near step edges (not shown here). This

model, detailed in units of the Ag(111) surface Fig. 4.4, is confronted to a high resolution STM image of the network, and allows a very accurate evaluation of dimensions reported in Fig. 4.2. The theoretical values thus are: α=17.5°; β=67.1°; γ=84.4°; δ=1.6°; ϵ=41.4°; A=33.16 Å; B=40.56 Å. These appear to be within 2° and 4% of the measured ones, well within usual STM error. The zoomed region of Fig. 4.4 shows how CN groups are localized near bridge sites [12].

To further study the relative strength of the observed bonds, a series of experiments at different temperatures was performed, and the stability of the self-assembled structure was evaluated. At T_{sub} = 75 K, we observe (Fig. 4.5a) that few 6DC$_{ru}$ spacers start to move along the bimolecular chains. This result corroborates that the 6DC$_{ch}$–6DC$_{ru}$ interaction is weaker than that for the 6DC$_{ch}$–DOA. When the temperature of the substrate is increased to 102 K (Fig. 4.5b), all 6DC$_{ru}$ spacers diffuse, but remain confined in between 6DC$_{ch}$–DOA chains. At 119 K (Fig. 4.5c), the diffusion is even faster, but still the 6DC$_{ch}$–DOA chains remain intact. They finally break for temperatures higher than 132 K (not shown).

Further analysis of similar images at 9 different temperatures allows to draw the Arrhenius plot presented in Fig. 4.5d. Specifically, as in the publication[102], the hopping rate R is calculated using the expression $R = \frac{h_e}{h_p \cdot t}$, where h_e is the number of hopping events occurring during the time t, and h_p is the number of hopping-able 6DC molecules, *i.e.*, the molecules that have enough space to perform movement. At low temperatures, the time t is the time elapsed between two successively taken pictures. For temperatures above 103 K, as the hopping process is more frequent, only single pictures are analyzed, and h_e is evaluated for each molecule counting the number of bright-to-dark and dark-to-bright changes in the 6DC$_{ru}$ molecules (see Fig. 4.5b&c), and t is the time necessary to scan enough lines to visualize the whole molecule. The best fit of these values gives an effective hopping barrier of 205 meV (±11 meV), and a prefactor of

$2.7x10^{9.4\pm0.6}$ Hz, well within the known broad range in the literature [103, 100, 102].

Finally, it needs to be emphasized that the ladder rungs have a stabilizing effect on the separation of the $6DC_{ch}$–DOA chains. Interestingly, this holds even in the dynamic regime. From Figure 4b and c it is evident that the $6DC_{ch}$–DOA chains form a highly regular grating whose periodicity is perfectly retained and unaffected after the onset of rung diffusion. Thus there is a dynamic stabilization of the supramolecular arrangement, which effect could be used in itself, by using dicarbonitrile or other linkers with appropriate length or even other hierarchic bonding patters, to fabricate tailored superlattices with definite regularity. By contrast, previously reported related 1D supramolecular gratings without stabilizing elements on a homogeneous surface inevitably showed a certain degree of variation in the distances between the constituting molecular lines [104, 105], even in the presence of adatoms in between them [106]. Thus, the introduction of the stabilizing effect by lateral weak linkages in hierarchic assemblies complements previous approaches with molecular gratings based on anisotropic templates [90, 107].

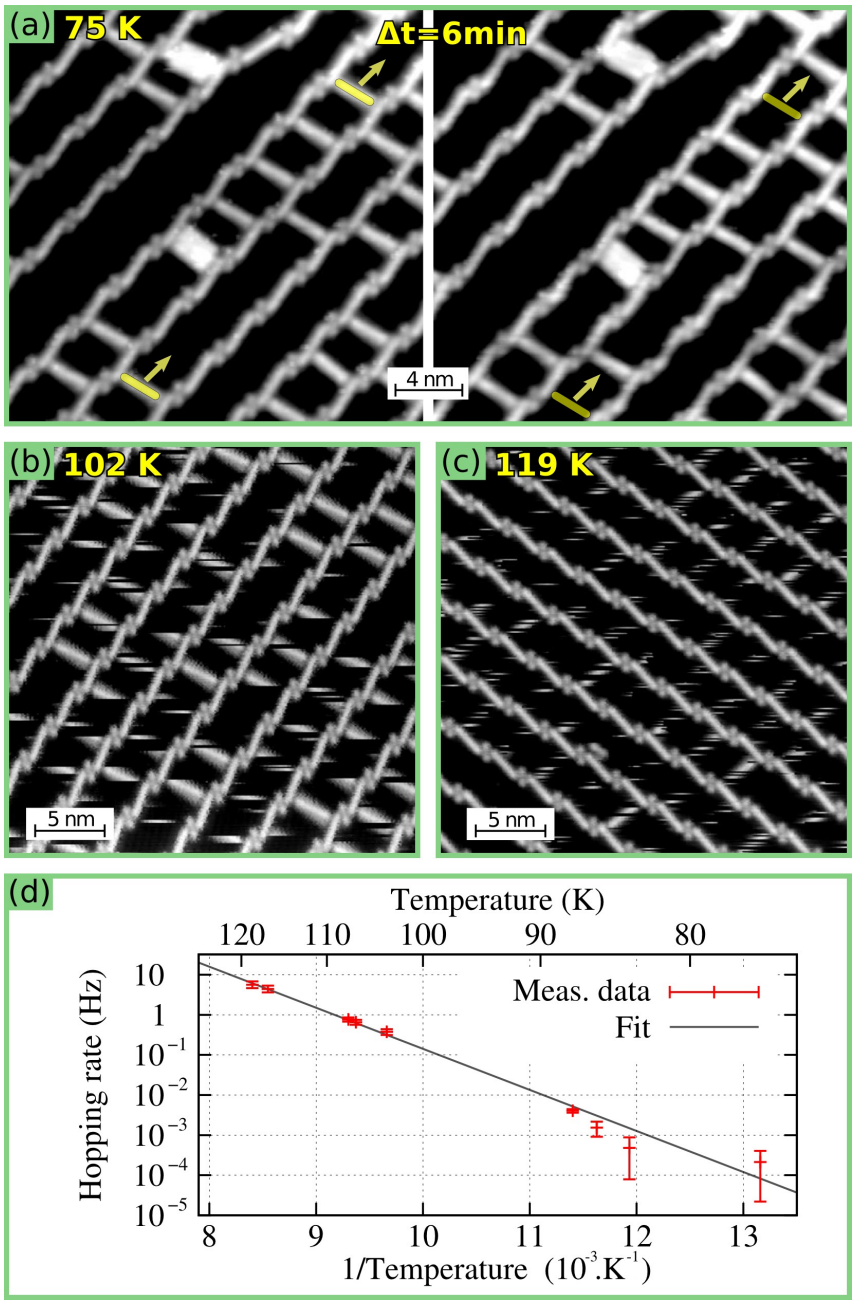

FIGURE 4.5. 1D 6DC diffusion guided by the bimolecular chains: (a) $T_{sub} = 75$ K, the two images show the same area of the network (*Right* chirality), the second being taken 6 minutes after the first one. Arrows are added to highlight the hopping events.(b) $T_{sub} = 102$ K. Frizzled appearance of $6DC_{ru}$ indicates diffusion within stable chains. (c) $T_{sub} = 119$ K, $Left$ chirality. The change in the frizzled features results from a higher hopping rate. (d) Arrhenius plot drawn from similar images at 9 different temperatures. Data are corrected to take into account the low scanning speed of the STM at high hopping rates (temperatures). The derived least squares fit gives an effective hopping energy of 205 meV (±11 meV), and a prefactor of $10^{9.4\pm0.6}$ Hz.

4.2.2. Theoretical investigation

In order to better understand the nature of the 6DC–DOA interaction, as well as to quantitatively compare it to the $6DC_{ch}$–$6DC_{ru}$ bond, total energy calculations were performed in the Density Functional Theory framework. The aim is not only to get the binding energies of the different bonds, but also to have a clear picture of the complete energy landscape in the different binding regions of the molecules. Since this requires extensive computations, a tremendous reduction of the computational cost is required. First, the simulations were performed without the presence of a substrate, as successfully used in a previous study[108]. By doing so, we assume that the interplay between the substrate-molecule and molecule-molecule bondings is minimal, which was checked with a test model.

This also allows us to study solely the interaction between molecules and not with the substrate. Then, the smaller NC-Ph_2-CN (biphenyl dicarbonitrile 2DC) molecule has been used, when only the CN group was involved in the bonding motif. Extensive convergence tests of NC-Ph_X-CN molecules (X up to 4) have indeed shown that the behaviour of the CN group weakly depends on X (number of phenyl rings) for $X > 2$.

The energy maps shown in Fig. 4.6 were obtained via the following steps: i) each molecule is first geometrically relaxed individually, as in the gas phase; ii) two or more molecules are placed in various relative positions and the total energy of the resulting box is computed as is, without geometrical relaxation; iii) the binding energy (in each configuration) is extracted by subtracting the total energy of the isolated constituting molecules; iv) results are presented as energy maps (Fig. 4.6), with colored (resp. white) areas corresponding to binding (resp. anti-bonding) configurations, and isolines for improved readability.

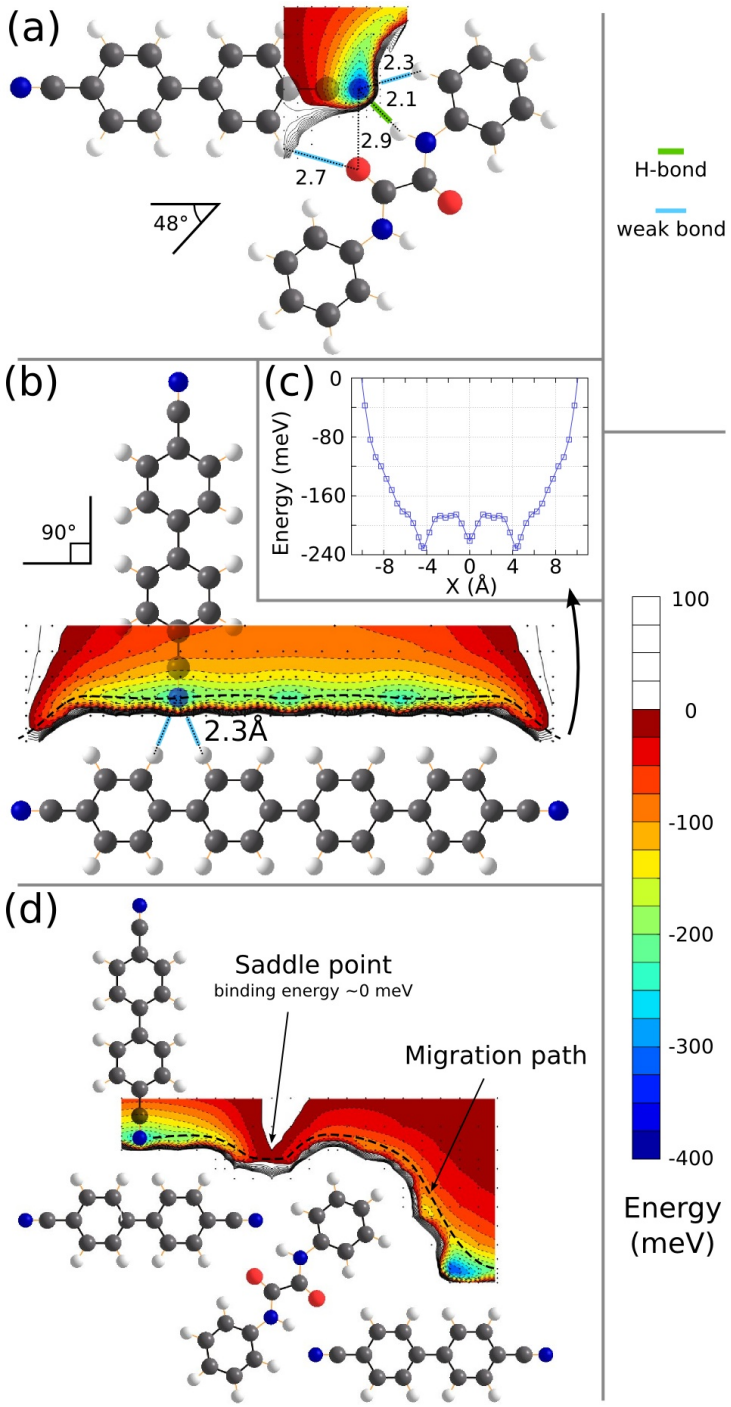

FIGURE 4.6. Energy maps of the 3 studied binding regions. Each black dot on the maps (more than 450 in total) is one simulation of rigidly displaced molecules, and gives the position of the binding nitrogen atom. Colored areas of the interpolated full energy maps correspond to negative formation energy, hence binding zone, while positive formation energy areas are white. Isolines mark 25 meV steps. Dark green lines mark classical hydrogen bonds, whereas light blue ones highlight weak attractive interaction. (a) Binding of NC-Ph_2-CN (2DC) with DOA. (b) Binding of 2DC with 4DC. (c) Evolution of the formation energy versus translation along the host 4DC. (d) Migration region around the 2DC–DOA–2DC link.

The first result (Fig. 4.6a) is the binding energy map of a 2DC with a DOA. The angle of 48° between the 2DC and the DOA comes from a previous full minimization showing this is the equilibrium angle. It is found that the binding energy reaches 340 meV at its maximum. In this equilibrium configuration shown, the closest distance between N and H atom is 2.1 Å (green thick line in Fig. 4.6a). It is interesting to note that three interactions contribute to this link: CN$\cdots$HN, CN$\cdots$HC$_{ph}$ and C$_{ph}$H$\cdots$OC. The first one is a classical hydrogen bond. The two others will be simply referred to as weak bonds (blue thin lines in Fig. 4.6). The contribution of each bond was evaluated in two steps. First, the binding energy of the configuration in Fig. 4.6a was computed with the carbonitrile group of the 2DC replaced by a simple hydrogen. It was found to be ∼70 meV, and corresponds to the contribution of the C$_{ph}$H$\cdots$O bond. Then, looking at the shape of the initial energy map, especially when the carbonitrile group is next to the HC$_{ph}$ group and relatively far from the HN group, we conclude that the CN$\cdots$HN and CN$\cdots$HC$_{ph}$ bonds contribute up to 180 meV and 90 meV respectively. Thus, we can infer that the binding between a 2DC and a DOA comprises a 50% contribution of the CN$\cdots$HN bond, 30% of the CN$\cdots$HC$_{ph}$ interaction and 20% of the C$_{ph}$H$\cdots$OC interaction.

In the model shown in Fig. 4.4 however, the relative position of molecules is slightly different from this lowest energy configuration, revealing the effect of the substrate periodicity in the positioning of molecules. The angle is closer to 43°, and the position of the CN group of 6DC atom is further away from the OC group of the DOA. Using this exact position of our model, we find a binding energy of 230 meV, to be compared with the 340 meV of the theoretical equilibrium position. To complete the picture, a cooperative effect of 40 meV per linkage is calculated, when two 2DCs (instead of just one) are connected to one DOA. This supplemental energy depends only to a minor extent on the exact position of 2DC and DOA molecules (theoretical equilibrium or experimental position), or on the number of phenyl rings in NC-Ph$_X$-CN molecules (2 and 3 tested). The

binding energy holding together the bimolecular chain is thus evaluated to be ∼270 meV per bonding motif.

The second result shown in Fig. 4.6b is related to the binding of two 6DC molecules perpendicular to each other (2DC with NC-Ph_4-CN (4DC) in our calculations). It was found that the attractive zone for the carbonitrile group of the 2DC molecule runs all along the side of the 4DC molecule. However, the energetically most favorable sites are located in between the phenyl rings, with a preference for the end groups, exhibiting a maximal binding energy of 235 meV. At this position, the nitrogen is at a distance of 2.3 Å of both nearest hydrogen atoms. Two weak bonds seem to be participating to the link, partly explaining the particular shape of the energy map. The hopping energy barrier between neighboring sites along the 4DC molecule is found to be as weak as 45 meV (see Fig. 4.6c). Finally, here again, the model shown in Fig. 4.4 is slightly different from the theoretical equilibrium configuration shown in Fig. 4.6b, both regarding the position and the size of the host molecule. The impact of the number of phenyl rings of the host molecule is found to be minimal, ∼10 meV. The change in position however causes a stronger decrease in the binding energy, yielding a final value of 185 meV (2DC connected to 6DC).

These two results confirm the observed larger strength of the $6DC_{ch}$–DOA bond over the $6DC_{ch}$–$6DC_{ru}$ bond. The remaining question about the diffusion properties of $6DC_{ru}$ along the $6DC_{ch}$–DOA chains is addressed in Fig. 4.6d. The binding energy of one $2DC_{ru}$ was computed in a large area covering the pathway from one $2DC_{ch}$ to the next, over an DOA. One can clearly see the saddle point at the junction of the $2DC_{ch}$ with the DOA. The binding energy at this point is found to be almost zero, yielding a hopping energy equal to the binding energy of the $6DC_{ch}$–$6DC_{ru}$ bond (185 meV). However, this hopping energy accounts only for one side of the $6DC_{ru}$ migration, and a more thorough consideration of the migration mechanism is essential to assert the combined effect of both sides. This investigation is presented in Fig. 4.7.

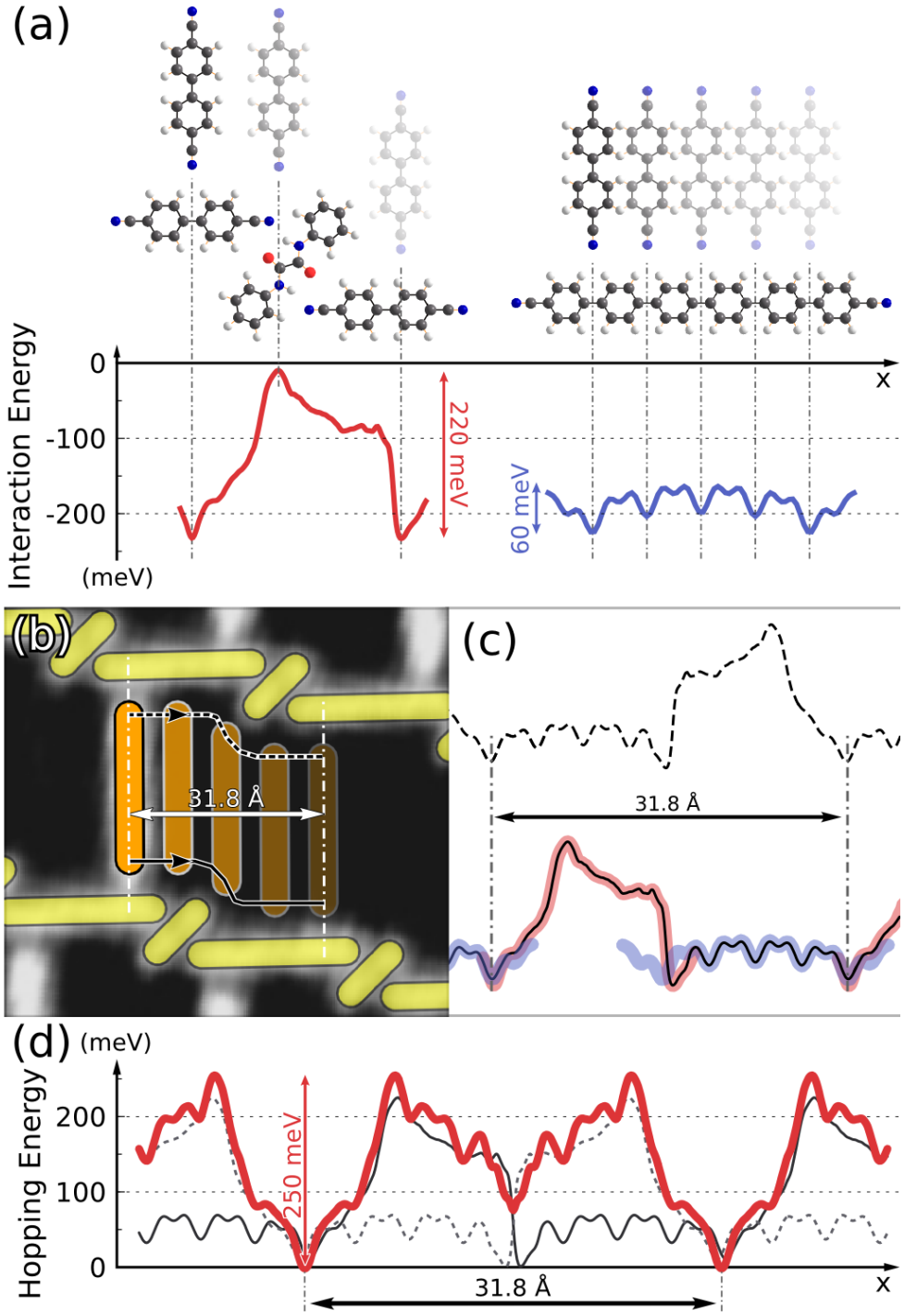

FIGURE 4.7. Prospective study of the migration path of $6DC_{ru}$ between two $6DC_{ch}$–DOA chains. a) Computation of the interaction energy along the two parts of migration path: the step and the straight part. b) A migration path drawn from a STM picture, namely the simple translation of the $6DC_{ru}$ along the $6DC_{ch}$–DOA chain guides. c) Reconstruction of the interaction energy along the full migration path, for each side. d) Sum of both contributions, plotted with respect to the stable state energy. The effective hopping energy barrier is 250 meV.

In order to get an estimate of the effective hopping energy barrier for the migration of a $6DC_{ru}$ molecule from one stable position to the next, I tried to reconstruct the full interaction energy curve all along a likely migration path drawn from STM pictures (Fig. 4.7b). This was achieved in 4 steps: i) the whole migration path is decomposed into the step part and the straight part, and DFT simulations (notably Fig. 4.6d) are used to determine the minimal energy path along x (Fig. 4.7a). The hopping energy barrier between the minimal energy configurations around the step reaches 220 meV. ii) The two parts of the interaction energy (step and straight part) are merged to get the full contribution of one $6DC_{ch}$–DOA chain to the migration energy curve (Fig. 4.7c, plain line). iii) The curve is mirrored to get the contribution of the other side's $6DC_{ch}$–DOA chain (Fig. 4.7c, dashed line). The two curves are aligned along x so that the extremal stable positions coincide (dot dashed lines), as seen in the STM picture (Fig. 4.7b). iv) The two contributions are summed to get an estimate of the migration energy curve. The effective hopping energy barrier now reaches only 250 meV (and not two times 220 meV), because of the misalignment of the saddle point from both sides. This means that the saddle point exhibited in Fig. 4.6d is not crossed simultaneously on both sides, but subsequently.

The calculated hopping energy is in fair agreement with our experimental findings from the Arrhenius analysis (hopping energy barrier of 205 meV), and fits even better when one considers the occurrence of the possible rotations of the $6DC_{ru}$ molecule. I indeed carried out a manipulation experiment at 10 K in which I pushed the $6DC_{ru}$ molecules along the chain direction. The images between each manipulation step are merged into a movie. Even though this mobility pathway is different form thermal excitation, the positions at which the $6DC_{ru}$ molecules reside after the manipulation process corroborate the presented scenario of guided molecular motion.

Anisotropic mobility is an important process in different nanosystems. At the appropriate temperature it governs the diffusion of metal adatoms [109] resulting in the growth of 1D structures [110]. In a similar manner, small organic molecules [111] as well as their larger analogs [100, 112, 113, 114] translate by this elementary process. In contrast to these systems, which rely on the anisotropic properties of the particular system, the necessary 1D guides are created on an isotropic surface by hierarchic self-assembly of appropriately designed tectons. It has been demonstrated that the diffusion of the mobile species is controlled by the interaction with the guides, which represents a novel approach to tailor molecular dynamics on surfaces in a universal fashion. Hierarchic assemblies may be generally useful to direct molecular motion *via* the tailored borders.

4.2.3. Conclusion

In summary, the self-assembly of a hierarchic bimolecular network of the ladder-type have been achieved in which, at temperatures exceeding ∼70 K, 1D diffusion of large organic molecules takes place. Theoretic analysis clarifies that hierarchy is introduced into the chiral supramolecular structure by the energetics of the different bonds established between the two organic species, including a novel carbonitrile – oxalic amide motif. The dynamics of the mobile species is consistent with an Arrhenius-type of hopping and steered by the interaction with the ladder side rails. These results demonstrate the usefulness of hierarchic design and reveal a new approach to guide molecular motion at nanostructured surfaces.

4.2.4. Methods

The scanning tunneling microscopy (STM) experiments were performed using a home-built ultrahigh vacuum (base pressure $3x10^{-11}$ mbar) low-temperature STM. The Ag(111) substrate was prepared by repeated cycles of Ar^+ sputtering and annealing to 750 K to obtain flat terraces separated

by monatomic steps. The two molecules, sexiphenyl dicarbonitrile (6DC) and N,N-diphenyl oxalic amide (DOA) were deposited from a double organic molecular beam epitaxy source with the quartz crucible at 572 K and 467 K for 6DC and DOA respectively, while keeping the substrate at 300 K. Both sequential and simultaneous deposition led to similar results. Following preparation, STM data were acquired at a substrate temperature (T_{sub}) as indicated, typically 10 K. The systems dynamics was probed in the range from 70–120 K.

For the theoretical investigation, we have used the Projector Augmented-Wave approach as implemented in the `ABINIT` code [115, 116], within the Local Density Approximation for the exchange-correlation energy. The cutoff energy used is 30 Ry. Since the code imposes periodic boundary conditions in all three directions, we ensured that the simulation box allowed a minimal distance of 8 Å between the molecules and their periodic images. We evaluated the subsequent error on total energy to be then lower than 10 meV. As molecules are rigidly displaced to obtain the energy maps, we checked the impact of geometrical relaxation on the binding energy by fully relaxing calculations for the lowest energy configurations, and we found energy differences lower than 10 meV. Also, for simplicity reason, flat molecules were used in the calculations, whereas 6DC are known to present a tilting between the phenyl rings [12, 117]. A test calculation involving two 2DC molecules revealed that impact on binding energy of the tilting is lower than 15 meV, despite the energy difference of almost 50 meV between tilted and untilted isolated 2DC molecule. The full energy maps displayed in Fig. 4.6 are obtained using a Delaunay interpolation between the computed points.

5 Steering On-Surface Self-Assembly Of High-Quality Hydrocarbon Networks With Terminal Alkynes

5.1. Introduction

As it has already been mentioned in the introduction C–H$\cdots\pi$ bridges represent versatile ingredients for the supramolecular design [118, 119] . In this context, terminal alkynes are especially interesting because they unite comparatively strong proton donor capabilities, which result from the high acidity of the alkynyl atom, with great versatility resulting from the fact that their π system can simultaneously act as proton acceptor [120, 118]. Initially, they have been recognized as secondary structural force in crystals of molecules featuring at the same time classical hydrogen bonding functionalities [121, 120, 122, 123]. Later it was demonstrated that in the absence of such functionalities the terminal alkyne interactions are the dominant ones [124, 125, 126]. It is worth to mention that the competing interaction with the π-system of an aromatic ring is not established in any of these crystal structures [124, 125, 126]. Often infinite zigzag patterns of nearly T-shaped arrangements of the ethyne groups are established [120, 122, 127, 124, 125], but also three- and six-membered synthons have been reported [127, 125, 128]. A somewhat controversially discussed topic is the manifestation of the cooperative effect, *i.e.* an increase of the binding energy per bond with increasing number of connected bonds [129, 120], in synthons built-up by terminal alkynes. On

the one hand, cooperative stabilization is suggested by experimental results [120, 122, 130, 125, 131] as well as early quantum chemical calculations [122], on the other hand such effects are not found with the same methods in cases appearing quite similar [123]. A more recent theoretical investigation focusing on ethyne concluded that no cooperative effect appear in between C_2H_2 molecules and only small additional stabilization (10%) results in the presence of water [132]. It could be tentatively concluded from this discussion that the backbone to which terminal alkynes are attached might have a pronounced influence on the manifestation of cooperative gain.

With the aim of a purposeful creation of functional nanostructures on surfaces, considerable effort has been devoted to understand how synthons known from 3D supramolecular chemistry adapt to the novel, 2D environment [7, 78, 133]. Examples of binding motifs being successfully transferred into two dimensions include the classical O−H···N, N−H···O, and N−H···N hydrogen bridges [104, 134, 81, 99]. Self-complementary multiple H bond synthons were used to create porous networks [11, 89] or bicomponent lines [90] as well as to steer conformation-selective self-assembly [135]. Cyclic binding motifs were stabilized by benzonitrile interactions leading to controlled supramolecular aggregates [136] and regular porous networks of varying symmetry [83, 12]. In contrast, terminal alkynes have so far been disregarded in the field of on-surface supramolecular chemistry. Only one, very recent study addresses the formation of regular hexameric aggregates of ethynylbenzene on Au(111) [137].

Through this chapter I contribute to filling this knowledge gap by presenting a systematic investigation of the self-assembly capabilities of multitopic terminal alkyne functionalized molecules in a 2D environment, namely on the Ag(111) surface in ultra-high vacuum conditions. The triple bond of phenylacetylene becomes often transformed to a formally double bond due to adsorption on more reactive substrates like Pt or Cu [138, 139, 140], but it stays intact on Au(111) [137]. Therefore it is an open question if

the terminal alkynes preserve their supramolecular capabilities on the silver surface. The low-temperature scanning tunneling microscopy (STM) reveals long-range ordered crystal-quality networks surface which are stabilized via novel, cyclic binding motifs and feature small nanopores. Using density functional theory (DFT) calculations I address the influence of the surface on the bonding capabilities of the ethyne moieties including the effect of cooperativity and discuss the delicate interplay between molecule-surface and intermolecular interactions leading to the extended supermolecular layer. Moreover, the present findings are potentially important regarding the homocoupling reaction occurring with the same building blocks at higher temperatures, which I discuss in the Chapter 6.

5.2. Results and Discussion

In order to study creation of networks based on interaction between terminal ethyne groups we employed 1,3,5-triethynyl-benzene (TEB (1)) and 1,3,5-tris-(4-ethynylphenyl)benzene (Ext-TEB (2)) (Scheme 1). TEB consists of a benzene ring with three acetylene groups attached to the carbon atoms in positions 1, 3, and 5. The molecule exhibits D_{3h} symmetry and the distance between hydrogen atoms of the terminal alkyne groups amounts to 8.78 Å.

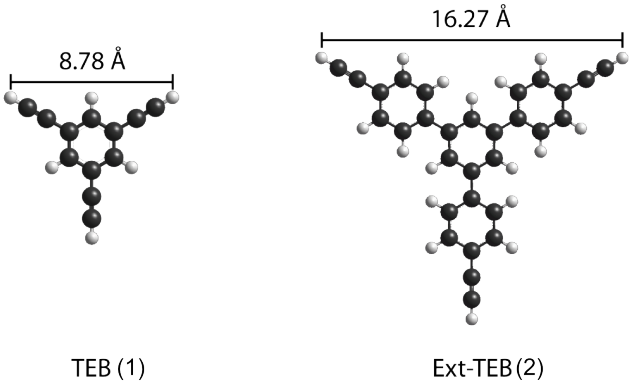

FIGURE 5.1. 1,3,5-triethynyl-benzene (TEB) and 1,3,5-tris-(4-ethynylphenyl)benzene (Ext-TEB)

After 1 minute exposure of the substrate at $T_{sample} = 180$ K long-range ordered regular nano-porous networks were observed (Fig. 5.2). In the STM images the molecules appear as bright triangular protrusions. The triangles are arranged such that they form zig-zag lines (orange), neighboring lines are laterally offset as indicated in Fig. 5.2a. Three molecules from one zig-zag line join three molecules from an adjacent line to construct a six-membered ring (green hexagon) which is enclosing a nanopore. From the uniform apparent height of the organic units and absence of a Moiré pattern we conclude that the produced network is commensurate with the underlying atomic lattice. A zoomed image (Fig. 5.2b) details that the building blocks can be identified as triangles (blue), each with one corner pointing oppositely with respect to the $[\overline{11}2]$ direction. Going along the direction from the center of the triangle to the center of the pore, every

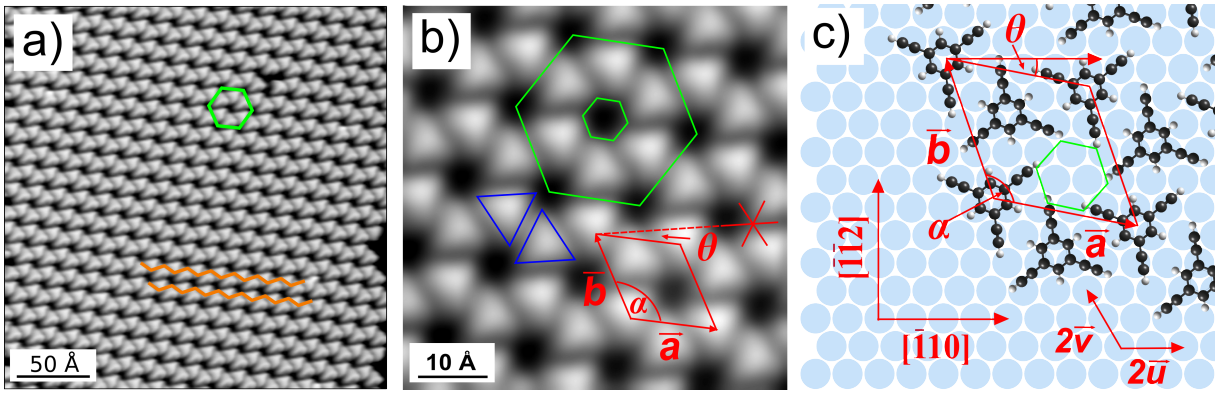

FIGURE 5.2. (a) STM topograph of TEB network ($U = -0.3$ V, $I = 0.1$ nA). (b) A zoomed image of the network with the corresponding elementary cell ($U = -0.1$ V, $I = 0.1$ nA). A small green hexagon represents a pore enclosed by hydrogen atoms of the respective molecules. (c) Model of the TEB network. The unit vectors $\vec{a}$ and $\vec{b}$ enclose the angle α. The angle θ is defined between the high-symmetry direction $[\bar{1}10]$ and $\vec{a}$. The primitive vectors of the Ag(111) surface are $\vec{u}$ and $\vec{v}$.

triangle is pointing left of the center of the pore, thus the superstructure exhibits organizational chirality [141, 142]. Accordingly, the six-membered rings frame a chiral pore (small green hexagon in Fig. 5.2b). Placing the corners of the pore at the tip terminations of the molecules, defined by an apparent height of 20% of the molecule's maximum apparent height, one can assign a maximal diameter $D_e = 5.8$ Å to the cavity. Domains with different principal directions and the opposite chirality as compared to those displayed in Fig. 5.2 were also found on the substrate (Fig. 5.4a,b).

The unit cell and its orientation with respect to the substrate (Fig. 5.2b, red), as determined by atomically resolving the bare substrate, were obtained by averaging the values of four STM images (54×54 Å^2) recorded at the same area with different slow scanning directions to minimize the error caused by drift. The measured lengths of the vectors are $|\vec{a}| = \left|\vec{b}\right| = (13.1 \pm 0.3)$ Å and $\alpha = (119 \pm 1)°$. The angle θ between $\vec{a}$ and one of the ¡$\bar{1}$ 1 0¿ high-symmetry directions (red star) is 11°.

Guided by the experimental values, we construct the adsorption model depicted in Fig. 5.2c with ball-and-stick model of the molecules on the hexagonal Ag(111) lattice represented by blue circles. With the definition of the primitive vectors of the Ag(111) substrate given in Fig. 5.2c the

elementary cell can be written in matrix representation as

$$\begin{pmatrix} \vec{a} \\ \vec{b} \end{pmatrix} = \begin{pmatrix} 4 & -1 \\ 1 & 5 \end{pmatrix} \begin{pmatrix} \vec{u} \\ \vec{v} \end{pmatrix}.$$

With the nearest-neighbor distance of 2.89 Å we obtain for the commensurate superstructure the values $|\vec{a}| = \left|\vec{b}\right| = 13.23$ Å, $\alpha = 120°$ and $\theta = 11°$ agreeing with the experimental findings within an error smaller than 1%. From the model is it obvious that the zig-zag lines follow $\vec{a}$, while the offset between adjacent lines is given by $\vec{b}$. The surface registry proposed by the model was not determined through experiments, because simultaneous molecular and atomic resolution was not achieved. Instead, the lateral displacement between the organic layer and the metal substrate was optimized to yield a high-symmetric arrangement. On the basis of this, we suggest that the centers of the phenyl moieties sit on hollow sites for which we can not distinguish between hexagonal close-packed (HCP) and face-centered cubic (FCC) hollow sites, since we take into account the first substrate layer only.

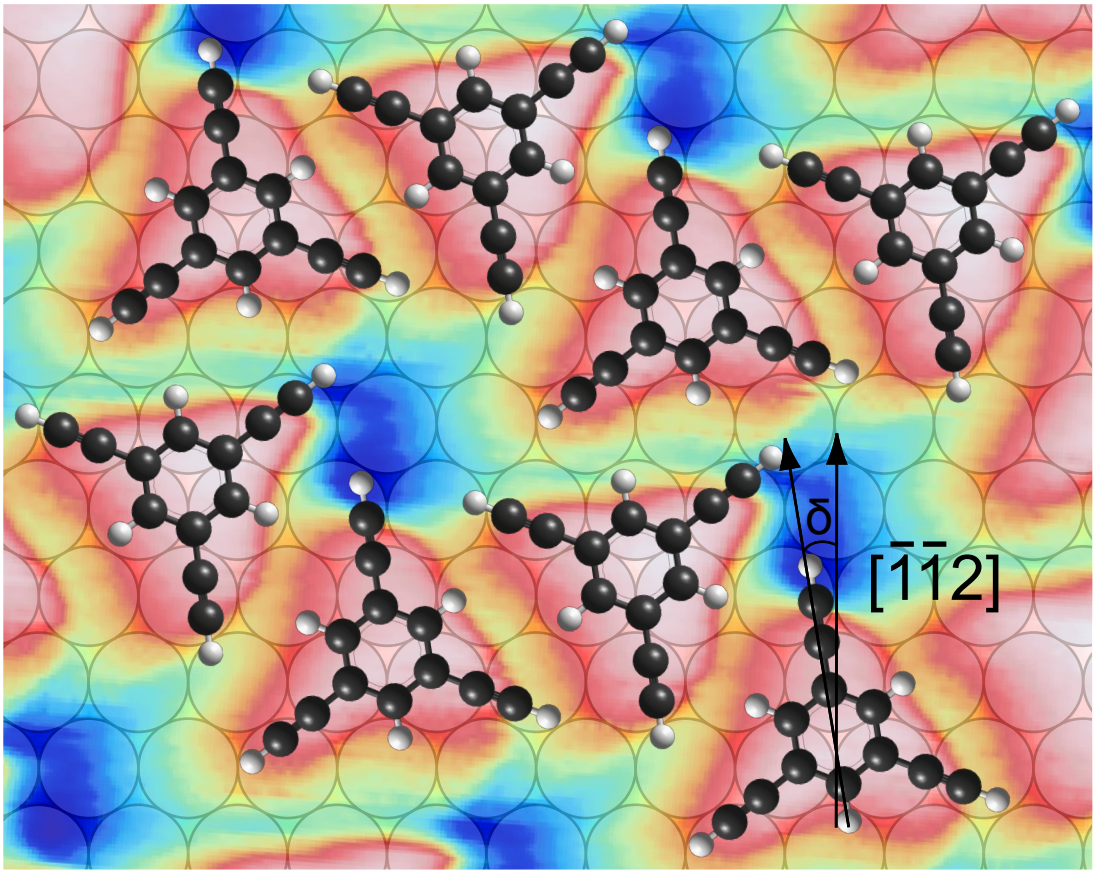

FIGURE 5.3. Ball-and-stick models of TEB were superimposed onto a high-resolution STM image to determine the rotation angle δ.

An enlarged model (Fig. 5.4c) highlights the enclosed pore and the supramolecular chiral organization. Placing the corners of the hexagon defining the cavity on top of the H atom centers we find that the largest diameter of the hexagon amounts to $D_t = 5.78$ Å. Furthermore, the ethyne groups are not aligned with the bridge or top sites. By superposing a HYPERCHEM calculated model onto high-resolution STM data (Fig. 5.3), we found the best agreement for the molecular outlines assuming a rotation such that the terminal alkynes enclose an angle $\delta = (8 \pm 2)^\circ$ with the ¡$\bar{1}\,\bar{1}\,2$¿ directions and accordingly $(-8 \pm 2)^\circ$ for the opposite chirality. The rotation of the TEB molecule away from being oriented along the substrates high-symmetry directions is most likely originating from the intermolecular interaction of the terminal ethyne groups, but indirect substrate-mediated interaction could in principle also interfere. For a first, very simple analysis,it suffices to assume as the sole driving force an attraction between a

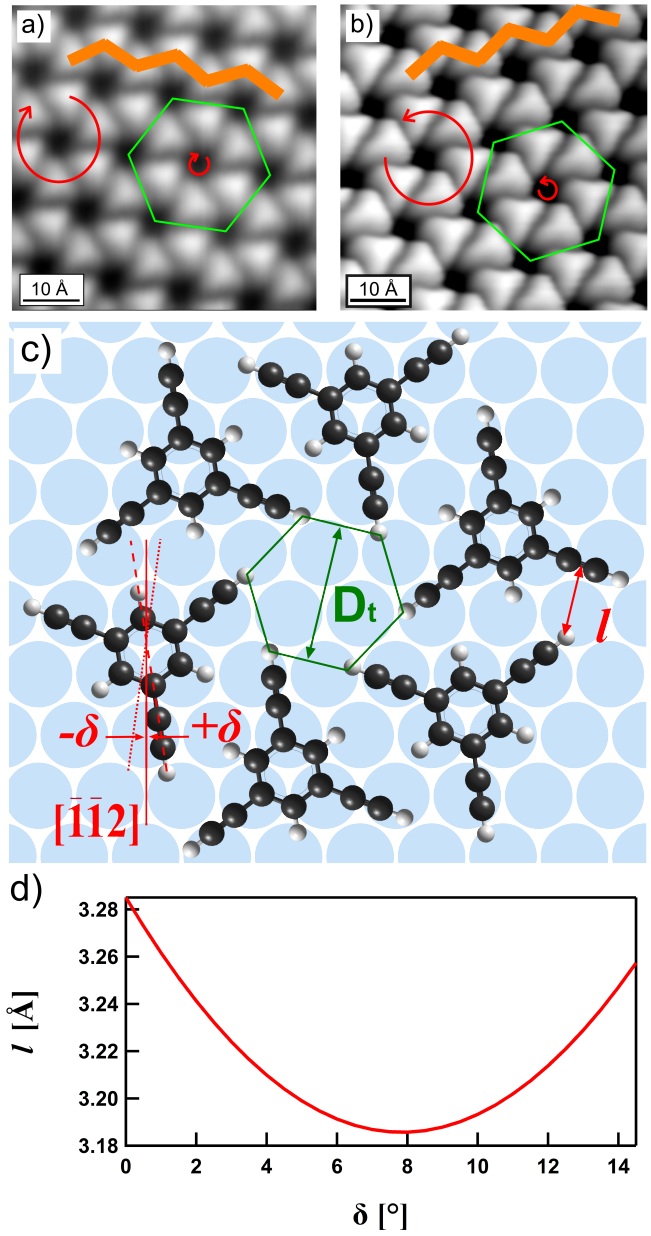

FIGURE 5.4. STM images of two different domains of ordered TEB networks showing (a) the left and (b) right enantiomorph. Brown zig-zag lines show the two different principal directions which are correlated with the handedness. Green hexagons with corners at the center of the nanopores highlight the six-membered rings enclosing the chiral pores. The chiralities are denoted with red arrows. (c) Pore of a diameter D_t enclosed by terminal hydrogen atoms (green), distance from a terminal hydrogen atom to the center of ethyne group on the nearest-neighbor molecule l and the angle δ describing the rotation away from the $[\bar{1}\bar{1}2]$ direction (red). (d) Ethyne bonding distance l as a function of the angle δ.

terminal hydrogen atom and the center of the nearby ethyne group. We calculated the distance l between the two atom centers as a function of the angle δ. Interestingly, a parabola with a minimum at $\delta = 8°$ (Fig. 5.4d)

was found, which nicely matches the STM data. Taking into account the oversimplifications of the assumed attraction, the quantitative agreement certainly cannot be regraded as conclusive. Nevertheless, this matching can be taken as a strong indication that the terminal ethyne groups are indeed the dominating driving force for the rotation of the molecules in the network.

In order to gain deeper understanding of the underlying interactions that drive the network formation, DFT calculations were carried out. In particular, I was interested in how the interplay between molecule-molecule and molecule-surface interactions affects the stability and the long-range order of the network. First, the attention was devoted to the intermolecular interactions in gas phase calculations of a TEB dimer (Fig. 5.5a) and the periodic TEB network (Fig. 5.5b). For the TEB network both the

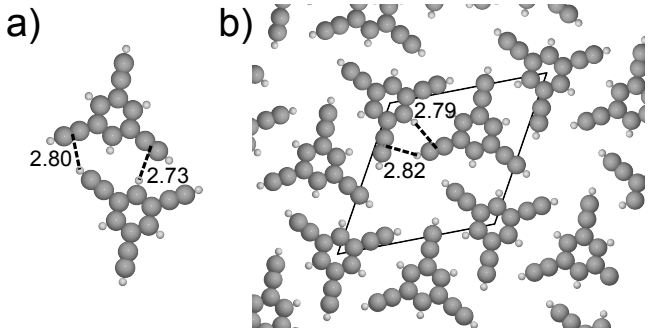

FIGURE 5.5. (a) Gas phase dimer (b) Network made of TEB molecules with the corresponding distances in Ångström.

internal structure and the length of the unit cell vectors were optimized while $\alpha = 120°$ was kept constant. To compare the bonding strength between dimer and network, we can define the binding energy of a molecule per molecule-molecule interaction for the dimer as

$$E_{bind,dim} = -(E_{dim} - 2E_{mol})$$

and for the network as

$$E_{bind,net} = -\frac{E_{net} - 2E_{mol}}{3},$$

where E_{mol}, E_{dim}, and E_{net} are the total energies per unit cell of the TEB molecule, the TEB dimer, and the TEB network, respectively, on the surface. The denominator 3 is due to the fact that in the network each molecule is interacting with three surrounding ones, whereas the factor 2 describes two molecules per elementary cell. In this theoretical framework a more negative energy of a single parameter (E_{mol}, E_{dim}, or E_{net}) means a more stable situation, while a positive binding energy (E_{bind}) is associated with stabilization due to the interaction of the isolated parts. $E_{bind,dim}$ and $E_{bind,net}$ amount to 0.20 and 0.22 eV respectively, hence the strengths per molecule-molecule interaction are comparable and the long-range order of the network has no recognizable cooperative effect on the individual interactions. The energy gained per molecule by formation of the periodic 2D sheet is

$$E_{form} = -\frac{E_{net} - 2E_{mol}}{2} = 0.33 \text{ eV}.$$

For the isolated molecular sheet, the optimized length of the two unit cell vectors is 12.77 Å, hence theory predicts an optimal lattice constant of almost 0.5 Å shorter than the one experimentally observed. The difference is attributed to the molecule-surface interaction which obviously has a great influence on the self-assembly of TEB on Ag(111). Thus, in the next step of the DFT analysis we explicitly take into account the substrate. For the adsorption of a single TEB molecule on Ag(111) four high-symmetric adsorption geometries were found as local minima (see Fig. 5.6). Notably, the adsorption energy gain, E_{ad}, varies significantly between the different cases and ranges from 1.40 to 1.19 eV from the most to the least stable configurations, respectively. This difference is of the same order of magnitude than E_{form}. Thus the surface is expected to pin the molecules to positions of well-defined registry in agreement with the experimental finding of the formation of a commensurable, long-range ordered network.

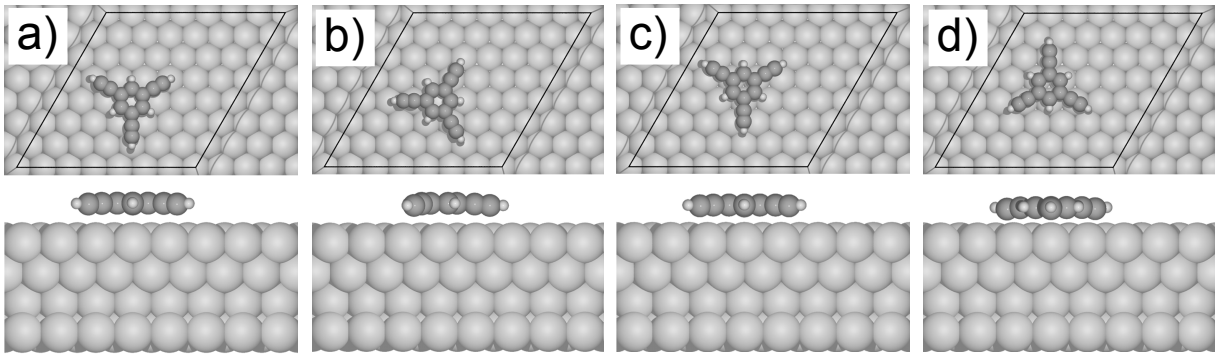

FIGURE 5.6. Top and side views of favorable adsorption geometries for TEB on Ag(111). The binding energies for the different configurations from (a) to (d) are 1.19, 1.25, 1.26, and 1.40 eV, respectively. Black lines in the top views indicate the surface unit cells used in the calculations.

In Fig. 5.8a and b the two most stable adsorption configurations of TEB on Ag(111) are depicted. In both cases the phenyl ring is centered above a hollow site, while the ethyne triple bonds are aligned with bridge and on top positions in Fig. 5.8a and b respectively. Note that FCC and HCP hollow sites were indistinguishable, with energy differences smaller than 5 meV. Fig. 5.8c illustrates the most stable geometry for the TEB network on the Ag(111) surface determined under the constraint of the model unit cell. Other configurations of networks representing local energy minima are given in Fig. 5.7.

The superstructure can be understood as consisting of entities alternatively adopting the two most stable geometries for the single molecules. However, all molecules are rotated imprinting chirality to the nanoporous phase, whereby the rotation angle $\alpha = 8°$ is in excellent agreement with the experiments. From the comparison of the adsorption configurations of the single organic units and the periodic assembly it is obvious that the rotation results from the intermolecular attraction focused on the terminal alkynes generating a torque around the phenyl ring centers which are pinned at hollow sites the substrate. In Fig. 5.8c also the distances between the centers of ethyne triple bonds and nearby hydrogen atoms are indicated. Compared to the isolated organic sheet (Fig. 5.5b), the intermolecular bonding distances are substantially larger under on-surface

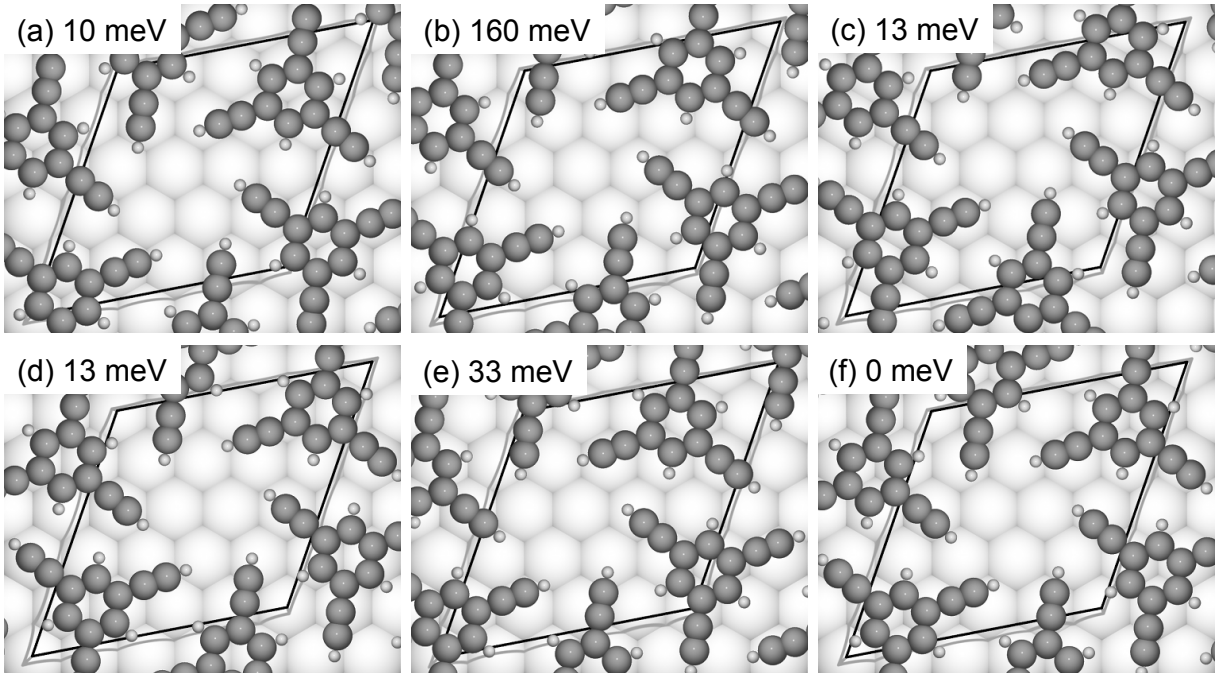

FIGURE 5.7. Comparison of networks with the TEB molecules at different registry above the Ag(111) surface. All structures have been optimized as described in the Methods section in the manuscript. The energies are given with respect to the most stable configuration (f) as the energy per unit cell. It is clear that adsorption sites with the benzene core above hollow sites are energetically favorable, while the top sites are highly disfavored.

conditions, due to the commensurability with the Ag(111) surface putting a constraint on the intermolecular distances. The energy gained per molecule by formation of the network on the surface is given by

$$E_{form,sub} = -\frac{E_{net,sub} - 2E_{mol} - E_{sub}}{2} - E_{ad},$$

where $E_{net,sub}$ and E_{sub} are the total energies per unit cell for the network on the surface and the clean surface, respectively. A stabilization by 0.11 eV/molecule with respect to the single molecules on the substrate was found, while for the isolated organic sheet E_{form} is 0.33 eV/molecule. The smaller energy gain on the surface has two origins.

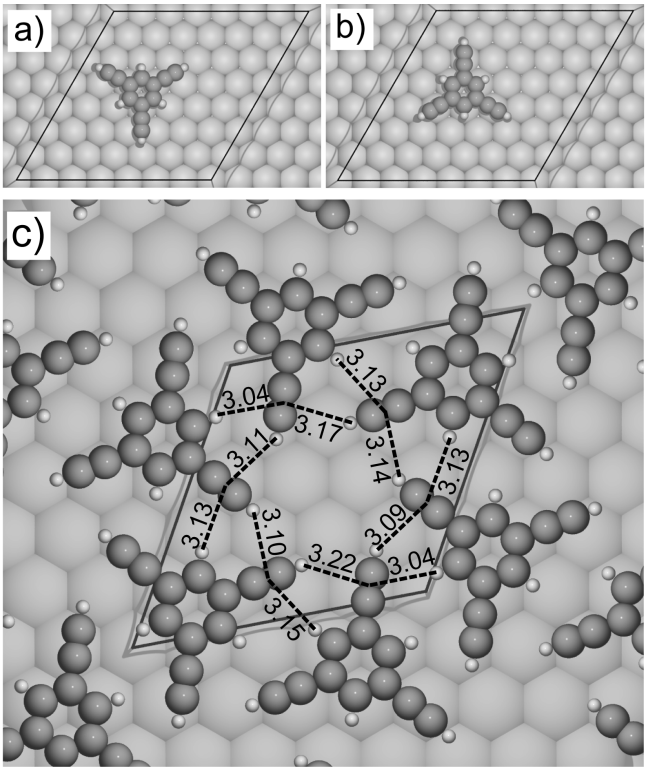

FIGURE 5.8. DFT optimized adsorption geometries of isolated molecules and the periodic network. Black lines indicate the surface unit cell used in the calculations. (a) and (b) Isolated TEB units adsorb on Ag(111) in a highly symmetric manner. (a) In the second most stable situation ($E_{ad} = 1.26$ eV) the phenyl moiety is centered over fcc hollow site and terminal alkynes are over bridge positions. (b) Most stable registry ($E_{ad} = 1.40$ eV) with the phenyl center over hcp hollow site and alkynes over on top positions. (c) The geometry of the entire network is characterized by molecules being centered over hollow sites with terminal alkynes rotated away from the original bridge and on top alignment. Note that the enantiomorph opposite to the one of the experimental model (Fig. 5.2c) is depicted.

First, due to the commensurability of the network with the surface, discussed above, the intermolecular distances are restricted to a regime in which $E_{bind,net}$ has not yet reached its maximum. Secondly, the adsorption configuration of each molecule in the superstructure is disrupted from the corresponding most favorable geometry reducing E_{ad}. The rotation-induced lowering of E_{ad} is reflected in the fact that the average adsorption heights for an isolated molecule and a molecule integrated in the network are 2.93 Å and 3.15 Å , respectively. In other words, there is a very delicate balance of energy gain due to intermolecular interactions and loss by disrupting molecule-surface interactions that control the on-surface network formation.

Notably, the DFT calculations predict an energetically favorable network formation, and are also able to describe the rotation of the TEB molecules in the network. This is a non-trivial task due to the fine balance between different interactions (see above). In order to model the formation of the network, the previously mentioned energy cost and gain need to be correctly reproduced in the calculations. In particular, the molecule-surface interactions are mainly governed by non-local van der Waals interactions, which description is still a hot topic of discussion in the DFT community. These intriguing results show that the van der Waals density-functional combined with the optimized form of Becke 86 exchange[143], gives a good qualitative description of the hierarchy between molecule-molecule and molecule-surface interactions, correctly describing the rotation of the molecules as well as predicting a stable network formation, and I suggest this methodology to be a valuable tool helpful for the analysis of similar types of systems.

Next I analyze the stabilization of the superstructure in terms of distinct bonds. Fig. 5.11 shows a charge difference plot of an isolated TEB sheet, illustrating the electron accumulation (red) and depletion (blue) induced by the formation of the network as compared to non-interaction gas phase molecules. The intermolecular bonding in the TEB network is

mainly characterized by two types of non-covalent bonding motifs. One is a weak H-bond between ethyne groups (green dotted ellipse) indicated by accumulation of electron charge around the ethyne group donating its π-system to the hydrogen bridge and depletion of electrons around the H atom donated by the other ethyne group. For the second intermolecular contact, namely again between an ethyne π-system and the nearby methine unit of the neighboring phenyl moiety, I suggest the proton acceptor ring interaction (PARI)[27] as the driving force. As demonstrated very recently[27], the in-plane interaction between a functional group bearing the potential to act as a proton acceptor in a H bridge and a benzene ring presents a special case of hydrogen bonding[144]. This is because the major part of the complexation energy gain is not originating from the methine unit near to the proton acceptor, but from the more remote half of the benzene ring. In the PARI situation the proton acceptor is pointing with its electron lone pair towards the benzene ring. Considering the geometry of the ethyne π-system in the case discussed here the charge difference plot reveals a great similarity and accordingly we attribute the second contact to a PARI. The interpretation that mainly the in-plane π-orbitals contribute to the bonding mechanism is further corroborated by the projected density of states (PDOS) displayed in Fig. 5.9.

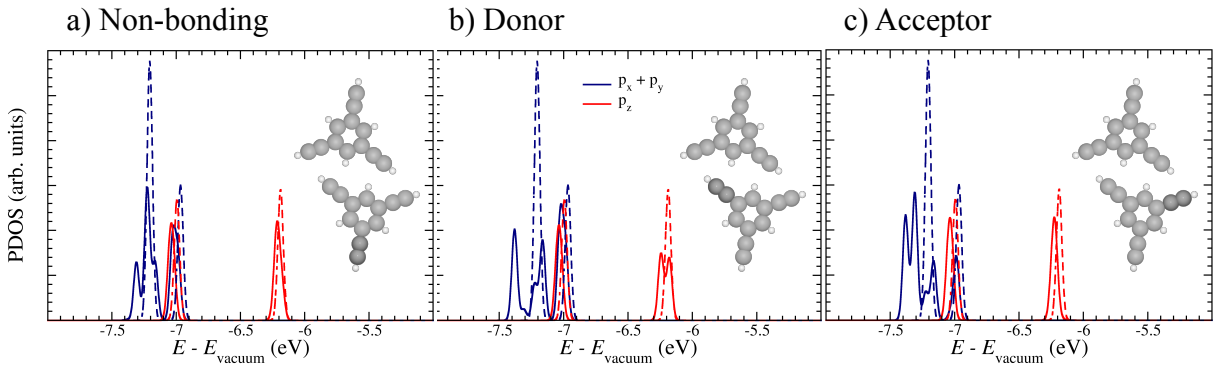

FIGURE 5.9. Projected density of states (PDOS) of three ethyne legs. The in-plane p_x and p_y orbitals are denoted with red color, the out-of-plane p_z orbital with blue.

For the TEB network on the surface very similar charge difference behavior was found (Fig. 5.10a) indicating that the bonding mechanism is preserving its character with the presence of the noble metal substrate. In

order the estimate how much each of the two bonding motifs contribute to the overall binding we constructed an alternative dimer featuring only the PARI (Fig. 5.10b) and compared it to a normal dimer with ethyne-ethyne H bridge and PARI (Fig. 5.10c). The binding energy of the modified dimer is 0.10 eV, hence half the binding energy of a normal TEB dimer. In other words, in the dimer the PARI is contributing significantly to the stabilization. The PARI-related binding energy agrees well with what is expected for a PARI originating from benzene.[27] Even though the PARI contribution is significant, the ethyne-ethyne interaction is expected to have the major influence on the overall network stabilization.

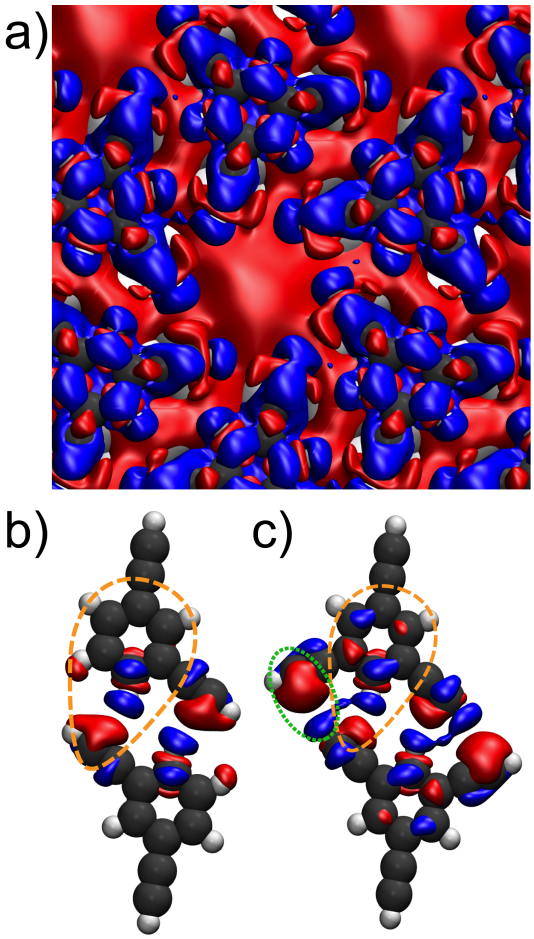

FIGURE 5.10. Electron charge difference plot for (a) the TEB network on the substrate, (b) a modified dimer with only PARI (orange), and (c) a normal TEB dimer in vacuum with PARI and ethyne-ethyne interactions (green). Red and blue are electron accumulation and depletion respectively.

This can be explained by different distances between the ethyne group and the benzene H-atom. Namely, in the TEB network this distance is larger than in the alternative dimer with only PARIs. Hence, we conclude that the PARI contribution is somewhat weakened by introducing the ethyne-ethyne interactions.

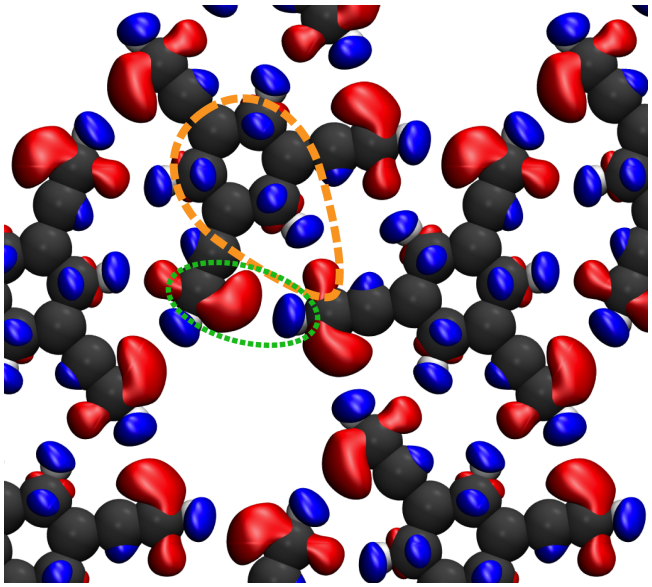

FIGURE 5.11. Electron charge difference plot of a TEB dimer in gas phase, illustrating the electron difference between the dimer and the two TEB constituents geometrically frozen in the dimer configuration. The value of the contours is 0.001e, where red is electron accumulation and blue is electron depletion.

In the following we compare with ethyne-related ordering in a three dimensional environment. It is noteworthy that in case of bulk material the ordering of the molecules featuring terminal alkynes often exhibits folded layer structure.[120, 122, 123, 127, 130, 125, 124, 128] A six-membered cyclic binding motif was reported before,[127] but the alkynes are not laying in the same plane and rather pointing in the opposite directions orthogonal to the plane which contains the binding motif. To the best of our knowledge no indication for appreciable in-plane interactions between ethyne and phenyl moieties have been reported so far. Note that in-plane geometry is a completely different case than the well-established hydrogen bridge between a proton donating ethyne group and the π-system of a benzene ring.[122, 130] Thus the planarity and the PARI contribution to

the stabilization qualify our binding six-membered cyclic binding motif as a novel synthon.

As a generalization step in our study of terminal alkyne-related self-assembly we synthesized 1,3,5-tri-(4-ethynyl-phenyl)benzene (Ext-TEB) (Fig. 5.1). This molecule also exhibits three-fold symmetry, but features additional benzene rings between the central one and the terminal ethyne groups. The H-H distance of the terminal groups is 16.27 Å. After Ext-TEB was deposited onto the Ag(111) surface (T_{sam} = 156 K) two different supramolecular arrangements coexist, namely a compact (CP, Fig. 5.12a) and an open-porous (OP, Fig. 5.13a) phase. Both phases form large domains of high-quality. The CP is very similar to the network made by TEB-molecules, again with a principal direction highlighted by zig-zag chains (orange) in Fig. 5.12a.

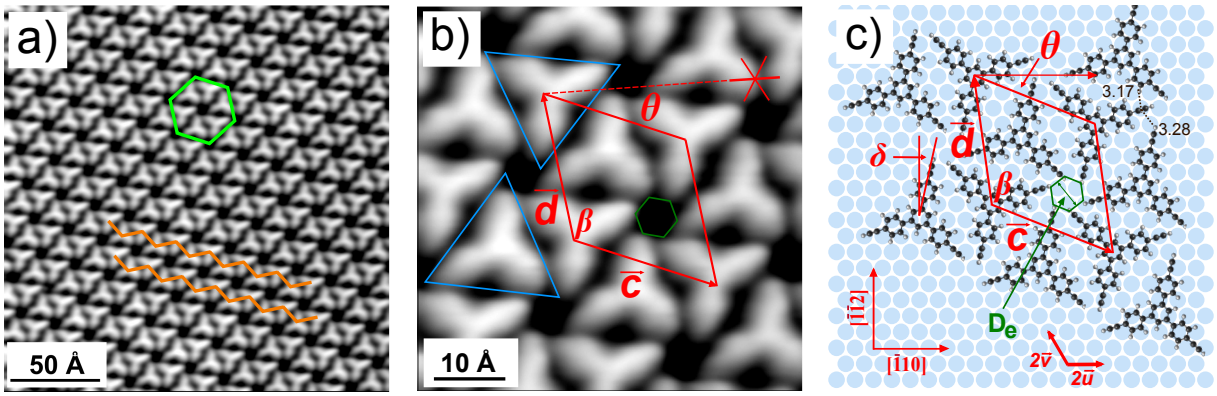

FIGURE 5.12. Compact packed phase of the Ext-TEB network. (a) Large-scale STM topograph showing a long-range ordering of the supramolecular network (U = −0.09 V, I = 0.05 nA). (b) A zoomed image of the network with the corresponding elementary cell. (U = −0.09 V, I = 0.05 nA) (c) Model of the open-porous phase.

Also, six-membered rings (green) enclose a nanopore. A close inspection of a zoomed-in image (Fig. 5.12b) reveals in close analogy to the case of TEB that two types of molecules (blue triangles pointing in different ¡$\bar{1}$ 1 0¿ directions) are present in the superstructure and that the terminal groups are pointing left of the pore center, thus the pores are chiral. The rotation angle is $\delta = 13°$. The diameter of a pore amounts to $D_e = 4.8$ Å i.e. slightly reduced compared to the smaller tecton. Ext-TEB builds up a periodic layer with a rhombic elementary cell. The experimentally determined values for the unit cell are $|\vec{c}| = \left|\vec{d}\right| = (20.0 \pm 0.4)$ Å, angle $\beta = (119.1 \pm 0.4)°$, $\theta = 22°$ (Fig. 5.12b). Within an error of approximately 1%, I propose a commensurate one defined by $|\vec{c}| = \left|\vec{d}\right| = 20.22$ Å, $\beta = 120°$, $\theta = 21.79°$ which is given in matrix representation as

$$\begin{pmatrix} \vec{c} \\ \vec{d} \end{pmatrix} = \begin{pmatrix} 5 & -3 \\ 3 & 8 \end{pmatrix} \begin{pmatrix} \vec{u} \\ \vec{v} \end{pmatrix}$$

with reference to the silver surface basis vectors $\vec{u}$ and $\vec{v}$. With the same definition as in the TEB assembly the maximal pore hexagon diameter amounts to $D_e = 4.76$ Å. Again, the surface registry was unknown, but through symmetry optimizing it was possible to construct a commensurate supermolecular model (Fig. 5.12c), which fits well to the measured data and where the constituents have a well-defined registry with the substrate. I propose that for one molecule type the central aromatic ring is placed on top while the outer rings adopt hollow site, whereas for the other type the registry is inverted. Without further arguments from DFT calculations, we conclude from the pronounced similarity of the circular binding motifs around the pores (cf. Fig. 5.2c and Fig. 5.12c) that also the interactions contributing to the network stabilization carry similar properties. The hydrogen bonds established by the ethyne groups have an average length of 3 Å and the PARI-type bonds manifest with a binding length of 3.17 Å.

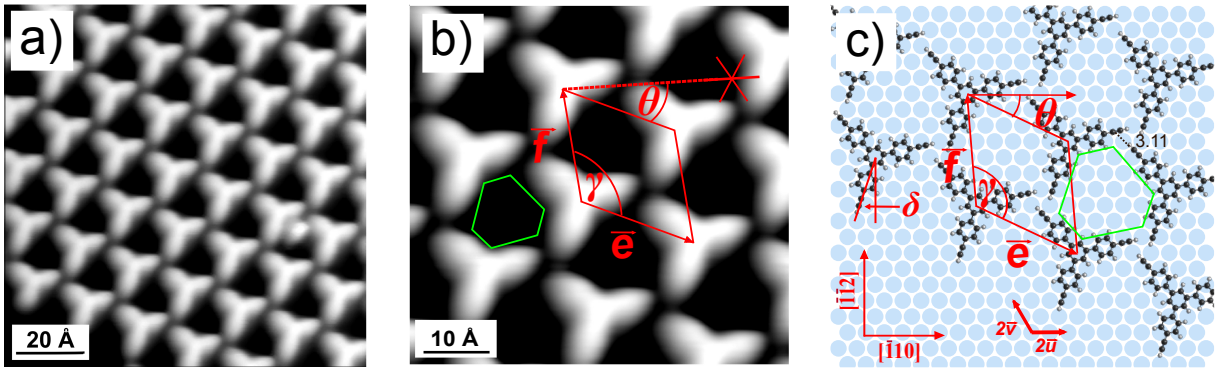

FIGURE 5.13. Open porous phase of the Ext-TEB network. (a) Large-scale STM topograph showing a long-range ordering of the supramolecular network ($U = -0.09$ V, $I = 0.05$ nA). (b) A zoomed image of the network with the corresponding elementary cell ($U = -0.09$ V, $I = 0.05$ nA) (c) Ball-and-stick network model.

Contrary to the two previous arrangements, in the OP all molecules have the same orientation (Fig. 5.13a). Only three ethyne groups (Fig. 5.13b and c) are contributing to the nodal connections between organic units and no pore is enclosed by them. Instead, a larger pore (green) is present in between the molecules. Due to the chirality of the nodal motif, the pores can be understood as three-fold symmetric hexagons featuring three long and three short sides (as depicted in Fig. 5.13b and Fig. 5.13c). Similarly to the previous structures, the complete network can be constructed by successive translations of the rhombic unit cell ($|\vec{e}| = \left|\vec{f}\right| = (17.3 \pm 0.4)$ Å, $\gamma = (119.3 \pm 0.5)^\circ$ $\theta = 26.2^\circ$) defined in Fig. 5.13b. Within an error of 1.3%, the experimental values were translated into a commensurate model superstructure ($|\vec{e}| = \left|\vec{f}\right| = 17.57$ Å, $\gamma = 120^\circ$, $\theta = 25.29^\circ$), which has the matrix notation

$$\begin{pmatrix} \vec{e} \\ \vec{f} \end{pmatrix} = \begin{pmatrix} 4 & -3 \\ 3 & 7 \end{pmatrix} \begin{pmatrix} \vec{u} \\ \vec{v} \end{pmatrix}.$$

Again, by symmetry reasons, I propose that the central benzene ring is centered above an on top site, while the centers of the three outer phenyl units are positioned over hollow sites (Fig. 5.13c). The OP is also different than the two others with respect to the interactions present. Here each terminal alkyne contributes in two ethyne-ethyne bonds only, but does not connect to a benzene ring. Since the hydrogen bridge lengths (3.14 Å) are approximately the same as for the other networks on the surface, it is

thinkable that also the binding energy related to it are similar. Accordingly, the OP seems to be energetically less favorable than the CP due to the missing PARI.

Furthermore, it is interesting to explore the high temperature behavior of the molecules. Upon annealing to higher temperatures the desorption of TEB takes place in the temperature range 270-300 K. On the contrary, after the annealing of samples with a submonolayer coverage of Ext-TEB to 330 K novel molecular units, i.e. dimers, are present. Further annealing to 400 K results in irregular networks. From the room temperature stability of these structures we conclude that covalent bonding is the predominant mechanism responsible for their formation, and we can attribute these effects to the interplay of the reactive terminal alkynes with the catalytic metal substrate[28].

5.3. Conclusion

In this chapter I gave an overview on the self-assembly capabilities of two three-fold symmetric organic species with aromatic backbones and terminal alkyne groups on Ag(111). I found long-range ordered commensurate networks and it was possible to understand the underlying balance between the intermolecular forces and the molecule-substrate interaction in great detail. The superstructures exhibit organizational chirality and are stabilized by a novel, six-membered cyclic synthon, where the ethyne-ethyne interaction is dominant and which is a planarized variant of ethyne-related binding motifs appearing in three dimensional environments. However, under on-surface conditions a substantial part of the stabilization is provided by the interaction between terminal alkyne groups and the phenyl units of neighboring molecules, a characteristic that is absent without substrate. No appreciable cooperative effects were found in the periodic organic sheets. In addition for the larger species a loosely packed phase was found with a three-fold binding motif being more similar to the known 3D synthons. The

results presented in this part of the work demonstrate that terminal alkyne groups can be used for the rational bottom-up construction of on-surface hydrocarbon networks and related nanoarchitectures.

6 Homo-Coupling of Terminal Alkynes on Noble-Metal Surface

6.1. Introduction

The classic route to covalent linking of acetylenes is the oxidative coupling reaction catalysed by copper ions in solution, with the initial key achievements reaching back to distant times [145, 146, 147, 148, 149]. Today, acetylenic coupling is recognized as a versatile ingredient for the rational design of carbon scaffolds and networks [150, 151, 152].

Thus it is a timely issue to explore such reactions at interfaces, and recent studies using a sequential protocol with monolayer self-assembly followed by a cross-linking step provided encouraging results [153]. Pursuing a different vein, there is the prospective research domain dealing with on-surface covalent reactions under ultra-high vacuum (UHV) conditions on clean metal surfaces to realize novel functional nano-architectures and networks [154, 155, 156, 157, 158, 159, 160, 161]. However, many of the employed protocols imply appreciable activation barriers or rely on the enabling character of a set of leaving groups, e.g., Ullmann reactions generating halogens, with the drawback of spurious by-products coexisting with the target structures [155, 157]. Accordingly, processes with milder reaction conditions avoiding at the same time the release of contaminations are needed. The surface confinement can moreover promote unique reaction pathways, nicely exemplified by cyclodehydrogenation processes on Cu(111) for tailored nanographenes [161], or site-specific linear alkane

polymerisation on an Au(110) facet [162]. A recent related report reveals the prominent role of a noble metal substrate in the catalytic course of a C - C Sonogashira coupling reaction elucidating its heterogenic nature [163]. Here I demonstrate through scanning tunnelling microscopy (STM) measurements and density functional theory (DFT) calculations the Ag-mediated terminal alkyne $C_{sp} - H$ bond activation and concomitant homo-coupling in a surface-assisted process. The pertaining C - C covalent bond formation (Fig. 1a) is formally reminiscent of the so-called Glaser-Hay type coupling [145, 148], while presenting a new approach towards silver-acetylide chemistry [164, 165]. The alkyne homo-coupling reaction takes place on the Ag(111) noble metal surface in UHV under soft conditions with volatile H_2 as the only by-product, affording discrete compounds or polymeric networks with a conjugated backbone. The mild thermal activation required, the high yields and the obtained selectivity pose criteria which allow us to rank this process on Ag(111) as a different class compared to the well-known alkyne C - C coupling reactions on transition metal surfaces targeting small aromatic compounds [166]. In view of the demonstrated versatility and promise of acetylenic coupling in solution or bulk environments, and the high prospects associated with on-surface covalent engineering of low-dimensional nano-architectures, the presently demonstrated C - C coupling pathway bears significant potential for the preparation of novel 1D or 2D materials and molecular devices, notably including carbon-pure scaffolds and compounds.

6.2. Results

6.2.1. Surface-assisted covalent dimerization of TEB modules

Compound 1 molecules (1,3,5-triethynyl-benzene, named TEB, (Fig. 6.1b) were initially deposited onto the Ag(111) surface held at 170 K, which results in self-assembled large islands with a long-range periodic structure (Fig. 6.2a). Thus the translational and rotational motion of molecules is

ensured on the poorly reactive Ag surface, which is a prerequisite for ordering and further reaction processes [7]. Within the dense-packed islands individual molecules lie flat on the surface, which is typical for benzene derivatives on noble metals, and appear as triangular protrusions (bright), consistent with the size and symmetry of the intact species.

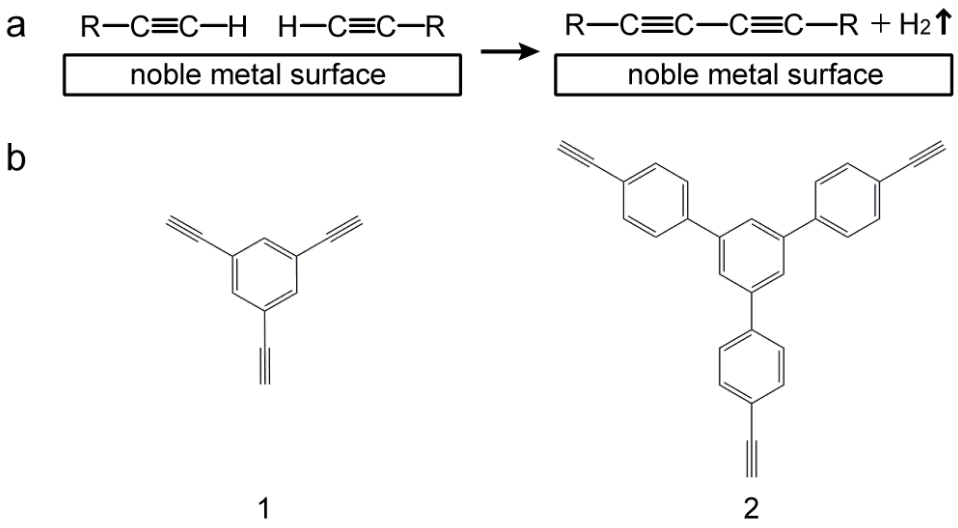

FIGURE 6.1. **Reaction scheme and employed molecules.** (a) surface-assisted homocoupling reaction. (b) terminal alkyne modules: 1,3,5-triethynyl-benzene 1 (TEB); 1,3,5-tris-(4-ethynylphenyl)benzene 2 (Ext-TEB).

Following standard procedures, the first attempt was to thermally trigger a chemical reaction by sample annealing. However, heating the surface with the adsorbed organic layer to room temperature considerably reduces the coverage of TEB molecules without inducing any morphology change in the STM appearance. Thermal annealing up to 330 K essentially restores the pristine surface free of TEB species, i.e. the desorption temperature is lower than that needed to activate a reaction. Thus we exposed the substrate kept at 330 K to a high molecular flux (partial pressure $\approx 10^{-8}$ mbar) in order to induce chemical transformation in the transient adsorption regime. Indeed, this procedure generated distinct novel surface features. The STM image depicted in Fig. 6.2b reveals irregular islands mainly consisting of pairwise arranged triangles connected by a waist (grey, upper right inset), designated as dimers. Only scarcely do the

islands incorporate extended, interconnected arrangements (centre inset). Close inspection also reveals some features (white) ascribed to impurities of unknown nature resulting from the limited quality of the powder used for evaporation. The potential (catalytic) role of these impurities in the resulting topography is excluded in conjunction with experiments presented later.

The very different appearance of the layer is attributed to the prevailing dimers recognized as novel compounds formed on the surface. For a direct comparison of individual TEB-units with the dimer species a sample was prepared as it was already explained, but additionally the exposure to the molecular beam while cooling down was maintained. As a result both monomers and dimers coexist on the surface and can be imaged with exactly the same tip and scanning parameters (Fig. 6.2c). Monomers (highlighted in green) are clearly discernable and their assembly is locally similar to that in the supramolecular layer. By comparison, the appearance of the dimer (highlighted in red) is consistent with the size of two TEB molecules being connected by a 1,3-butadiyne group resulting from the homo-coupling of two terminal alkynes. The results suggest that under appropriate conditions the monomers can be linked by a self-limiting surface-assisted reaction favouring a high yield of dimeric products, whereby the formation of oligomers is inhibited. In fact, a statistical analysis of the sample displayed in Fig. 6.2b shows that approximately three quarters of the originally monomeric compound were successfully dimerised. Due to the increased surface bonding of the dimers it is now possible to induce further changes at higher temperatures. The data in Fig. 6.2d evidence a drastic transformation of the dimer-dominated sample (Fig. 6.2b) upon tempering at 370 K for 10 minutes. Although the observed structures are rather irregular, they definitely must comprise multiple interconnections between the original TEB-constituents, which can hardly be identified in the network arrangement due to the small size of the monomer unit.

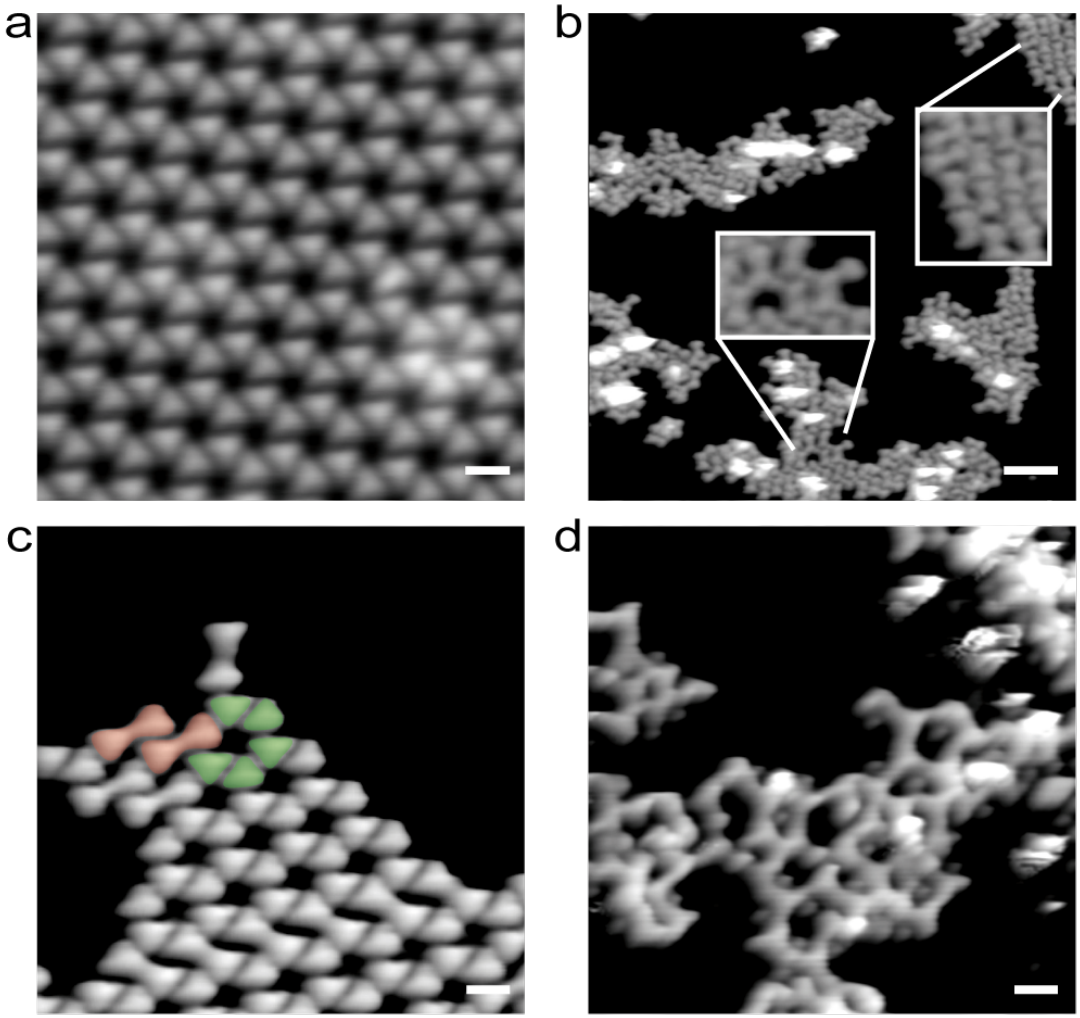

FIGURE 6.2. **STM topographic images of 1,3,5-triethynyl-benzene (TEB) molecules and reaction products on Ag(111).** (a) Dense-packed phase formed by single molecules, deposited at a substrate temperature of 170 K. (b) Overview image with islands of TEB dimers, formed under a high flux on the substrate at a temperature of 330 K. The insets highlight a dimer array (upper right) and oligomeric structures (centre). (c) Area with coexisting single molecules (green) and dimeric compounds (red). (d) Oligomerisation induced by annealing a dimer-dominated sample to 370 K.

6.2.2. Covalent nature of TEB dimer

Next I address the nature of the dimeric TEB-compounds by density functional theory (DFT) simulations. One needs to consider that the dimer formation proceeds under conditions where substrate step fluctuations occur

and silver adatoms exist on the surface. This might interfere in the surface-assisted reaction and potentially afford organometallic Ag bis-acetylide complexes, similar to related scenarios on Cu surfaces [167, 168, 169]. The covalently-bonded dimer was relaxed on the Ag(111) surface and an STM image simulation was carried out with the equilibrium structure (Fig. 6.4a). The calculated image shows a smooth connection between the two TEB moieties, which has an apparent height slightly lower than the two benzene rings. For comparison, the Ag bis-acetylide complex, further referred to as organometallic dimer, would exhibit a characteristic substructure in the connecting waist originating from the metal centre and furthermore its length exceeds that of the covalent dimer. The simulated STM image of a covalently-bonded dimer (Fig. 6.4a) and the experimental data of a dimer (Fig. 6.4b) are rendered with the same colour code. The characteristic outline, the smooth connection via the thinner waist, as well as the slightly brighter benzene rings compared to the waist, all agree well with the simulation. I furthermore analysed the small regular dimer patch depicted in Fig. 6.4c. With the model of the covalent dimer as obtained by the DFT calculations superimposed on the dimer array a very good agreement is found. The unit cell ($a = 14.5$ Å, $b = 10.2$ Å, $\alpha = 88.0$, $\beta = 25.0$) was determined with < 0.3 Å precision (typical error $< 2\%$). Because the extension of covalent vs. organometallic dimers differs by 2.5 Å, the latter cannot be reconciled with the unit cell size. Moreover, STM molecular manipulation experiments were employed to assess the stability of the connection between the two TEB moieties of the dimer (Fig. 6.3). Whereas monomers can be removed from islands of the dense-packed phase without affecting the order of neighbouring molecules (Fig. 6.3a,b), the TEB dimer could only be translated as a rigid unit under similar conditions (Fig. 6.3c,d).

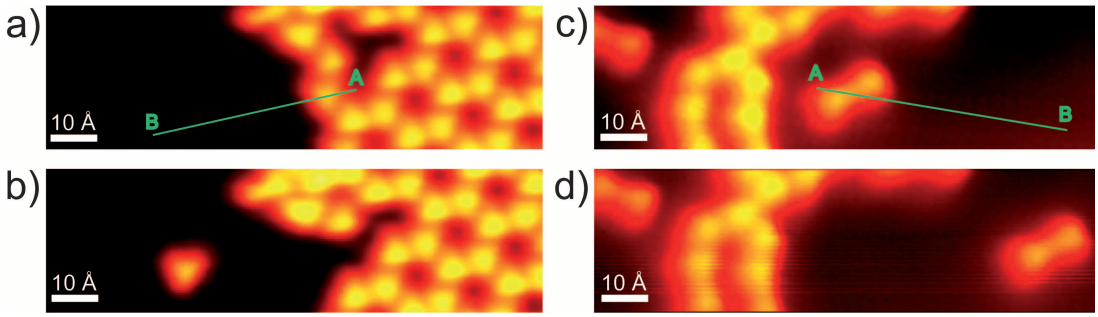

FIGURE 6.3. (a)-(b) STM images before and after a lateral manipulation, moving a single TEB molecule out of the dense-packed phase island. (Constant current manipulation: U = 0.1 V, I = 15 nA). (c)-(d) STM images before and after a lateral manipulation, moving a single TEB dimer. (Constant current manipulation: U = 0.1 V, I = 20 nA). The green lines in (a) and (b) give the starting (A) and ending (B) positions of the manipulation.

The combined insight from STM and DFT results reveals the covalent C - C linkage of ethynyl groups in a surface-assisted homo-coupling reaction. This process is illustrated in Fig. 6.1a. The generated hydrogen atoms are expected to recombinatively desorb as H_2 into the vacuum environment, following the previously established routes [**162**, **170**, **171**]. From the experimental fact that self-assembly of integral molecules readily occurs at low temperatures (Fig. 6.2a), I infer that molecular diffusion and rotation is not a limiting factor for the initial reaction steps.

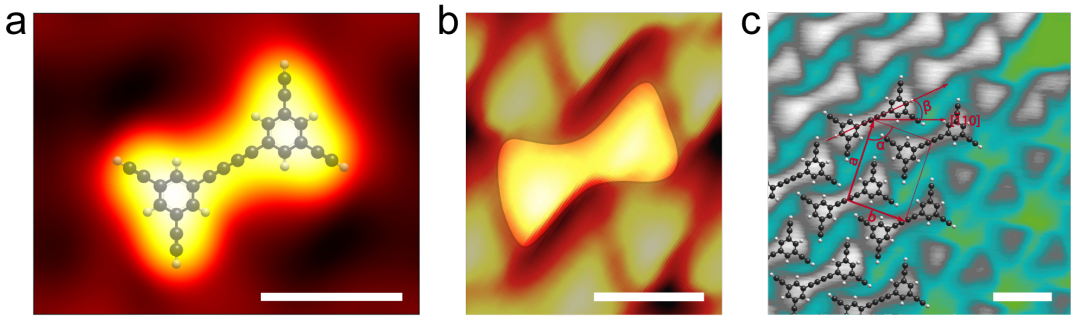

FIGURE 6.4. **DFT simulations and comparison with STM observations.** (a) Simulated STM image of the covalent dimer on a Ag(111) slab ($U = -0.6$ V) with its carbon backbone. (b) High-resolution STM image of a dimer ($U = -0.57$ V, $I = 0.1$ nA). (c) STM image of an ordered dimer patch superimposed with the calculated dimer structure ($U = 0.1$ V, $I = 0.1$ nA).

6.2.3. DFT investigation of reaction pathway

In the survey of possible pathways I started by hypothesizing the sophisticated model, elaborated on the basis of DFT calculations, for the reaction pathway of the Ullmann reaction of halobenzenes [172], where the necessary cleavage of the C - X educt (X being a halogen unit) is expected to proceed readily in an isolated step on the surface, without introducing a major reaction barrier, and thus the analysis can be restricted to the motion and interaction of chemisorbed C_6H_5 units. Applied to the present system, I thus envisioned a precursor formation by the splitting-off of the hydrogen atoms of TEB molecules resulting in formally radical intermediates bound to the surface, followed by diffusion of these intermediates, and a covalent coupling reaction producing the dimer. Transition state calculations were carried out, and I found that in this case the initial $C_{sp}H$ bond cleavage (Fig. 6.5a) implies a reaction barrier of 1.8 eV, being rather high compared to the overall energy barrier of 0.38 eV identified for the Ullmann reaction of C_6H_5 units on Cu(111) that also proceeds at mild temperatures [172]. An alternative, putative mechanism via an adatom-related dehydrogenation (Fig. 6.5b) similar to the one proposed by King et al. [173] seems even more unlikely since it is associated with a reaction barrier of 1.9 eV. Moreover, there is no evidence for atomic steps playing a relevant role in the potential dehydrogenation according to the STM observations.

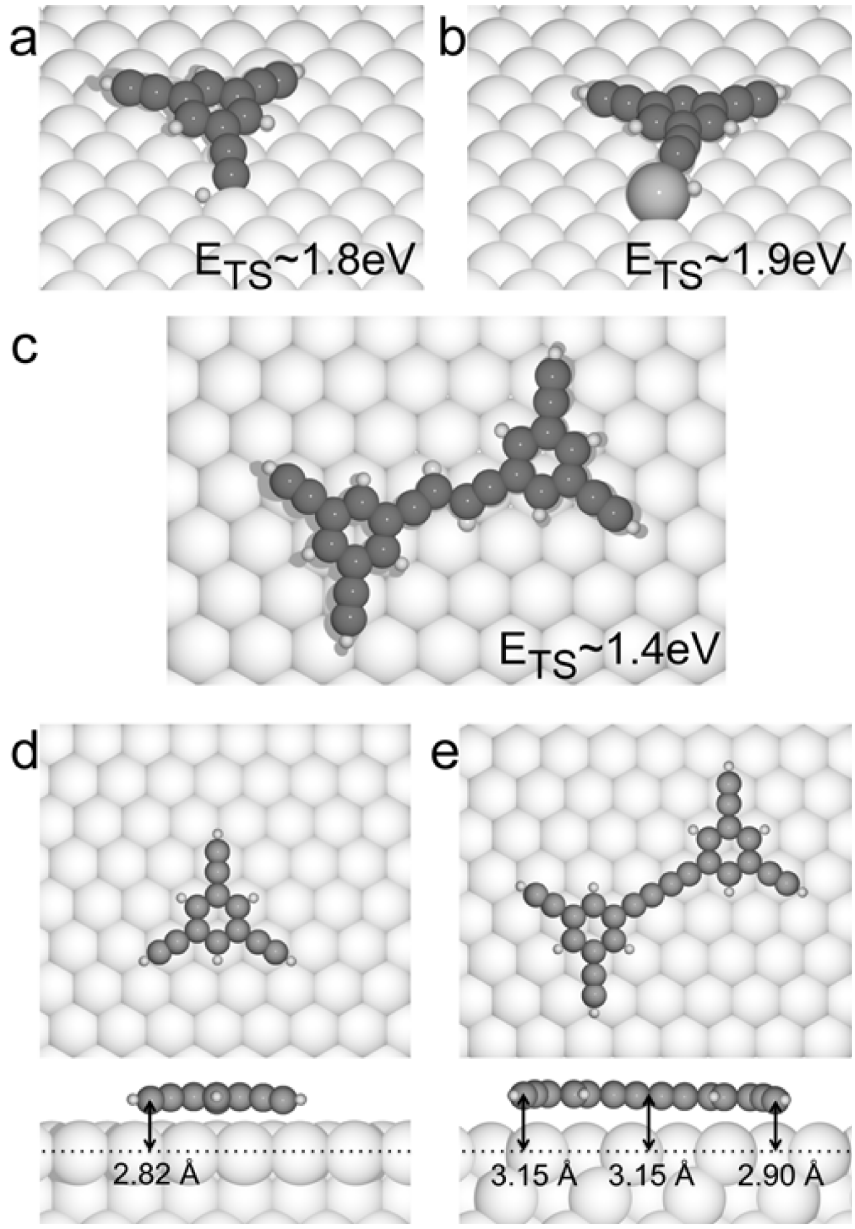

FIGURE 6.5. **DFT calculated possible transition states marking reaction barriers and adsorption geometries of TEB monomer and TEB dimer.** The reaction barriers for (a) surface-catalysed and (b) adatom-catalysed dehydrogenation are remarkably higher than for (c), a direct covalent linking of two tautomerised TEB molecules. The energies of the transition states, ETS, are given with respect to the energy of an isolated molecule on the surface. (d) In the most favourable monomer adsorption configuration the benzene ring is placed on a hollow site and the ethyne groups are centered over top positions. (e) Only the right half of the covalently-bonded dimer can adopt a geometry near to the optimal one displayed in (d). The left half is forced to position the ethyne groups near to less favourable bridge sites. Accordingly, the dimer and most pronounced the left half resides at a larger height than the monomer.

Beyond previously established mechanisms I thus assessed a novel pathway implying a direct covalent bond formation, under the condition that the terminal alkyne group retains initially its integrity. Surface mobility of the constituents is not an issue, because self-assembly of regular TEB arrays readily occurs at $T < 200$ K. Once two terminal alkyne moieties come in touch, a reaction intermediate can be achieved by invoking a connection step producing a tautomerised dimer, followed by the splitting-off of the hydrogen atoms at a later stage. Our calculations suggest an appreciably lower reaction barrier of ≈ 1.4 eV for the direct covalent linking of two TEB units via a nonlinear carbon chain (Fig. 6.5c). The necessary further step-by-step dissociations of the two hydrogen atoms and the reestablishment of the linear butadiyne bridge are almost spontaneous with barriers below ≈ 0.15 eV. Energy barriers were obtained by transition state calculations following the approach described in Ref. [174] using a combination of the climbing image nudged elastic band [175] (CI-NEB) and Dimer [176, 177] methods. In short, CI-NEB was used to find an initial estimate of the transition state. The estimate was then used to generate the input (central image and dimer) in the Dimer method. Structural optimization of the dimer was performed until the forces acting on the atoms in the central images were smaller than $0.04\frac{eV}{\mathring{A}}$. The reaction barrier of ≈ 1.4 eV may be too high to match the experimental fact that dimerization readily takes place at $T \approx 330$ K. However, the employed reaction intermediate geometry was obtained by sticking closely to the covalent dimer coordinates. Transition states yielding smaller barriers are expected to be found by optimizing the tautomer geometry, e.g., with respect to its conformation, the position of the H atoms or its registry with the substrate, which has not yet been done due to the related substantial computational effort. Even without further reduction, the barrier for the tautomerization pathway is already much smaller than the one associated with the covalent coupling of surface-stabilized cyclohexa-m-phenylene radicals on Ag(111), which is rate-limited by the coupling step with a barrier of 1.8 eV [178]. The barrier calculated here appreciably exceeds the 0.4 eV proposed for Ullmann

coupling of phenyl on Cu(111) [172], but this reaction is diffusion limited and thus for larger molecules much higher barriers interfere, as shown in Ref. [178]. Suggested reaction pathway involving a direct merging of two TEB units into the covalent dimer would explain why a higher flux is needed during the deposition to induce the reaction: as this is a second order reaction, a high coverage of molecules is needed in order to compete with the desorption of monomers, which are bonded to the surface by an adsorption energy of ≈ 1.40 eV.

Furthermore, the DFT calculations provide an explanation for the hierarchic character of the coupling reaction. The comparison of the monomer adsorption height (on average 2.93 Å above the Ag surface layer) with the dimer reveals a lifting of the latter by 0.19 Å. The most stable bonding geometries of the monomer and dimer are compared in Fig. 6.5d and e where the adsorption heights of the alkyne groups are indicated. The monomer adsorbs symmetrically with the CH carbons of the alkyne group at a height of 2.82 Å. The dimer has no high-symmetry adsorption configuration with all alkyne groups adsorbed equivalent on the surface, but half the dimer adsorbs close to the geometry of the monomer, with the alkyne groups at a height of 2.90 Å. The other half of the molecule is adsorbed in a less favourable configuration explaining why this side of the molecule resides considerably further away from the surface. Supporting experimental evidence is provided by a comparison of the apparent height of monomer and dimer units in the same STM image (Fig. 6.6). TEB monomers exhibit a systematically lower value (0.87 Å) than the dimers (0.98 Å). Even though the apparent height values depend on the bias and cannot be compared to the geometric height directly, the bias independent tendency that dimers are systematically imaged higher than monomers is in agreement with theory. In addition, the slight asymmetric shape of the dimers is also consistent with the calculations. The increased adsorption height of the dimer compared to the monomer can be assigned to the mismatch between the dimer and Ag substrate.

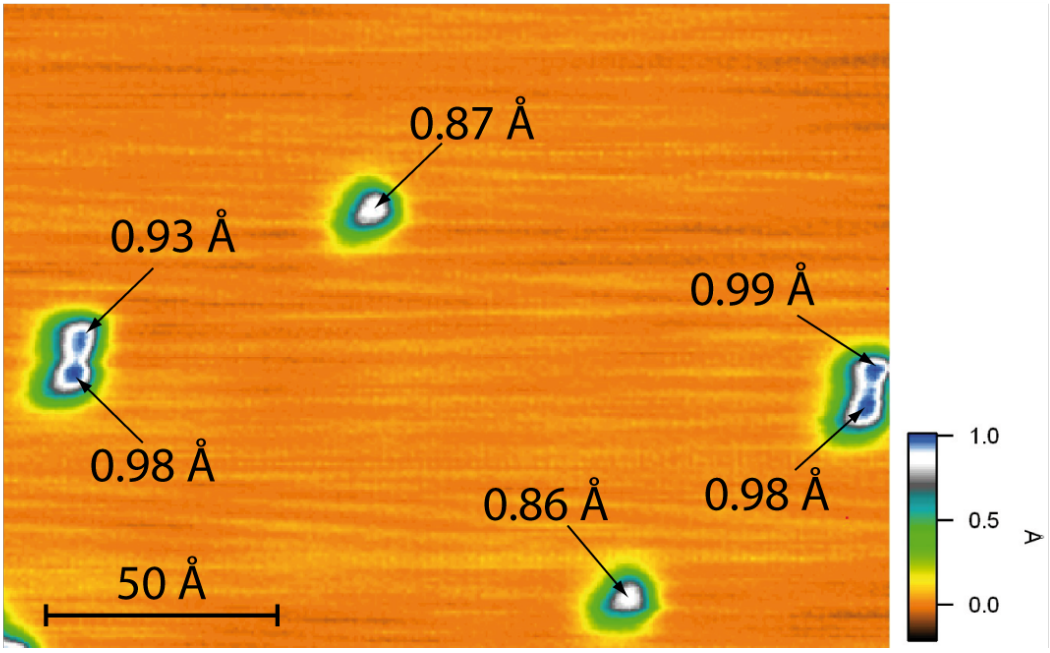

FIGURE 6.6. **Apparent height of isolated TEB monomer and dimer on the Ag(111) surface.** Constant-current STM image (U = -1 V, I = 0.1 nA). The maximum apparent height of the TEB monomers and dimers indicated by black arrows is shown. The averaged apparent height of the dimers is approximately 0.1 Åhigher than that of the monomers. The apparent height difference is also clearly visible with the colour scale employed.

One notes that the average adsorption height of the four favourable adsorption geometries for the monomer (cf. Fig. 5.6 from the Chapter 5) differ by 0.19 Å proving that small deviations of the most favourable adsorption geometry induce quite significant height changes. In addition, the covalently coupled alkynes may also have a negative effect on the interaction with the surface compared to the original terminal group. In any case, due to the lifting of the dimer compared to the monomer the catalytic effect of the surface is reduced after the first homo-coupling step, and any subsequent oligomerisation implies increased energy barriers. This intriguing result indicates that the covalent coupling of the surface-confined terminal alkynes is sensitively influenced by the subtle details of the bonding geometry. It is suggested that this feature can be further explored to achieve site-selective linking of multitopic polyalkyne modules regulated by appropriate spacer groups at the respective terminal ethynyl groups.

Such properties are sought for heterogeneous catalytic reactions or covalent engineering of hierarchic surface nano-architectures [179]. A comprehensive modelling of all possible pathways within the DFT framework is clearly beyond the scope of the present study, however our present theoretical understanding strongly supports a new mechanism for the presented homo-coupling reaction on the Ag(111) surface.

6.2.4. Generality of the on-surface homo-coupling

To demonstrate the generality and further explore the noble metal surface-assisted alkyne homo-coupling reaction molecule 2 (1,3,5-tris-(4-ethynylphenyl)-benzene was synthesized; Ext-TEB; see Fig. 6.1b). Depositing Ext-TEB molecules at low temperature (152 K) leads to the assembly of highly regular supramolecular domains (Fig. 6.7a) with flat-lying species and a packing scheme similar to that of TEB molecules. Following annealing of the covered surface to 300 K, again the characteristic dimers evolve, as shown in Fig. 6.7b, coexisting with unreacted precursor Ext-TEB species. Accordingly, the surface-assisted reaction is not outstripped by monomer desorption, which effect is ascribed to the stronger surface interaction. The imaging characteristics of the Ext-TEB dimers, in particular the resolution of the connecting waist and its overall length can be explained on the same grounds as those of their TEB analogues. Hence we conclude that the Ag(111) surface similarly promotes the Ext-TEB homo-coupling reaction, which process also obeys the hierarchic principle identified for the TEB species.

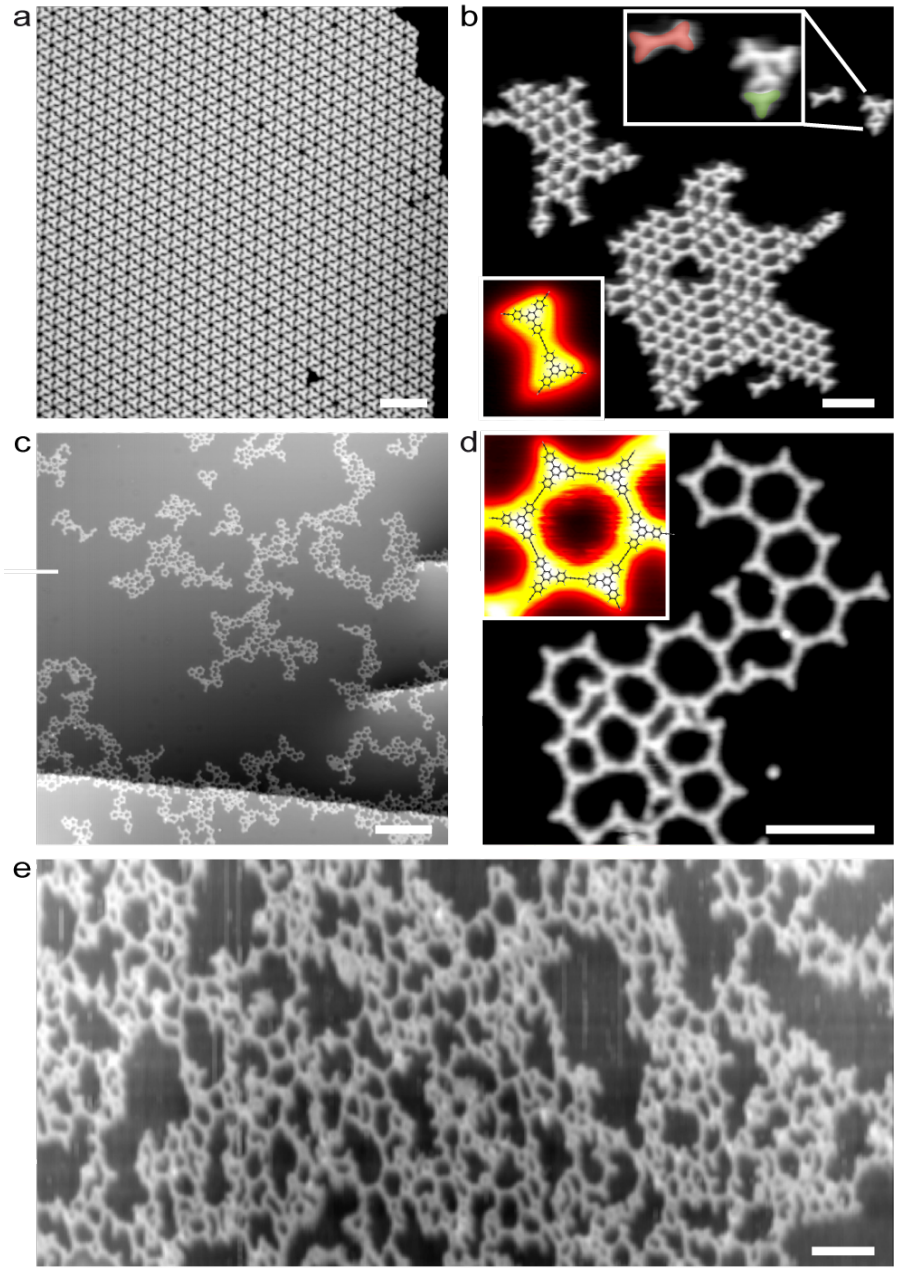

FIGURE 6.7. **STM topographic images of Ext-TEB molecules and reaction products on Ag(111).** (a) Dense-packed phase formed by unreacted Ext-TEB molecules, deposited at a substrate temperature of 152 K. (b) Covalently bonded Ext-TEB dimers obtained by annealing at 300 K. The down-left inset shows a high-resolution image of a dimer superimposed with a HYPERCHEM calculated model. The upper inset magnifies an area with dimers (red) and monomers (green). (c) Large scale image of covalent network patches, through annealing the sample to 400 K. (d) In the magnified area an open reticular structure from the merged ethynyl moieties prevails. The inset shows a single honeycomb nanopore superimposed with a HYPERCHEM calculated model. (e) STM overview image recorded at room-temperature of a robust polymeric network structure obtained by irregular crosslinking at 520 K demonstrates the robustness of the structure at conditions relevant for later applications.

With the extended organic species I managed to elaborate an even clearer picture of the polymerization reaction. A mild annealing treatment (400 K) leads to the formation of irregular, open-porous networks (Fig. 6.7c), i.e. we again encounter a hierarchic reaction pathway. A closer inspection of the zoom-in (cf. Fig. 6.7d) demonstrates the high level of purity achievable with our approach. Furthermore, it reveals that the covalently-bonded architecture contains a series of features reflecting the pairwise connection of the terminal ethynyl groups and a certain degree of molecular flexibility. The six-membered oligomeric cyclic units represent the ideal product of a convergent homo-coupling reaction with straight C - C connections between the Ext-TEB modules. The inset shows a magnified image of the associated honeycomb unit, and a corresponding HYPERCHEM model that nicely fits the STM data. By contrast, the additional five- and seven-fold cyclic structures imply distortions of the molecular modules [168, 169, 180]. In addition, some features are visible where three molecular terminations join together which can be of different origin including covalent connections differing from the intended butadiyne bridges as further discussed in the capture of Fig. 6.8.

Next, I demonstrate the formation of extended 2D polymeric networks using the surface-assisted coupling protocol. The STM image in Fig. 6.7e reveals that a coherently reticulated layer structure decorating the entire silver substrate can be readily achieved with the thermal treatment of high Ext-TEB surface concentrations. Importantly, this reaction product is robust and its stable character becomes obvious in STM data recorded at room-temperature. The layer formation reflects an irregular crosslinking process. In this sample the deviations from the ideal linear butadiyne bridges are more frequent than in the previous sample (Fig. 6.7d). We attribute this to the fact that before the thermal treatment a higher molecular coverage was present and the maximum annealing temperature was 520 K. The combination of both probably gives rise to more types of covalent connections differing from the intended one. Because the lateral C - C linkages between the Ext-TEB modules are stronger than the surface bonding of

individual units, the layer represents a covalent nanomembrane that can be potentially used in further processing steps and applications, similar to related 2D sheets [181, 182, 183, 184].

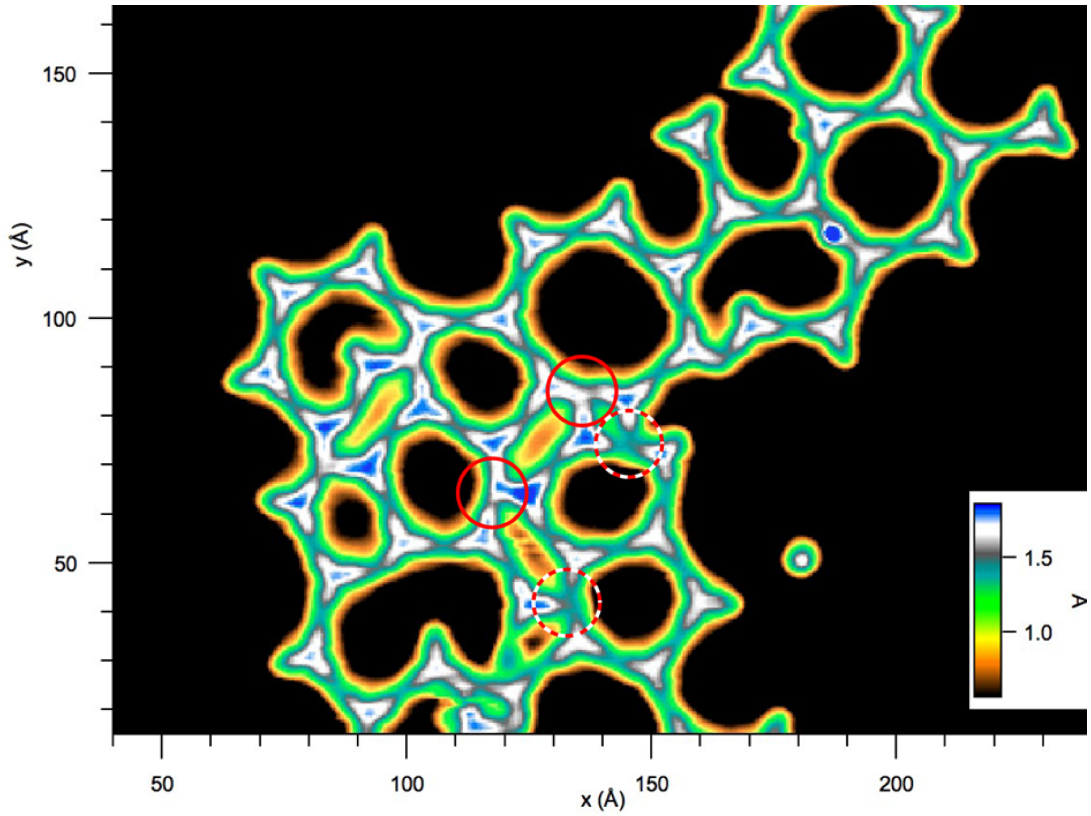

FIGURE 6.8. **STM topographic images of Ext-TEB after annealing to 400 K.** Apart from the intended butadiyne covalent bridges irregular features are visible where three molecular terminations join together. In some cases (red circles) these connections appear brighter than in other cases (red dashed circles). The origin of these structural features remains unclear. Probably one of these cases is related to covalent connections differing from the intended butadiyne bridges, while the other could be explained by terminal groups exhibiting unusually short distances due to being forced by the covalent backbone of surrounding molecules.

6.2.5. Complementary X-ray photoelectron spectroscopy evidence

Finally, the claimed covalent bond formation is substantiated by complementary X-ray photoelectron spectroscopy (XPS) measurements. I investigated a sample prepared under comparable conditions as the one showing the reticulated Ext-TEB network, i.e. evaporation of Ext-TEB onto the Ag(111) surface at 315 K followed by mild annealing to 400 K. In the C_{1s} region (Fig. 6.9a) only a single discernable peak is present at a binding energy of 284.9 eV resulting from a superposition of several carbon species with binding energies differing by less than the energy resolution. Due to the overlapping of the signals of the chemically slightly different carbon species, the experimental profile was fitted with only two general Voigt peaks that do not represent a distinct carbon species each. Since a typical binding energy for methylacetylide on Ag(111) is 283.7 eV [185], the absence of such a low-energy shoulder already indicates the absence of organometallic bonding in our sample.

Further support for the covalent character is provided by a DFT-based simulation of XPS line shapes (Fig. 6.9b) of a covalent TEB dimer (Fig. 6.9c) and an organometallic dimer (Fig. 6.9d). In this simulation the smaller TEB species was used instead of the larger Ext-TEB due to computation time limitations. The geometries of the respective adsorbates were optimized on the Ag(111) slab and then the C_{1s} core-level shifts were calculated for each carbon atom with reference to an arbitrarily chosen atom (cf. Fig. 6.9c, d and Fig. 6.10). Then for each carbon atom a Voigt peak with a shape expected for the experimental resolution of ≈ 0.6 eV was generated and the peaks were superposed taking into account the relative energy shifts. The resulting simulated signal was placed on the same energy axis as the experimental spectrum in order to facilitate comparison (Fig. 6.9b). Consistent with the literature our simulation of the organometallic dimer (red dashed line) shows a low binding energy shoulder originating from the ethynyl groups interacting with the Ag atom. In the case of an Ext-TEB network where most of the ethynyl groups are coordinated to a

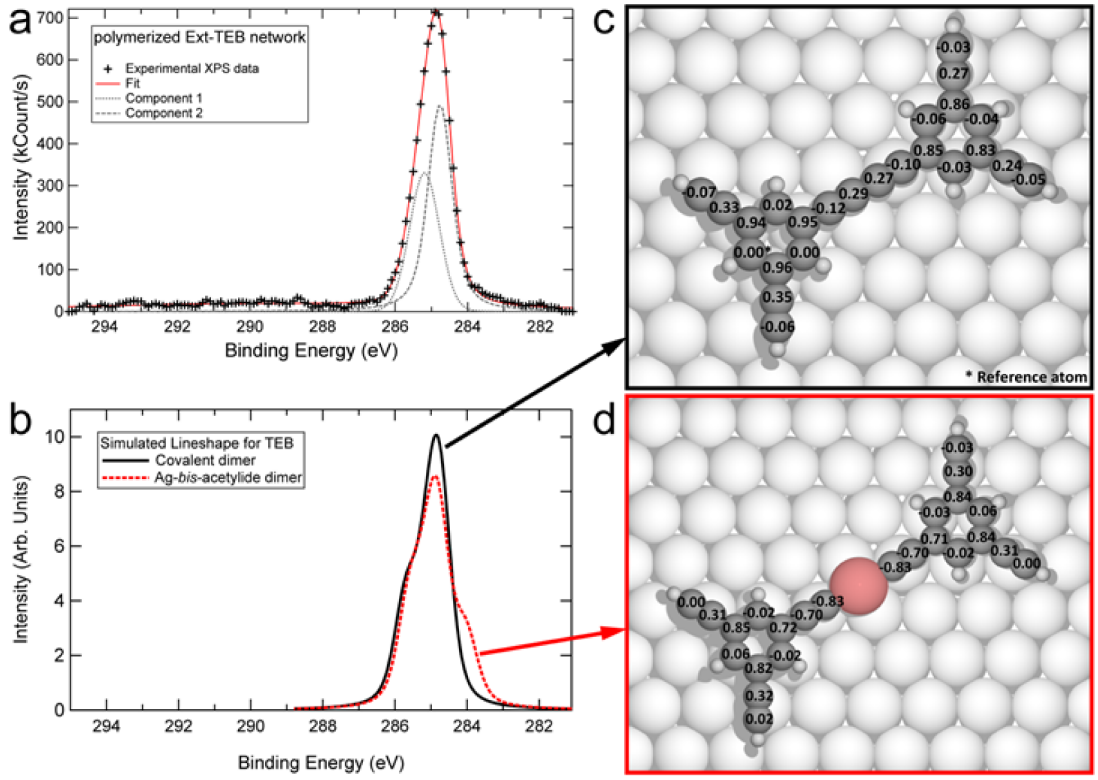

FIGURE 6.9. XPS data of polymerised Ext-TEB network and DFT-based simulated line shapes calculated from covalent and organometallic dimers. (a) Experimental XPS data of the C_{1s} region of a sample with a submonolayer coverage of Ext-TEB after annealing to 400 K. The experimental spectrum (crosses) show a single peak centred at 284.9 eV. (b) DFT-based simulation of the XPS line shape of the covalent (black solid line) and the organometallic (red dashed line) TEB dimer expected for an experimental resolution of $\approx$ 0.6 eV. c and d, Top view of the DFT-optimized adsorption geometry of a covalent and an organometallic TEB dimer respectively. The C_{1s} core level shifts relative to the reference atom are superimposed on each carbon atom. The Ag atom incorporated into the organometallic dimer is highlighted in red in (d).

silver atom, approximately the same relative intensity of this shoulder is expected. Thus, the low energy component should be clearly discernible with the experimental resolution. However, no such component is visible in the experimental data. Therefore the XPS analysis strongly opposes to a potential organometallic binding mechanism behind the formation of the 2D polymeric network in agreement with our combined STM/DFT analysis.

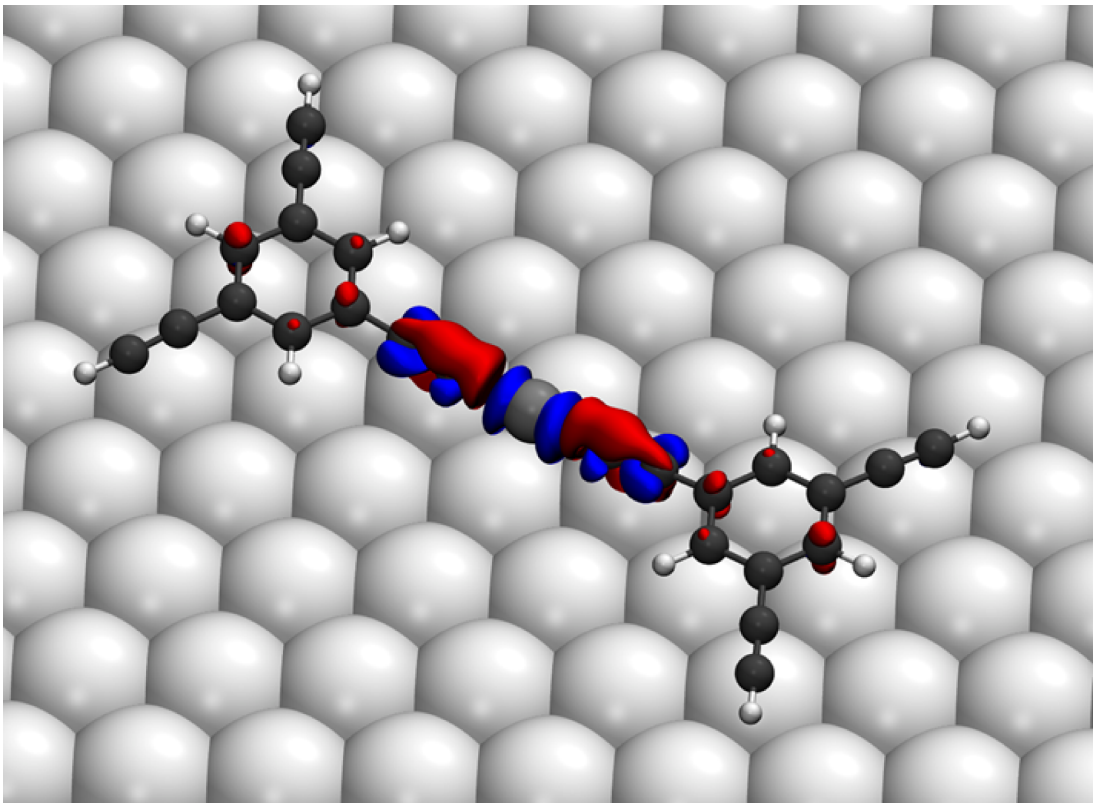

FIGURE 6.10. Charge difference plot of the Ag bis-acetylide complex. Electron charge density difference in the organometallic dimer calculated as the electron density difference between the full system and three reference systems consisting of each of the two molecules and the silver surface (with Ag adatom). The red contours are electron accumulation and the blue contours electron depletion and the value of the contours is 0.02e. The Ag adatom donates electrons to the former ethyne groups, which at the same time back-donates into the organometallic dimer.

Simulated core-level shifts were obtained by comparing total energy differences between core-ionized and ground state systems. The total energies of core-ionized systems were computed by using a core-ionized PAW potential for the core-ionized atom as described by Köhler and Kresse [186]. Hence, a separate calculation was carried out for every atom for which the core-level shift was computed. In this way, not only the local electrostatic potential of the atoms, but also screening of the core-hole in the final state is taken into account when simulating the core-level shifts. Similar calculations yielded reasonable results and proved to be helpful for the understanding of bonding properties in surface anchoring of organic species [187] and on-surface molecular architectures [188].

6.3. Discussion

In solution chemistry, the formation of π-alkyne-silver complexes is an initial step on the way to acetylides, i.e. between silver cations and terminal C - H bond a nonlinear two-electron, three-centre bond is formed (for a thorough discussion cf. Refs. [164, 165]). With the surface confinement the planar adsorption of the presently investigated organic species entails a natural proximity between the Ag surface atoms and the ethynyl group. This geometry profoundly influences the chemical nature of the terminal alkyne. From the mild temperatures at which the homo-coupling takes place it can be concluded that the very presence of the Ag(111) substrate indeed supplies a catalytic template. The hierarchic steps in which the reaction proceeds demonstrate how sensitive the alkyne C - H activation and reactivity responds to subtle changes of the local environment. Moreover, with the reaction pathway being established via a tautomerised intermediate, there is no need to a priori invoke an organometallic reaction intermediate, i.e. there is a formal similarity with the envisioned mechanism in silver acetylide formation in the presence of a base [165], being at variance with related processes mediated by transient attachment of copper ions at the ethynyl group [173]. It is also interesting to note that it was impossible to induce covalent bonding of acetylene molecules on an oxide surface by the presence of single silver atoms [189].

To conclusion, I introduced a novel heterogeneous catalytic synthesis protocol for the surface-confined coupling of terminal alkyne species at a smooth noble metal substrate. The systematic STM measurements and DFT calculations demonstrate covalent C - C bonding and 2D polymerisation through homo-coupling reactions in a surface-assisted synthesis proceeding in vacuum under mild conditions without generation of spurious by-products. With multifunctional species (e.g., the presently employed tritopic compounds) product formation is affected and tunable by hierarchic reaction pathways, reflecting the modified surface interaction of reaction intermediates. It is suggested that terminal alkyne building blocks can

be in general covalently linked on suitable noble metal surfaces to create novel molecular compounds, low-dimensional superstructures or coherently reticulated polymeric layers. This provides a new synthesis route towards conjugated molecular nanosystems and networks, providing potential for the fabrication of regular 1D scaffolds like carbyne [190, 191], 2D-polymers like graphyne or graphdiyne [150, 192], and similar hydrocarbon membranes. I furthermore envision the use of nanostructured interfaces and noble metal nanoparticles as catalytic materials and reaction templates under vacuum or other conditions.

6.3.1. Sample preparation

The sample was prepared as it was already explained in Chapter 2. For TEB molecules a non-purified powder was used, introducing a small concentration of contaminations on the surface. The related impurities do not interfere in the surface processes, as evidenced by the self-assembly of the pure species (cf. Fig. 6.2a). In UHV the room temperature vapor pressure of TEB is finite. As a result the molecular flux obtained at a specific T_{OMBE} reduces with time after filling of the crucible. For the sample shown in Fig. 6.2b T_{OMBE} was room temperature. The higher flux used for subsequent experiments was achieved by a new refill of TEB molecules into the crucible, i.e. it did not imply increased evaporation temperatures. In order to avoid polymerization for TEB molecules in the crucible, the sublimation temperature was strictly kept below 370 K for all preparations. Sublimating TEB molecules (T_{OMBE} ¡ 370 K) onto the cold Ag(111) substrate held at 170 K, no signature of covalent reaction was found. After the preparation, the sample was cooled down and transferred into our home-made Besocke-type scanning tunnelling microscope (STM) [51], where data were recorded with a chemically etched tungsten tip at 5.5 K (unless mentioned otherwise). The bias for tunneling current is applied to the sample. If not stated otherwise typical tunneling condition were $U = -1$ V and $I = 0.1$ nA.

7 Quantum Confinement in 2D Nanoporous Honeycomb Networks at Close-Packed Metal Surfaces

In this chapter I present a systematic theoretical investigation of electron confinement phenomena in two-dimensional (2D) nanoporous honeycomb networks, motivated by a joint theoretical and experimental study of the hexagonal networks consisting of dicarbonitrile-sexiphenyl molecules coordinated by cobalt adatoms on Ag(111) surface [193]. I study the electronic structure within a pseudopotential landscape employing the boundary elements method (BEM) and electron plane waves (EPW) expansion. By systematically varying the scattering parameters I demonstrate the origin of different effects influencing the confined states and the relation between the scattering potential landscape and the electronic band structure. Moreover, I present a unified theoretical explanation of the data obtained with the complementary methods, scanning tunneling spectroscopy (STS) and ARPES. Parts of the chapter were published in the reference [194].

7.1. Introduction

The electronic properties of metal surfaces can be strongly affected by the presence of surface states which exist in the projected bulk band gap and are localized at the solid-vacuum interface [34] Notably, the so-called Shockley states provide a quasi-two-dimensional nearly-free electrons gas

(2DEG) with a well-defined effective mass and energy dispersion relation [33, 195] Historically, they were first observed on Cu(111) by means of angle-resolved photoemission spectroscopy (ARPES) [30] for which the resolution increased drastically over the time [196, 197]. With the invention of scanning tunneling microscopy/spectroscopy it became possible not only to investigate surface states both in the occupied and unoccupied regime, but also their local characteristics [31, 198, 199]. Moreover, the careful positioning of individual adatoms with tip manipulation [70] allowed for the deliberate nanoscale tuning of the electronic properties of a close-packed metal surface by confining the 2DEG. The geometry of the man-made quantum corrals defined the resulting standing wave patterns, including their lateral electron density distribution, as well as the energetic position of the related resonances. Substantial effort has been dedicated in the last 20 years to the tuning of electron wave function properties by scattering geometries of arbitrary shape [200, 201, 202, 203, 204] leading to such intriguing effects as quantum mirage [205, 206, 207], above-barrier resonances [208], spin coupling [209] etc. In parallel, vicinal surfaces also turned out to be a convenient terrain for observing standing-wave patterns and superlattice effects, because they exhibit a very easy recordable surface state and the surface electrons scatter strongly on the step egdes [210, 211].

A major disadvantage of the manipulation-based approach is that mesoscopic tuning of material properties can not be achieved. This limitation can be overcome with recently developed two-dimensional supramolecular self-assembly protocols [7, 72], because adsorbed molecules can take over the role of the scatterers equally well as adatoms [212]. It has been shown that this parallel bottom-up approach presents versatile strategy for a surfacewide control over electronic properties by fabrication of regular arrays of confining structures [106, 95, 193, 213]. Moreover, this strategy is even suitable to steer the organization of additional adsorbed species [106, 214, 215]. However, a thorough understanding of the details of the

imposed characteristics as well as the relation between network geometry and resulting interfacial band structure is still missing.

7.2. Results and Discussion

For the detailed study of the electron confinement in supramolecular networks the starting point was the model of a particle in a box. In this simple model it is assumed that the electron is characterized by an effective mass m^* [33] and confined to a 2D area by infinitely high potential barriers. Despite of its simplicity it enables quick and efficient analysis of the phenomena connected with confining effects. Since we later want to analyze networks with hexagonal symmetry, we define the confining area to be a regular hexagon. The geometry does not allow separation of radial and azimuthal variables, therefore the model does not permit an analytical solution and a numerical approach is required. In our case the Schrödinger equation is solved with help of BEM, described in the computational methods section.

The first investigated system is a hexagonal cavity surrounded by a barrier [Fig. 7.1(a)]. The diameter $D = 57.78$ Å and the barrier width $d = 2.45$ Å were chosen in accordance with our earlier experiment [63]. The height of the potential barrier V, i.e., the difference between the potential inside the hexagon and the potential inside the barrier was chosen to be 10 eV as an approximation of infinitely high walls. The LDOS spectra [Fig. 7.1(b)] are calculated at representative points defined in [Fig. 7.1(a)]. The density curves consist of several very narrow and high-intensity peaks. In the cavity center two peaks (1 and 4) are observed at -5 meV and 245 meV. At the point halfway 1, i.e., at the half of the distance between the center and the middle of the barrier, four eigenstates (1, 2, 3, 6) exhibit non-zero intensity. Finally, at the halfway 2 position, i.e., at half the distance between center and a corner of the hexagon, all eigenstates except the one at 370 meV contribute to the spectrum. We also calculated the spatial

distribution of the electron density [Fig. 7.1(c)] for the eigenenergies at which the peaks appeared. For the first eigenenergy (-5 meV) the landscape is dome-like with the strongest LDOS ρ at the center and decreasing with the distance from it. The eigenstates 2 and 3 exhibit both a donut-like distribution. For the one lower in energy ρ is almost the same at halfway 1 and 2, while for the latter one ($E = 205$ meV) protrusions are formed at halfway 1. The maximal density ρ_{max} of the fourth eigenstate is localized predominantly at the center, which is reflected in a bright yellow spot, but a weak surrounding rim is visible in addition. The last two eigenstates exhibit density maxima on the respective halfways, why the corresponding landscapes consist of sixfold patterns rotated mutually by 30 degrees. Each two-dimensional landscape is normalized to its ρ_{max} and the same color scales were used. It should be pointed out that the intensities given in the caption of [Fig. 7.1(c)] are different from the values read out from the LDOS spectra. This is due to the sharpness of the peaks and the fact that energies of the peaks' maximum and the input values for 2D plots are only approximately the same. Our findings for this system nicely agree with an earlier report of Li *et al.*[33], which demonstrates the validity of the two numerical approaches.

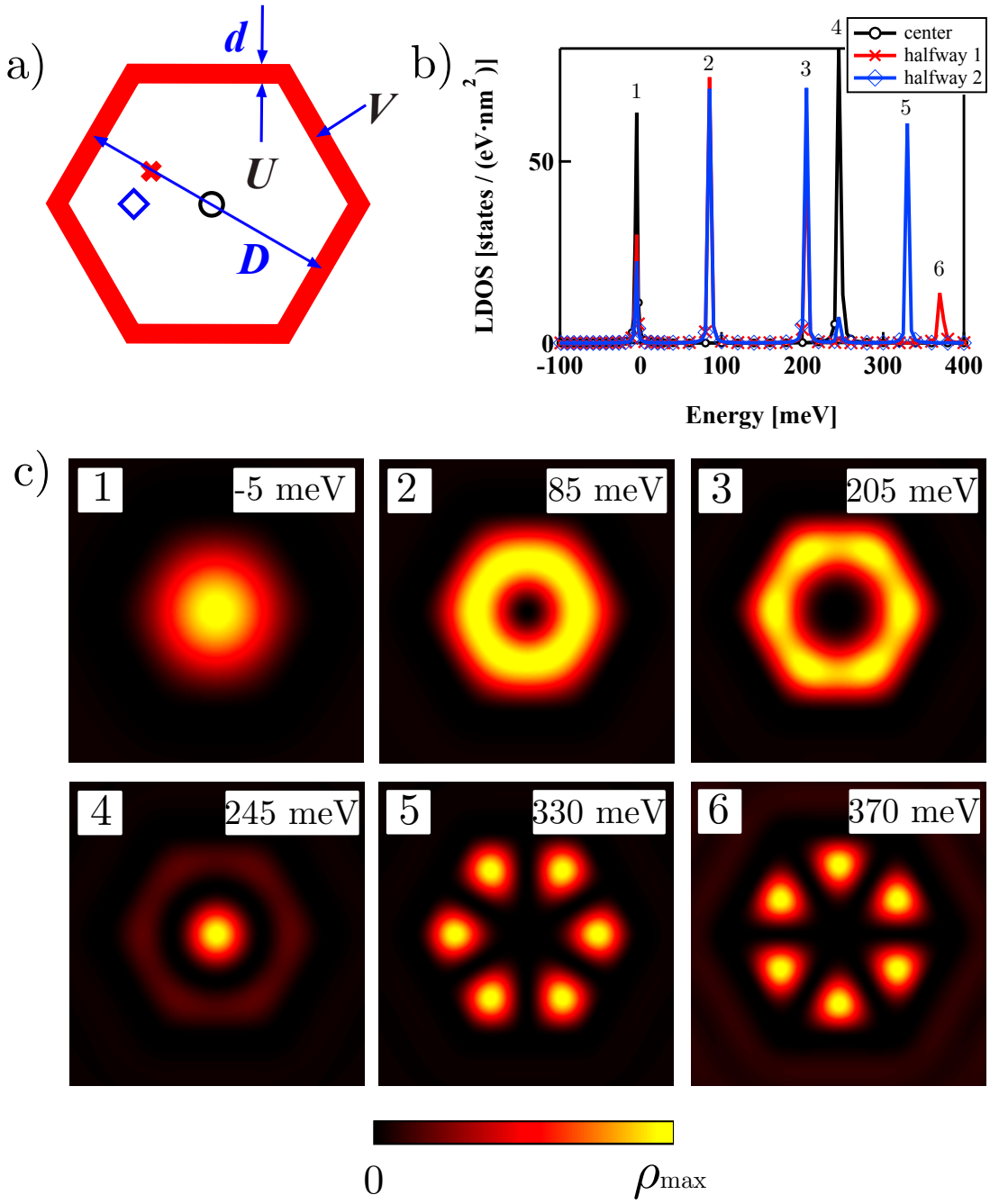

FIGURE 7.1. (a) An isolated hexagonal potential well. Diameter of the pore is $D = 57.58$ Å, barrier width $d = 2.5$ Å. Height of the barrier is $V = 10$ eV. The points on which the LDOS was calculated are labeled with colored markers (black circle, red cross and blue diamond). (b) LDOS on the representative points. (c) Spatial distribution of the DOS for the eigenenergies as indicated. ρ_{max} values expressed in $\frac{\text{states}}{\text{eV}\cdot\text{nm}^2}$ are: 63.6, 63.5, 78.3, 72.4, 80.8 and 25.4.

Next, we analyze the electronic properties of metal-organic networks with finite potentials. For understanding the influence of the different constituents we rely on a series of systems with comparable parameters [Fig. 7.2]. We start again with the case of an isolated island [Fig. 7.2(a)], where D remained the same as before, but d was set to a more generic value of $d = 5$ Å, allowing more pronounced influence of the corners for the assessment discussed below. The barrier potential V was changed to 500 meV providing tunneling of the electrons throughout the barrier, thus simulating a situation generated by physisorbed conjugated π-systems [95]. Concerning the average lifetime of the states Γ, we did not use the lifetime broadening applied recently [63] (25 meV), but instead we have chosen $\Gamma = 2$ meV, to obtain sharper features, making the analysis easier.

For the isolated island the spectrum of the center [Fig. 7.2(a), right panel, black circles] shows two peaks with maxima at -15 meV and 200 meV, where the width of the first is sharper than that of the second one. The LDOS of the halfway spectrum (red crosses) has three clear maxima (-15 meV, 61 meV and 163 meV) and a broad structure above 300 meV. On the contrary, no clear peaks are observed in the spectra computed above the barrier (blue diamonds) and corners (green squares).

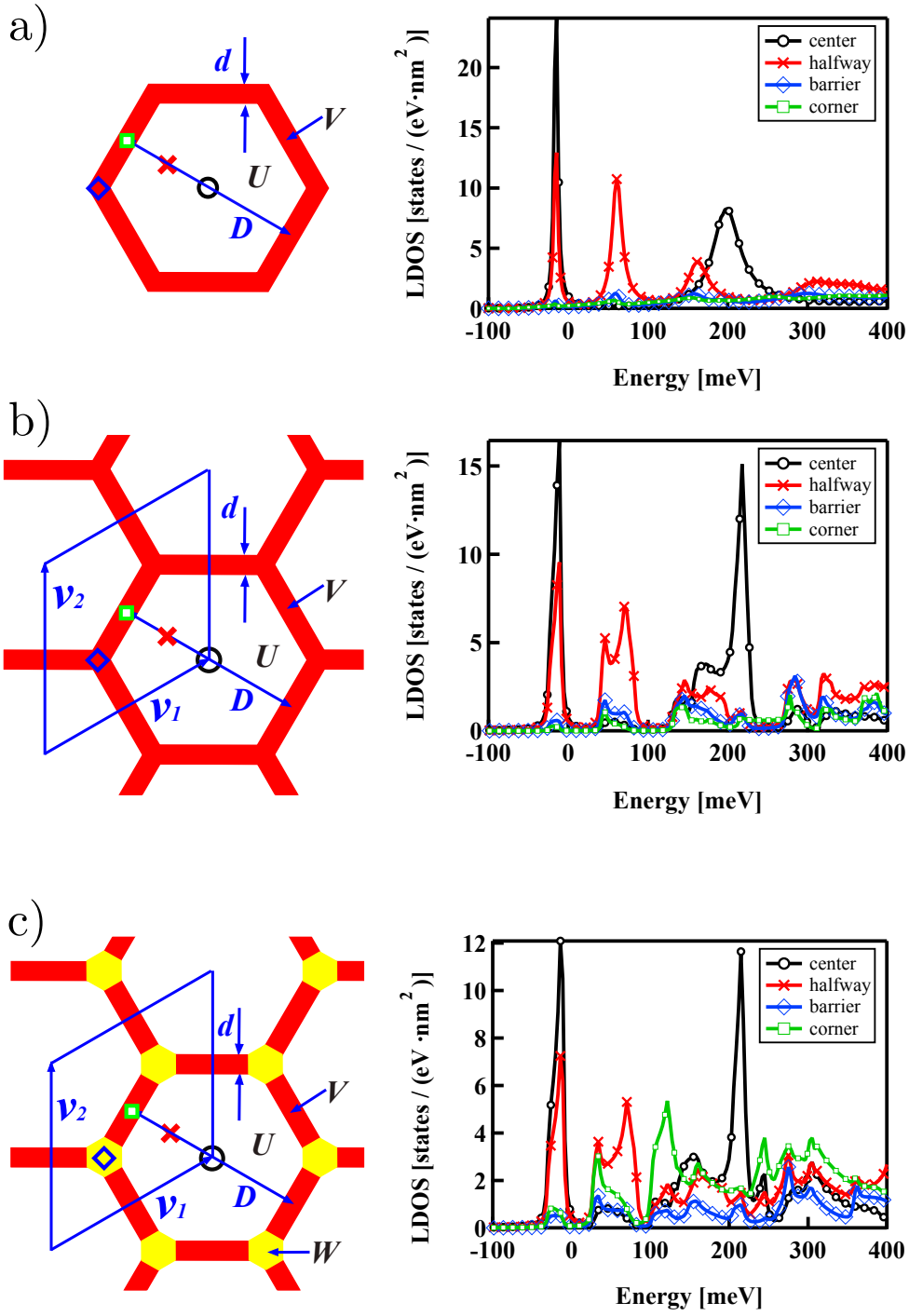

FIGURE 7.2. Series of comparable systems. The left column sketches the geometrical representation of (a) an isolated island, (b) the elementary cell of the UV and (c) the UVW system spanning a periodic lattice. The diameter of the pore is $D = 57.58$ Å, the barrier width $d = 5$ Å. Unit vectors are denoted with $\vec{v}_1$ and $\vec{v}_2$. The barrier potentials amount to $V = 500$ meV and $W = -100$ meV (UVW system only). The points at which the LDOS was calculated are referred to with colored symbols (black, red, green and blue). The right column displays the LDOS calculated at the points defined in the geometrical representation. - (color online)

It is noteworthy that the central peak at 200 meV is rather wide despite of very low energy broadening ($\Gamma = 2$ meV), which indicates a high transmission coefficient at this energy. We confirm this assertion by calculating the reflexion (R) and transmission (T) coefficients of the analytically solvable case of a one-dimensional barrier with a geometry as defined in Fig. 7.3(a). They are expressed as $T(E) = \frac{|B|^2}{|A|^2}$ and $R(E) = 1 - T(E)$, where A is the complex amplitude of the incoming wave and B that of the transmitted wave. Using the textbook formula [216]

$$R(E) = 1 - \frac{1}{1 + \frac{V^2}{4E(V-E)} \sinh^2\left(\sqrt{\frac{2m^*(V-E)a^2}{\hbar^2}}\right)}$$

we obtained the curves shown in Fig. 7.3(b). Particularly, for the incident wave with an energy of 200 meV the computed values are $R = 0.15$ and $T = 0.85$. We also related R with the linewidths by using the formula

$$\Gamma_l = -\frac{\hbar^2}{m^* S}\sqrt{\frac{2m^*(E - E_0)}{\hbar^2}} \ln\sqrt{R},$$

derived in earlier work [217] by Crampin *et al.* and this dependence is illustrated in Fig. 7.3(c). The formula was originally obtained for circular resonators of the radius S, which we use here as an approximation of the hexagonal scattering boundary by defining $S = D/2$. Comparison of $\Gamma_l(R)$ [Fig. 7.3(c), solid line] with the values obtained by fitting the LDOS curves [Fig. 7.2(a), circles and crosses] with a set of Lorentzians (each peak has been assigned one Lorentz peak) yields an agreement to within 4 meV. The agreement corroborates the consistent treatment of inelastic scattering effects in the analytical approach of Crampin *et al.* [217] and the numerical BEM.

The formula for Γ_l given here is based on the assumption of the inelastic scattering and the s-wave approximation, which was also used previously [200], where the array of adatoms building up the corral are considered as totally absorbing walls with a δ-function potential. The pertaining approach gave a qualitatively good description of the linewidths and scattering processes, but could not correctly describe widths for higher energies.

This was achieved by using an alternative picture; namely elastic scattering only on rectangular, finite-height potential barriers is taken into account, [218] which excludes a significant coupling between surface and bulk states. In an advanced version [219] the accordance with the experimental data is improved by employing a more realistic, Gauss-shaped potential.

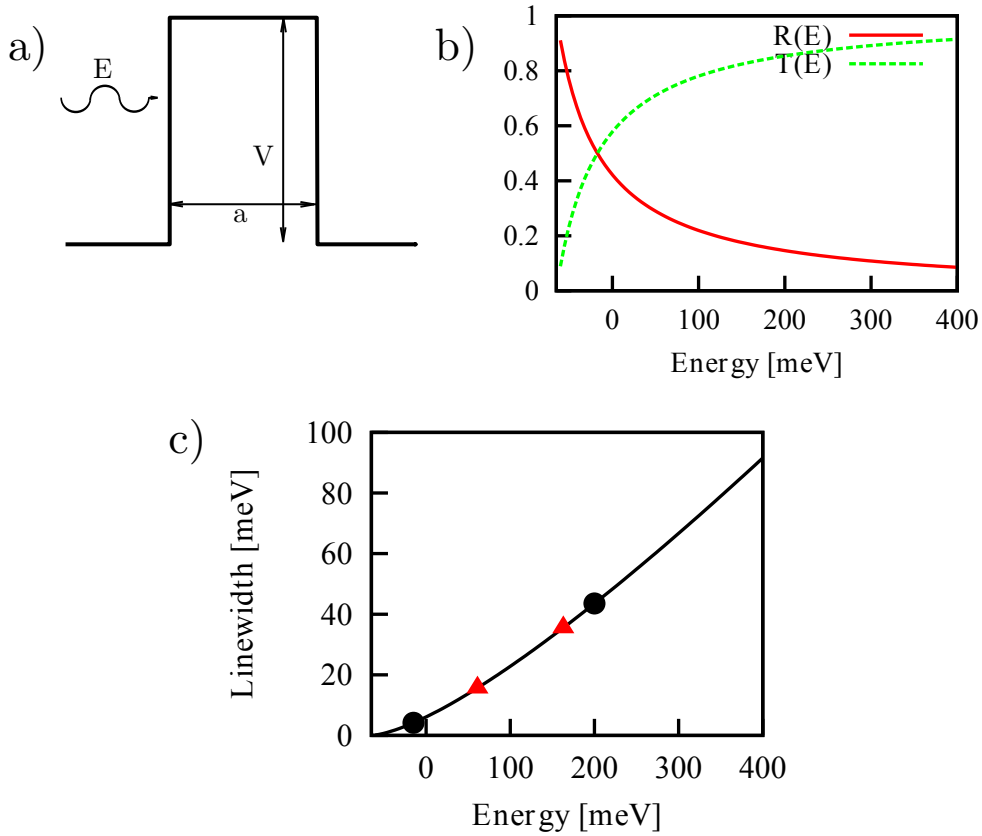

FIGURE 7.3. (a) Sketch of a one-dimensional barrier (height $V = 500$ meV, width $a = 2.5$ Å) used for calculating R and T for an incident wave of energy E. (b) Reflexion (red full) and transmission (green dashed line) coefficients of the 1D barrier. (c) Linewidth as a function of the energy in the approximation of a circular resonator and comparison with the width of the peaks in the BEM-calculated spectra of the isolated system (center position: black dots; halfway position: red triangles).

Next we analyze the influence of periodicity on the confinement characteristics. Properties of periodic structures were calculated in the previous work [63] by using an ornament consisting of several individual quantum wells, requiring a substantial computational effort. The program code used here permits to extend the particle-in-a-box model to infinite 2D systems by defining an elementary cell and using periodic boundary conditions. The first periodic case we employed consists of two potential difference regions and is called the UV-system [Fig. 7.2(b), left panel]. We kept the values for U and V the same as for the case of the island. Therefore any possible changes in the LDOS features will be exclusively related to the introduction of periodicity. The elementary cell is marked with a blue parallelogram with unit vectors $\vec{v}_1 = \begin{pmatrix} D\frac{\sqrt{3}}{2} \\ D/2 \end{pmatrix}$ and $\vec{v}_2 = \begin{pmatrix} 0 \\ D \end{pmatrix}$. Within the EPW code solutions of the Schrödinger equation are represented as a linear combination of plane waves and a satisfactory convergence was achieved with a basis set consisting of 55 vectors. We find that inclusion of periodicity significantly changes the picture of the LDOS distribution. The halfway peak at 60 meV and the central peak at 200 meV are affected most strongly [Fig. 7.2(b)]. The halfway peak is split into two smaller peaks at the energies 46 and 72 meV with similar ρ values. The splitting features can be explained by the interaction between pores. In analogy to the hydrogen molecule, where the interaction between atoms can be seen as a small perturbation, here the penetration of the waves from an arbitrary pore into the neighboring ones represents the perturbation. It lifts up the degeneracy of states within one quantum well, i.e., there is a peak splitting. For the center one the splitting results in maxima at 172 and 218 meV. Contrary to the halfway case the splitting is connected with a remarkable LDOS enhancement for the 218 meV-peak, due to a periodical arrangement of the barriers. The spectra calculated on the barrier and at the corner are still exhibiting small state densities compared to the center and the halfway spectrum apart from the features in the higher energy range ($E > 300$ meV).

To further study metal-organic networks and the influence of cobalt atoms we defined a scattering potential landscape with three constituents, namely the UVW system [Fig. 7.2(c), left panel]. Its geometry is almost the same as that of the UV system; the difference consists of hexagonal entities with the side length d at the corners representing Co atoms. Earlier, the atoms could be well described by the negative scattering barrier of $W = -50$ meV [63]. For the sake of a clearer manifestation of the quantum phenomena we here chose $W = -100$ meV. The most striking difference compared to the UV-system consists of additional peaks rising on the attractive scattering centers with the most prominent being located at 34 and 121 meV [Fig. 7.2(c)]. In addition, the fact that the splitting of the halfway peak structure (red crosses) between 0 and 100 meV gets broader is indicative of stronger coupling between neighboring quantum wells. The same argumentation holds for the two higher energy peak sequences originally positioned between 140 and 220 meV and above 260 meV [Fig. 7.2(b), right panel], which are now broadened and exhibit a more complex shape [Fig. 7.2(c), right panel]. For a better understanding of the distribution of the spatially modulated electronic density we calculated 2D LDOS maps [Fig. 7.4] at the eigenenergies E_i indicated by maxima in the spectra shown in Fig. 7.2(b) and (c). The upper row of panels in Fig. 7.4 applies to the UV system, the lower to the UVW one. Each two-dimensional landscape is normalized to the DOS maximum ρ_{max} and the same color scales were used in all panels. The first states depicted in Fig. 7.4(a) and (g), respectively, correspond to the first eigenstate ψ_1 of the isolated island. They are dome-like, exhibiting a strong maximum in the center, that slowly decreases going towards the halfway points and then more quickly to the walls and cobalt sites, there being almost zero. The landscapes at 46 (34) meV and 72 (70) meV are donut-shaped, showing much less maximal intensity and are related to the low- and high-energy peak emerged from the second hexagon eigenstate ψ_2. A very nice illustration of the influence of the regions with positive potential is given in Fig. 7.4(d) and (j). The upper pattern exhibits a very low LDOS, that is minimal at the network corners.

On the other hand, in the lower pattern clear maxima (yellowish corners) exactly at the corners, i.e., cobalt sites, are discernible. Fig. 7.4(e) and (k) are related to the central peaks at 172 meV and 158 meV. The state with the energy of 172 meV does not originate from one single island eigenstate, but it is a linear combination of ψ_3 and ψ_4 (cf. Fig. 7.1(c)) [63]. Its UVW-counterpart [Fig. 7.4(l)] can be seen as a compound of the original state itself and and state which mostly depicts the influence of the cobalt atoms [Fig. 7.4(j)]. The 172 meV and 158 meV modes are characterized by the lowest ρ_{max} of all examples shown in Fig. 7.4. In those modes central and halfway sites are the most noticeable. In the UVW system ρ on the barriers is suppressed by the presence of the cobalt atoms, while exactly on cobalt sites it is enhanced in comparison with UV system. In the last figures in the rows [Fig 7.4 (f) and (l)] the states with the same origin as those in Fig. 7.4 (e) and (k) are shown. Here the DOS is maximal in a very narrow part of the space around the center.

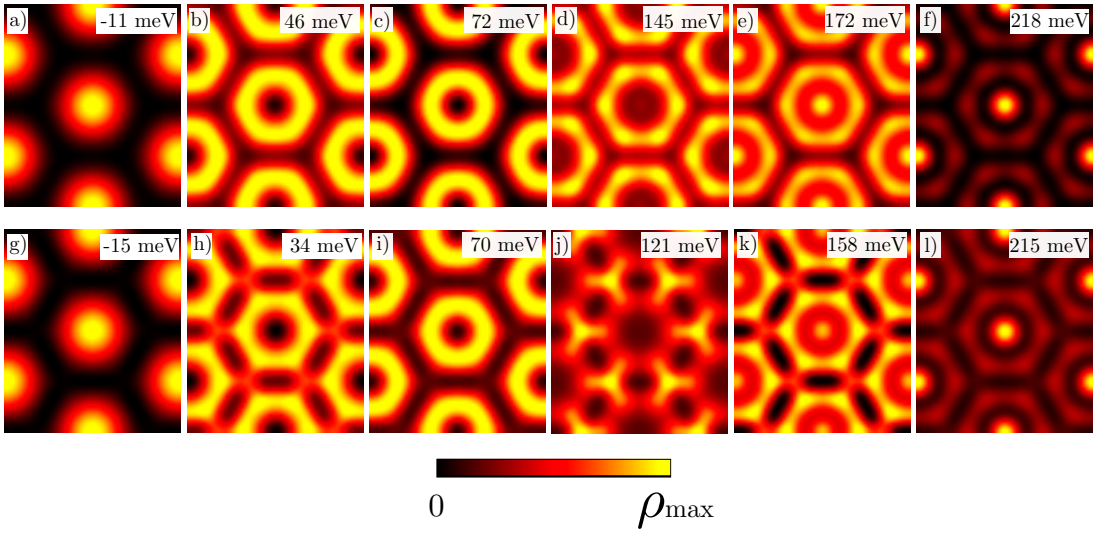

FIGURE 7.4. Two-dimensional landscapes showing spatial distribution of the density of the states for energies at which peaks in the LDOS spectra rise. The upper panel refers to the UV system, the lower to UVW. Maximal intensities ρ_{max} (in $\frac{\text{states}}{\text{eV}\cdot\text{nm}^2}$) are as follows: 16.4, 5.9, 7.7, 5.2, 3.8, 15.2 (UV-system) and 11.1, 4.3, 5.2, 5.4, 3.4 and 11.9 (UVW). The differences between the ρ_{max} corresponding to the 2D landscapes and values from the spectra come from the fact that the LDOS was calculated at the four representative points only and for the given energies ρ_{max} can appear elsewhere inside the barrier.

Furthermore, our investigation was extended to band structure calculations, which have already been performed in similar cases [64, 65]. We start the analysis with the zero-potential approximation, [65] i.e. we consider the geometry of the UV-system, but set V to zero [Fig. 7.5(a)] and then compare the band structure to those calculated for the UV and UVW systems [Fig. 7.5(b)]. The symmetry group is the diperiodic group $Dg80$ (as in graphene [220]) $T \wedge C_{6h}$, where T is the subgroup of 2D translations and C_{6h} the axial point group. Since all relevant conclusions on the electronic structure can be easily transferred to the entire system by the action of the elements of T, without loss of generality, a constraint on the axial point group only is possible. In addition, due to the fact that the horizontal plane is a trivial mirror plane of this structure, we can omit it and the relevant group finally reduces to C_{6v}. Speaking of the electronic properties it is enough to consider the little group of the particular points of the Brillouin zone (BZ). The Γ point, being the center of the BZ has the maximal symmetry C_{6v}. The lowest band starting from -65 meV (the energy of the surface state) is related to the totally symmetrical irreducible representation A_1^+. At the M point (C_{2v}) the lowest energy level is doubly degenerate [Fig. 7.5(a)], thus the corresponding reducible representation can be decomposed as follows: $D^{(M)} = 2A_1^+$. A non-zero scattering potential V will lift this degeneracy and open a gap [denoted with α in Fig. 7.5(b)] at the M point. The stabilizer, sometimes also called a little group, of the K point is C_{3v} and at this point a triplet of states is present in the zero-potential case [Fig. 7.5(a), K point]. The decomposition of this 3D representation is given as $D^{(K)} = A_1 \oplus E$, where E is a 2D irreducible one. Again the finite potential V opens a gap at the K point [β in Fig. 7.5(b)], but the two upper bands still touch each other. The reason for the partial gap opening is that the symmetry of the perturbed system (both UV and UVW) remained unchanged (C_{6v}). Both gaps at the M and K points are induced by the perturbation potential. Additional splitting of the bands can be caused by the symmetry lowering (here C_{3v}), which will be clarified in the discussion below.

By a qualitative inspection of the band structure for both systems one concludes that the bands of the UVW system are systematically shifted downwards with respect to those in the UV system, which is a consequence of employing a negative potential. This affects also a very small gap at the M point. The UV-value of the gap amounts to 53 meV and in the UVW case 38 meV. In addition, the evolution of the split halfway peaks [Fig. 7.2 (b) and (c), right panel] is clearly visible from the band structure point of view. The two peaks are related to the doubly degenerated bands at the Γ point (82 meV) [Fig. 7.5(b) red dashed and green dotted]. The distance between upper and lower band is increased by 10 meV going from UV to UVW system. Another attribute of this picture is that in the range from -100 to 200 meV all bands are linear in the neighborhood of the K point from both sides and have discontinuous derivatives at K point. This behavior is related to a graphene-like dispersion relation shifted above the Fermi level [221].

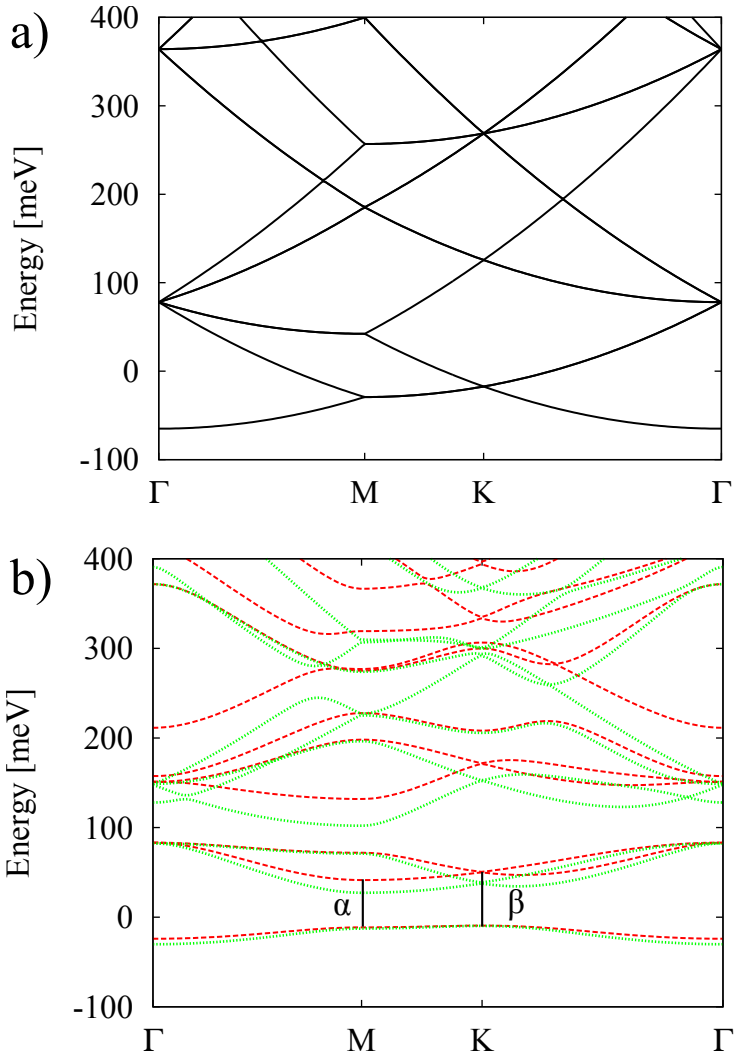

FIGURE 7.5. (a) Band structure of the hexagonal systems in the zero-potential approximation. (b) Bands for the UV system (red dashed) and UVW (green dotted). With α and β the gap at M and K points for the UV system are denoted, respectively.

7.2.1. Dicarbonitrile-pentaphenyl on Cu(111)

In the context of the theoretical investigation of the quantum confinement I extended my calculations to a further honeycomb network formed by dicarbonitrile pentaphenyl ($NC-Ph_5-CN$) on a Cu(111) surface coordinated by Cu atoms. In the original work [215] the network consists of two alternatively placed chiral and non-chiral nodal binding motifs, exhibiting thus threefold C_{3v} symmetry. However, I neglected this small deviation and the system is treated as a perfect hexagonal lattice with a period of 5 nm (experimental value 4.97 ± 0.04 nm) [Fig. 7.6(a)].

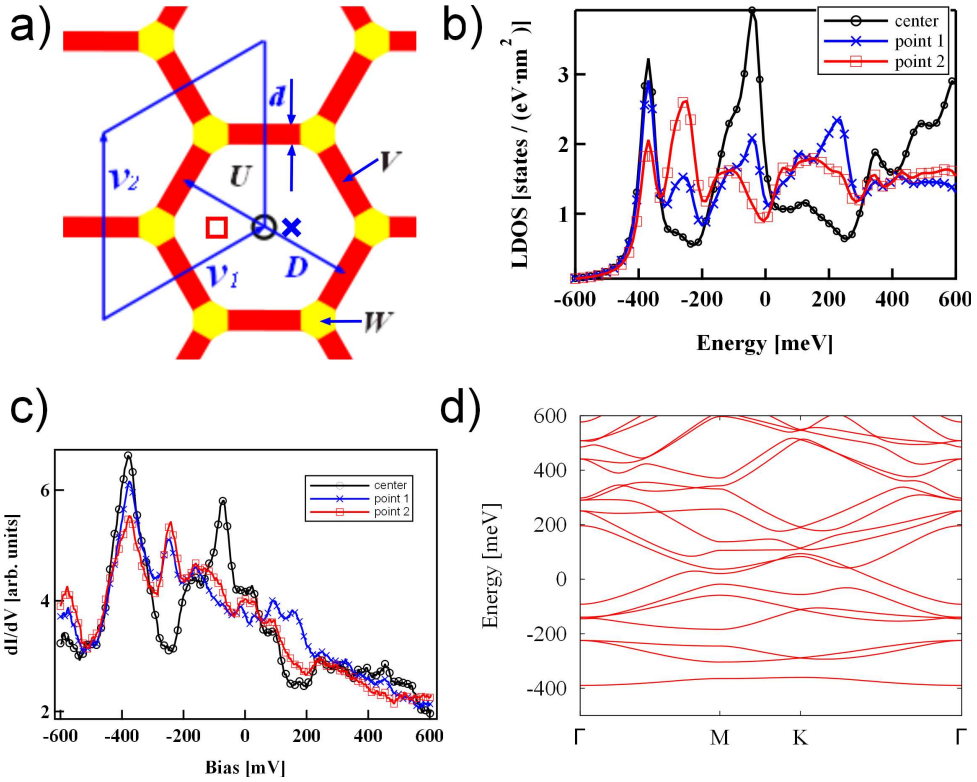

FIGURE 7.6. (a) Geometrical representation of the elementary cell of the UVW system spanning a periodic lattice. The diameter of the pore is $D = 50$ Å, the barrier width $d = 2.5$ Å. Unit vectors are denoted with $\vec{v}_1$ and $\vec{v}_2$. The barrier potentials amount to $\Delta V = 1000$ meV and $U = W = -440$ meV. The points at which the LDOS was calculated are referred to with colored symbols. (b) LDOS calculated at the points defined in the geometrical representation. (c) Curves measured in the experiment by STS. (d) Band structure of the UVW system.

The molecules were represented by barriers of a $\Delta V = 1000$ meV height, while the potential of the atoms was set to the energy of the surface state. Using this configuration the LDOS was calculated [Fig. 7.6(b)] at the points according to the experiment [Fig. 7.6(c)]. The spectrum at the center shows two clear peaks at -370 meV and -42 meV, which compares to the experimental values of -370 meV and -70 meV. The blue and red curve (point 1 and point 2) have peaks at -370 meV and -248 meV (in the experiment -370 meV and -240 meV) with three additional peaks for the point 1, namely, at -42 meV, 115 meV and 235 meV. Measured values lie at -163 meV, 94 and 154 meV. From this comparison it is clear that we see a good agreement with the measured data. The peaks above the Fermi level are shifted upwards, which can be explained by the fact that the interaction between molecular orbitals and metal substrate is very strong above the Fermi level and therefore leads to a DOS enhancement. On the other hand the code employed here does not allow the treatment of this feature. Nevertheless, by comparison measured and simulated values and the shapes of the curves, I assert a good agreement with the experimental data, which means that it was possible to describe the electron confinement both on Ag(111) and Cu(111) surfaces.

I also show the band structure for the considered system [Fig. 7.6(d)], which can be compared to the bands of Cu(111) in zero-potential approximation. The shift of bands upon imposing potentials on the scattering centers and bands splitting are treated in an analogous manner as in the case of network on Ag(111).

7.2.2. Comparison with the ARPES data

In order to round off these considerations I compared band structure calculations with the ARPES measurements and also LDOS curve with measured dI/dV profile. For this purpose I simulated a DPDI (4,9-diaminoperylene-quinone-3,10-diimine) network on Cu(111), which is proven to form a self-assembled array of coupled quantum dots [213]. It is a hexagonal structure

as well, with triangular nodes [222]. The periodicity of the fabricated network was 25.5 Å (corresponding to a $p(10 \times 10)$ superlattice), with a pore diameter of 16 Å. In the original experiment [213] photoemission intensity (PI) was measured and the energy dispersion curve of the surface state was represented by the second derivative of the PI. The surface state band exhibits a width of 80 meV and starts from -220 meV at the Γ point, i.e., it is upshifted by 220 meV with respect to the onset of the Shockley state of the free surface (-440 meV). The energy gap at the M point in this case amounts to 90 meV. The STS dI/dV measurement in the nanopore center has revealed two peaks at -220 meV and 70 meV, where the first one is significantly more pronounced.

In my theoretical approach I defined the geometry of the scattering regions as close to the experimental values as possible. The periodicity remained the same, i.e. 25.5 Å, but instead of the triangular nodal motifs I introduced hexagonal ones with a side length of 5.5 Å. [Fig. 7.7]. The best fit with the experimental data was achieved with a changed effective mass ($m^* = 0.44m_e$ instead of $0.38m_e$ [70]).

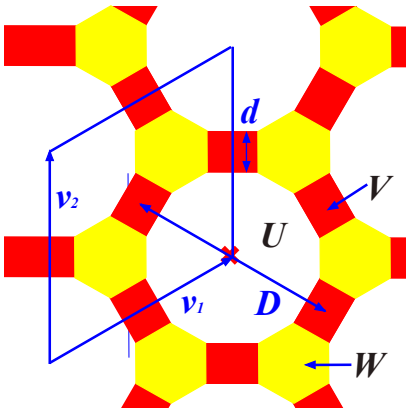

FIGURE 7.7. A hexagonal quantum well with hexagonal regions and the corresponding elementary cell (blue parallelogram). Diameter of the pore is $D = 25.5$ Å, barrier width $d = 5.5$ Å. Unit vectors are denoted with $\vec{v}_1$ and $\vec{v}_2$. The LDOS was calculated in the center (red circle). Different regions are denoted by U, V and W respectively.

The potential of the inner region U was, as in the cases discussed previously, set to the onset energy of the the copper surface state $E_0 =$

−360 meV. We immediately note that this value deviates from the original value of -440 meV [31] Since the Cu(111) surface is more reactive than the Ag(111), higher absolute values for the potentials were employed. The reason for this discrepancy is the temperature dependence of the E_0 [197]. The difference of the barrier potential and U was $V = 1500$ meV and that between the nodes potential and U was $W = -2000$ meV. Note that the negative potential here does not describe attractive metal scattering objects, but it's only the value yielding the best agreement with the experimental data. In the experiment these electron attracting regions are generated by deprotonated amino groups. The bandwidth of 127 meV is slightly overestimated compared to the measured value, whereas the 91 meV band gap is in an excellent agreement with the experimental findings [Fig. 7.8(a)]. The calculated LDOS curve shows also quite reasonable agreement with the spectroscopic signature of the network. The first measured peak at -220 meV is reproduced by one at -200 meV. The second peak from the experiment could not be identified - instead of it a 200 meV bright plateau is observed and a peak at 580 meV. The intensity of the first central peak is definitely the largest. Concerning these inconsistencies, we argue which part of the $\vec{k}$-spectrum was actually sampled with the STM-tip. This could explain the difference to theory [Fig. 7.8(b)], because there all $\vec{k}$-vectors are taken into account.

Results even closer to the measured ones are achieved by varying the effective mass. Employing the parameters $m^* = 0.5m_e$, $V = 1700$ meV and $W = -100$ meV brings us the band gap and band width of 100 meV and the first central peak at -210 meV. However, this is not a realistic model, since the chosen m^* does not have a physical justification.

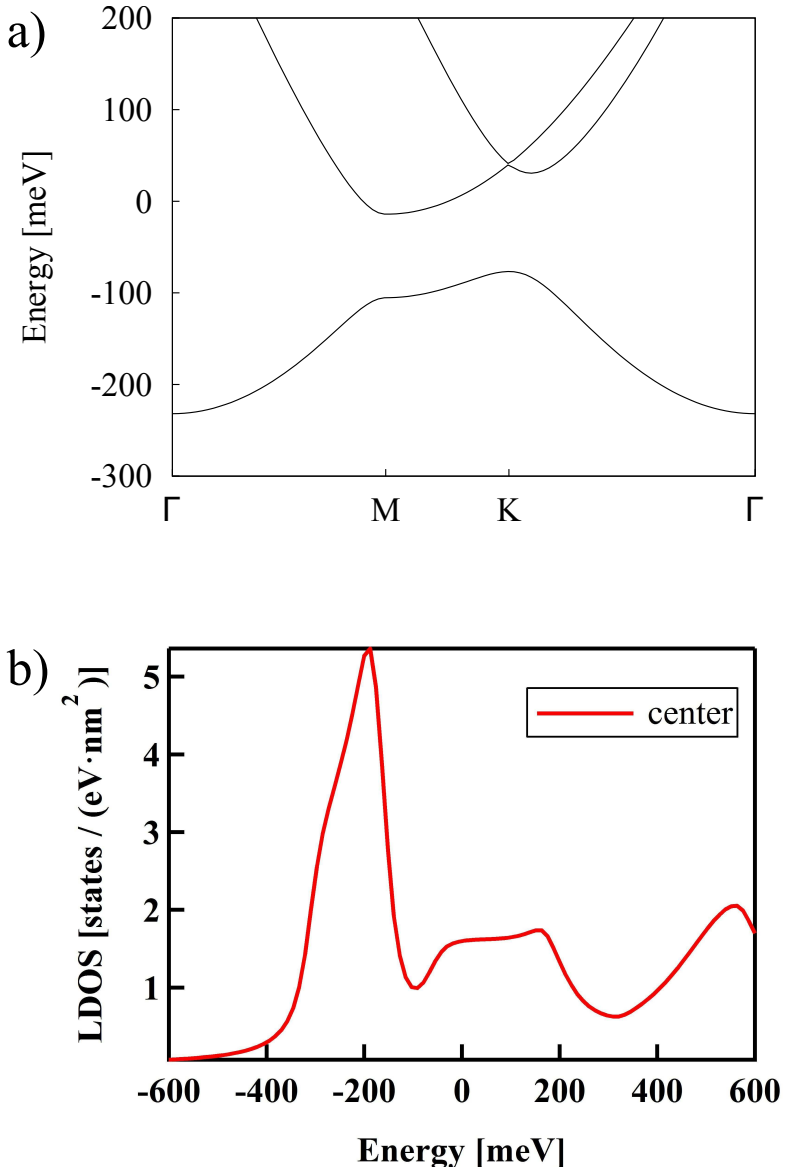

FIGURE 7.8. (a) Band structure of the hexagonal system with hexagonal corner regions. (b) LDOS calculated in the center of the pore.

7.3. Conclusion

In conclusion, I studied the confinement of a nearly free 2D electron gas in two dimensional nanoporous networks, which I could regard as interacting quantum dots. Our theoretical considerations allowed a profound insight into electronic properties of the different systems going from the single islands towards periodical structures with different potential landscapes. I was able to identify three different types of the broadening in the LDOS signature and to relate them to the natural broadening of the spectral lines, transmission coefficient and eventually interaction between pores. The analysis of the pertaining band structures showed that the gap opening at K and M points of the Brillouin zone is perturbation induced. Finally, I demonstrated a comparison with ARPES data and altering of the bands by changing potentials, effective mass and geometry.

8 Summary and Outlook

In this thesis a thorough and systematical investigation of surface-confined open-porous networks with scanning tunneling spectroscopy and BEM, DFT and *ab initio* calculations was presented.

The assembly and dynamics of the bimolecular nano-porous networks consisting of sexiphenyl-dicarbonitrile and N,N'-diphenyl oxalic amide molecules on the Ag(111) surface was studied. The study was performed by means of the STM at low temperature ($T_{substrate}$ = 10 K) and was also corroborated by *ab initio* calculations. The network formation was found to be governed by a two-step assembly protocol involving hierarchic interactions, including a novel carbonitrileoxalic amide bonding motif. The calculations rationalized the network formation and yielded different binding energies for two bonding motifs. In the temperature range above 70 K, weakly bound sexiphenyl-dicarbonitrile molecules carry out one-dimensional diffusion guided by the more stable chaining substructure of the network held together by the carbonitrile-oxalic amide bonding motif. The hopping barrier in the diffusion process and the Arrhenius prefactor were calculated as well and they fit very well in the value range known in the literature.

Furthermore, in the second part of the presented work self-assembly and covalent reactions of TEB and *de novo* synthesized Ext-TEB molecules with terminal alkynes were investigated. It was possible to identify a novel, planar sixfold cyclic binding motif, which is responsible for creation of the long-ranged nanoporous networks. These networks exhibit an organizational chirality. In case of Ext-TEB, an additional open-porous phase was

found to be present, with a three-fold motif. DFT calculations revealed that a very delicate balance between the attractive molecule-molecule interaction and molecule-substrate interaction nests the molecules onto the surface registry and provides a possible explanation why Ext-TEB builds only open phase, and not the dense-packed one. A thermal treatment of the molecules triggered a chemical reaction and a covalent linking of acetylenes was achieved as well, which is a significant success towards fabrication of novel carbon-based nanoarchitectures and two-dimensional materials apart from graphene. A $C_{sp}-H$ bond activation turned out to be Ag surface-mediated and the homo-coupling takes place in the absence of conventionally used transition metal catalysts and with H_2 as only by-product.

In the last part I presented a detailed analysis of the electron confinement in the nanoporous networks with and without metal coordination. The research comprised several different systems, for which LDOS, spatial distribution of DOS and band structures were calculated and the results are in excellent agreement with the existing STM and ARPES data. Concerning calculations only, it was demonstrated how metal scattering centers and non-zero potentials alter bands and lead to a gap opening at special points of the Brillouin zone. Moreover, three types of broadening of the spectral lines could be clearly distinguished. They are attributed to the natural broadening of the lines, different transmission coefficients at different energies and interaction between the pores.

Results shown in this dissertation can be used as an additional motivation for a further research in the area of supramolecular engineering and covalent network formation. In parallel, already successfully employed covalent bonding can be utilized as a binding motif for a variety of other classes of molecules. Bimolecular self-assembly protocols could give new possibilities to guide molecular motion at nanostructured surfaces and so become driving mechanism for nanomachines and motors. On the other

hand, an extensive know-how on theoretical analysis of the electronic properties is useful not only for the analysis of similar systems, but also for prediction, control and tuning of the electronic states in nanocavities.

Acknowledgements

Carrying out this work and subsequently writing this thesis was without a doubt one of the most arduous tasks I have taken. Having said that, one of the joys of having doing this work was the possibility to meet, learn from, enjoy great support, mentoring and encouragement from all the lovely people to be mentioned bellow.

First of all, I would like extend my gratitude to Prof. Dr. Johannes V. Barth for giving me the opportunity to work at the E20, a man who graced me with his ideas, leadership and guidance throughout my stay. I praise the enormous amount of mentoring and teaching by Dr. habil. Florian Klappenberger, who has been an inestimable supervisor for me, directing my research work, helping me to improve my skills in all aspects of my scientific understanding and who went above and beyond to read every line of my papers and thesis in meticulous detail, thus helping me improve skills of putting things in writing. His wide knowledge, patience, devotion and a simple way of explaining complicated concepts are impressive and were always giving me a strong motivation for work. Thanks Flo for the amazing discussions about extracurricular topics as well: Gerhard Polt, differences between the Bayern and the Preußen and explanation of the origin of the Leberkäse. I am also grateful to Dr. Yi-Qi Zhang for fruitful discussions and helping out in the ISL, whenever I needed it.

My thanks are due to Dr. Younes Makoudi, who introduced me to the operation with the STM, as well as Dr. Emmanuel Arras and Dr. Wolfgang Krenner for their expertise, discussions and a great collaboration.

I appreciate the help of Dr. Jonas Björk from the Linköping University in Sweden, whose calculations provided significant contribution to this work, Prof. Dr. Federico Javier García de Abajo from the Facultad de Quimica, San Sebastian, Spain for providing me the EBEM code and introducing to it, and Dr. Mario Ruben and Dr. Svetlana Klyatskaya from the Karlsruhe Institute of Technology (KIT) for the synthesis of the molecules I employed in my experiments.

I would like to thank Kamila Wilson and Viktorija Blaschek, who gave me salary every month, whether it was deserved or not, Max Glanz, the IT wizard and Karl Eberle, Karl Kölbl and Reinhold Schneider, very efficient and prompt technical support team. Thanks for making my life easier in all administrative and technical aspects of my life and work at E20.

It is an often-used cliché, but in this case it is not overstatement to say that the people with whom I spent a great deal of time at the Department were not just working colleagues, but will remain true friends. In this context I would like to name Dr. Sybille Fischer, Dr. Davíd Écija Fernández, Dr. Saranyan Vijaraghavan, Pepe Nacho Urgel, Dr. Katharina Diller, Dr. Carlos-Andres Palma, Dr. Anthoula Papageorgiou, Sushobhan Joshi and Borja Cirera. Of course, I would like to thank all other members of E20 for the support and stimulating working environment.

I would also like to acknowledge Mathilde Dehnert and my spiritual half, Mima Lukić for the encouragement, discussions and support.

Another special thanks goes to Meinhard Holler. Meinhard, danke für deine Unterstützung, lange inspirierende Gespräche über alle möglichen Themen, fürs Bekochtwerden, für die endlosen Sprachstreitereien und dafür, dass Du mir immer zur Seite gestanden bist.

Because she faced the same kind of challenge, big shout to Dr. Marina Marinković for her support, advice, discussions about science and life, and laughing about the PhD Comics.

I am also very grateful to Snežana Turunčić-Dauner, who supported me in the decision to move to Germany and who conveyed the finest details of the German language to me.

I express my deepest gratitude to my parents, Olivera and Miroslav for their infinite love, belief in me, support in my decisions and simply for always being there, not only on good days, but also on tough ones.

And finally, thanks to all of you who read this thesis. If you made it this far, it sure proves you have patience and/or great interest in nanotechnology.

List of publications

- N. Kepčija, F. Klappenberger and J. V. Barth, *Quantum Confinement In 2D Nanoporous Honeycomb Networks At Close-Packed Metal Surfaces.* submitted to Phys. Rev. B , (2013).
- N. Kepčija, Y.-Q. Zhang, M. Kleinschrodt, J. Björk, S. Klyatskaya, F. Klappenberger, M. Ruben and J. V. Barth, *Steering On-Surface Self-Assembly of High-Quality Hydrocarbon Networks with Terminal Alkynes.* J. Phys. Chem. C , 117 3987-3995 (2013).
- Y.-Q. Zhang, N. Kepčija, M. Kleinschrodt, S. Fischer, A.C. Papageorgiou, F. Allegreti, J. Björk, S. Klyatskaya, F. Klappenberger, M. Ruben and J. V. Barth, *Homo-coupling of terminal alkynes on a noble metal surface.* Nat. Commun., 3 1286 (2013).
- W. Krenner, F. Klappenberger, N. Kepčija, E. Arras, Y. Makoudi, D. Kühne, S. Klyatskaya, M. Ruben, M. and J. V. Barth, *Unraveling the Hierarchic Formation of Open-porous Bimolecular Networks.* J. Phys. Chem. C , 116 (31) 16421-16429 (2012).
- Y. Makoudi, E. Arras, N. Kepčija, W. Krenner, S. Klyatskaya, F. Klappenberger, M. Ruben, A. P. Seitsonen, and J. V. Barth, *Hierarchically Organized Bimolecular Ladder Network Exhibiting Guided One-Dimensional Diffusion.* ACS Nano , 6 (1) 549-556 (2012).
- I. Milošević, N. Kepčija, E. Dobardžić, M. Mohr, J. Maultzsch, J. and Thomsen, C. and M. Damnjanović, *Symmetry based analysis of the Kohn anomaly and electron-phonon interaction in graphene and carbon nanotubes.* Phys. Rev. B., 81 (23) 233410 (2010).

Bibliography

[1] R. Feynman. There's a plenty of room at the bottom. *Engineering And Science*, 23(5):22–26, 1960.

[2] K.E. Drexler. *Engines of Creation: The Coming Era of Nanotechnology*. Anchor Books, 1986.

[3] N. Wirth. Program development by stepwise refinement. *Communications of the ACM*, 14(4):221–227, 1971.

[4] J. Hoopes. *False Prophets: The Gurus Who Created Modern Management and Why Their Ideas Are Bad for Business Today*. Basic Books, 2003.

[5] K. E. Drexler and C. Peterson. *Nanotechnology and Enabling Technologies*. Foresight Briefing, 1989.

[6] J. V. Barth, G. Costantini, and K. Kern. Engineering atomic and molecular nanostructures at surfaces. *Nature*, 437(7059):671–679, Sep 2005.

[7] J. V. Barth. Molecular architectonic on metal surfaces. *Annu. Rev. Phys. Chem.*, 58(1):375–407, 2007.

[8] L. J. Prins, D. N. Reinhoudt, and P. Timmerman. Noncovalent synthesis using hydrogen bonding. *Angew. Chem. Int. Ed.*, 40(13):2383–2426, 2001.

[9] J. M. Lehn. Toward complex matter: Supramolecular chemistry and self-organization. *Proc. Natl. Acad. Sci. U. S. A.*, 99(8):4763–4768, Apr 2002.

[10] K. Ariga, M. V. Lee, T. Mori, X. Y. Yu, and J. P. Hill. Two-dimensional nanoarchitectonics based on self-assembly. *Adv. Colloid Interfac*, 154(1-2):20–29, Feb 2010.

[11] S. Griessl, M. Lackinger, M. Edelwirth, M. Hietschold, and W. M. Heckl. Self-assembled two-dimensional molecular host-guest architectures from trimesic acid. *Single Mol.*, 3(1):25–31, 2002.

[12] D. Kühne, F. Klappenberger, R. Decker, U. Schlickum, H. Brune, S. Klyatskaya, M. Ruben, and J. V. Barth. Self-assembly of nanoporous chiral networks with varying symmetry from sexiphenyl-dicarbonitrile on Ag(111). *J. Phys. Chem. C*, 113(41):17851–17859, 2009.

[13] Loshaek S. Narducy K.W., Jahnke R. L. Hydrophilic colored contact lenses, 1989.

[14] V. Balzani, A. Credi, and M. Venturi. Molecular machines working on surfaces and at interfaces. *ChemPhysChem*, 9(2):202–220, Feb 2008.

[15] V. Balzani, A. Credi, F. M. Raymo, and J. F. Stoddart. Artificial molecular machines. *Angew. Chem. - Int. Edn. Eng.*, 39(19):3349–3391, 2000.

[16] M. Fujita, N. Fujita, K. Ogura, and K. Yamaguchi. Spontaneous assembly of ten components into two interlocked, identical coordination cages. *Nature*, 400(6739):52–55, Jul 1 1999.

[17] D. N. Reinhoudt and M. Crego-Calama. Synthesis beyond the molecule. *Science*, 295(5564):2403–2407, Mar 29 2002.

[18] J. Kong, N. R. Franklin, C. Zhou, M. G. Chapline, S. Peng, K. Cho, and H. Dai. Nanotube molecular wires as chemical sensors. *Science*, 287(5453):622–625, 2000.

[19] K. Seufert, W. Auwärter, and J. V. Barth. Discriminative response of surface-confined metalloporphyrin molecules to carbon and nitrogen monoxide. *J. Am. Chem. Soc.*, 132(51):18141–18146, 2010.

[20] O.K. Varghese, P.D. Kichambre, D. Gong, K.G. Ong, E.C. Dickey, and C.A. Grimes. Gas sensing characteristics of multi-wall carbon nanotubes. *Sensor Actuat. B-Chem.*, 81(1):32 – 41, 2001.

[21] N. L. Rosi, J. Eckert, M. Eddaoudi, D. T. Vodak, J. Kim, M. O'Keeffe, and O. M. Yaghi. Hydrogen storage in microporous metal-organic frameworks. *Science*, 300(5622):1127–1129, May 2003.

[22] M. E. Davis. Ordered porous materials for emerging applications. *Nature*, 417(6891):813–821, Jun 2002.

[23] A. Stein. Advances in microporous and mesoporous solids - highlights of recent progress. *Adv. Mater.*, 15(10):763–775, May 2003.

[24] M. Mannini, F. Pineider, P. Sainctavit, C. Danieli, E. Otero, C. Sciancalepore, A. M. Talarico, M.-A. Arrio, A. Cornia, D. Gatteschi, and R. Sessoli. Magnetic memory of a single-molecule quantum magnet wired to a gold surface. *Nat. Mater.*, 8(3):194–197, March 2009.

[25] P. Gambardella, S. Stepanow, A. Dmitriev, J. Honolka, F. M. F. de Groot, M. Lingenfelder, S. Sen Gupta, D. D. Sarma, P. Bencok, S. Stanescu, S. Clair, S. Pons, N. Lin, A. P. Seitsonen, H. Brune, J. V. Barth, and K. Kern. Supramolecular control of the magnetic anisotropy in two-dimensional high-spin fe arrays at a metal interface. *Nat. Mater.*, 8(3):189–193, Mar 2009.

[26] L. Bogani and W. Wernsdorfer. Molecular spintronics using single-molecule magnets. *Nat. Mater.*, 7(3):179–186, March 2008.

[27] E. Arras, A. P. Seitsonen, F. Klappenberger, and J. V. Barth. Nature of the attractive interaction between proton acceptors and organic ring systems. *Phys. Chem. Chem. Phys.*, 14(14):15995–16001, 2012.

[28] Y.-Q. Zhang, N. Kepčija, M. Kleinschrodt, S. Fischer, A. C. Papageorgiou, F. Allegreti, J. Björk, S. Klyatskaya, F. Klappenberger, M. Ruben, and J. V. Barth. Homo-coupling of terminal alkynes on a noble metal surface. *Nat. Commun.*, 3:1286, 2012.

[29] P. Zeppenfeld, C. P. Lutz, and D. M. Eigler. Manipulating atoms and molecules with a scanning tunneling microscope manipulating atoms and molecules with a scanning tunneling microscope. *Ultramicroscopy*, 42:128–133, Jul 1992.

[30] P. O. Gartland and B. J. Slagsvold. Transitions conserving parallel momentum in photoemission from the (111) face of copper. *Phys. Rev. B*, 12:4047–4058, Nov 1975.

[31] M. F. Crommie, C. P. Lutz, and D. M. Eigler. Imaging standing waves in a two-dimensional electron gas. *Nature*, 363(6429):524–527, Jun 1993.

[32] J. T. Li, W. D. Schneider, R. Berndt, and S. Crampin. Electron confinement to nanoscale ag islands on ag(111): A quantitative study. *Phys. Rev. Lett.*, 80(15):3332–3335, Apr 1998.

[33] J. Li, W. D. Schneider, S. Crampin, and R. Berndt. Tunnelling spectroscopy of surface state scattering and confinement. *Surf. Sci.*, 422(1-3):95–106, Feb 1999.

[34] N. Memmel. Monitoring and modifying properties of metal surfaces by electronic surface states. *Surf. Sci. Rep.*, 32(3-4):91–163, 1998.

[35] I. Giaever. Energy gap in superconductors measured by electron tunneling. *Phys. Rev. Lett.*, 5:147–148, Aug 1960.

[36] I. Giaever. Electron tunneling between two superconductors. *Phys. Rev. Lett.*, 5:464–466, Nov 1960.

[37] J. Bardeen, L. N. Cooper, and J. R. Schrieffer. Theory of superconductivity. *Phys. Rev.*, 108:1175–1204, Dec 1957.

[38] J. Bardeen. Tunneling from a many-particle point of view. *Phys. Rev. Lett.*, 6(2):57–59, 1961.

[39] J. Tersoff and D. R. Hamann. Theory of the scanning tunneling microscope. *Phys. Rev. B*, 31(2):805–813, 1985.

[40] J. Tersoff and D. R. Hamann. Theory and application for the scanning tunneling microscope. *Phys. Rev. Lett.*, 50(25):1998–2001, 1983.

[41] N. D. Lang. Vacuum tunneling current from an adsorbed atom. *Phys. Rev. Lett.*, 55(2):230–233, 1985.

[42] N. D. Lang. Theory of single-atom imaging in the scanning tunneling microscope. *Phys. Rev. Lett.*, 56(11):1164–1167, Mar 1986.

[43] J. Winnterlin, J. Wiechers, H. Brune, T. Gritsch, H. Hofer, and Behm R. J. Atomic-resolution imaging of close-packed meta-surfaces by scanning tunneling microscopy. *Phys. Rev. Lett.*, 62(1):59–62, Jan 2 1989.

[44] C. Wöll, S. Chiang, R. J. Wilson, and P. H. Lippel. Determination of atom positions at stacking-fault dislocations on Au(111) by scanning tunneling microscopy. *Phys. Rev. B*, 39(11):7988–7991, Apr 1989.

[45] V. M. Hallmark, S. Chiang, J. F. Rabolt, J. D. Swalen, and R. J. Wilson. Observation of atomic corrugation on Au(111) by scanning tunneling microscopy. *Phys. Rev. Lett.*, 59(25):2879–2882, Dec 21 1987.

[46] C. J. Chen. Origin of atomic resolution on metal-surfaces in scanning tunneling microscopy. *Phys. Rev. Lett.*, 65(4):448–451, Jul 1990.

[47] C.J. Chen. Microscopic view of stm. *J. Vac. Sci. Technol. A*, 9(1):44–50, Jan./Feb. 1991.

[48] W. A. Hofer, A. J. Fisher, R. A. Wolkow, and P. Grutter. Surface relaxations, current enhancements, and absolute distances in high resolution scanning tunneling microscopy. *Phys. Rev. Lett.*, 8723(23):236104, Dec 2001.

[49] J. E. Demuth, U Köhler, and R. J. Hamers. The stm learning-curve and where it may take us. *Journal of Microscopy - Oxford*, 152(2):299–316, Nov 1988.

[50] K. Besocke. An easily operable scanning tunneling microscope. *Surf. Sci.*, 181(1-2):145–153, Mar 1987.

[51] S. Clair. *Investigation of Low-Dimensional Supramolecular Architectures by Low-Temperature Scanning Tunneling Microscopy*. PhD thesis, Ecole Polytechnique Fédérale de Lausanne, 2004.

[52] Wolfgang Krenner. *Supramolecular Templates - Routes Towards Steering Assembly and Electronic Properties at the Nanoscale*. PhD thesis, Technische Universität München, 2012.

[53] P. Hohenberg and W. Kohn. Inhomogeneous electron gas. *Phys. Rev.*, 136:B864–B871, Nov 1964.

[54] G. Kresse and J. Furthmüller. Efficient iterative schemes for ab initio total-energy calculations using a plane-wave basis set. *Phys. Rev. B.*, 54:11169–11186, 1996.

[55] G. Kresse and D. Joubert. From ultrasoft pseudopotentials to the projector augmented-wave method. *Phys. Rev. B.*, 59:1758–1775, 1999.

[56] P. E. Blöchl. Projector augmented-wave method. *Phys. Rev. B.*, 50:17953–17979, 1994.

[57] M. Dion, H. Rydberg, E. Schröder, D. C. Langreth, and B. I. Lundqvist. Van der Waals density functional for general geometries. *Phys. Rev. Lett.*, 92:246401–4, 2004.

[58] J. Klimeš, D. R. Bowler, and A. Michaelides. Van der Waals density functionals applied to solids. *Phys. Rev. B.*, 83:195131–13, 2011.

[59] J. Tersoff and D. R. Hamann. Theory and application for the scanning tunneling microscope. *Phys. Rev. B.*, 50:1998–2001, 1983.

[60] N. Lorente and M. Persson. Theoretical aspects of tunneling-current-induced bond excitation and breaking at surfaces. *Faraday Discuss.*, 117:277–290, 2000.

[61] V. Myroshnychenko, E. Carb-Argibay, I. Pastoriza-Santos, J. Perez-Juste, L. M. Liz-Marzan, and F. J. García de Abajo. Modeling the Optical Response of Highly Faceted Metal Nanoparticles with a Fully 3D Boundary Element Method. *Adv. Mater.*, 20(22):4288–4293, Nov 2008.

[62] F. J. García de Abajo, J. Cordon, M. Corso, F. Schiller, and J. E. Ortega. Lateral engineering of surface states - towards surface-state nanoelectronics. *Nanoscale*, 2(5):717–721, 2010.

[63] F. Klappenberger, D. Kühne, W. Krenner, I. Silanes, A. Arnau, F. J. Garcia de Abajo, S. Klyatskaya, M. Ruben, and J. V. Barth. Tunable quantum dot arrays formed from self-assembled metal-organic networks. *Phys. Rev. Lett.*, 106(2):026802–026802, Jan 2011.

[64] Z. M. Abd El-Fattah, M. Matena, M. Corso, F. J. Garcia de Abajo, F. Schiller, and J. E Ortega. Lifshitz Transition across the Ag/Cu(111) Superlattice Band Gap Tuned by Interface Doping. *Phys. Rev. Lett,*, 107(6):066803, AUG 3 2011.

[65] D. Malterre, B. Kierren, Y. Fagot-Revurat, C. Didiot, F. J. Garcia de Abajo, F. Schiller, J. Cordon, and J. E. Ortega. Symmetry breaking and gap opening in two-dimensional hexagonal lattices. *New J. Phys.*, 13:013026–013026, Jan 2011.

[66] I. Tamm. Possible type of electron-binding on crystal surfaces. *Zeitschrift für Physik*, 76:849–850, 1932.

[67] J Zak. Symmetry criterion for surface-states in solids. *Phys. Rev. B*, 32(4):2218–2226, 1985.

[68] W. Shockley. Surface states associated with a periodic potential. *Phys. Rev.*, 56:317–323, 1939.

[69] S. D. Kevan and R. H. Gaylord. High-resolution photoemission study of the electronic structure of the noble-metal (111) surfaces. *Phys. Rev. B*, 36(11):5809–5818, Oct 1987.

[70] M. F. Crommie, C. P. Lutz, and D. M. Eigler. Confinement of electrons to quantum corrals on a metal surface. *Science*, 262(5131):218–220, Oct 1993.

[71] L. Bürgi, O. Jeandupeux, A. Hirstein, H. Brune, and K. Kern. Confinement of surface state electrons in Fabry-Perot resonators. *Phys. Rev. Lett.*, 81(24):5370–5373, DEC 14 1998.

[72] Y. Pennec, W. Auwärter, A. Schiffrin, A. Weber-Bargioni, A. Riemann, and J. V. Barth. Supramolecular gratings for tuneable confinement of electrons on metal surfaces. *Nat. Nanotechnol.*, 2(2):99–103, Feb 2007.

[73] R. Paniago, R. Matzdorf, G. Meister, and A. Goldmann. Temperature dependence of Shockley-type surface energy bands on Cu(111), Ag(111), Au(111). *Surf. Sci.*, 336(1-2):113–122, AUG 1 1995.

[74] J. S. Lindsey. Self-assembly in synthetic routes to molecular devices - biological principles and chemical perspectives - a review. *New J. Chem.*, 15(2-3):153–180, Feb-Mar 1991.

[75] D. Philp and J. F. Stoddart. Self-assembly in natural and unnatural systems. *Angew. Chem., Int. Ed.*, 35(11):1155–1196, 1996.

[76] J. A. A. W. Elemans, A. E. Rowan, and R. J. M. Nolte. Mastering Molecular Matter. Supramolecular Architectures by Hierarchical Self-Assembly. *J. Mater. Chem.*, 13(11):2661–2670, Nov 2003.

[77] S. De Feyter and F. C. De Schryver. Two-dimensional supramolecular self-assembly probed by scanning tunneling microscopy. *Chem. Soc. Rev.*, 32(6):393–393, Nov 2003.

[78] J. A. A. W. Elemans, S. Lei, and S. De Feyter. Molecular and supramolecular networks on surfaces: From two-dimensional crystal engineering to reactivity. *Angew. Chem., Int. Ed.*, 48(40):7298–7332, 2009.

[79] S. Clair, S. Pons, H. Brune, K. Kern, and J. V. Barth. Mesoscopic metallosupramolecular texturing by hierarchic assembly. *Angew. Chem., Int. Ed.*, 44(44):7294–7297, 2005.

[80] M. C. Blüm, E. Ćavar, M. Pivetta, F. Patthey, and W. D. Schneider. Conservation of chirality in a hierarchical supramolecular self-assembled structure with pentagonal symmetry. *Angew. Chem., Int. Ed.*, 44(33):5334–5337, 2005.

[81] R. Otero, M. Schock, L. M. Molina, E. Laegsgaard, I. Stensgaard, B. Hammer, and F. Besenbacher. Guanine quartet networks stabilized by cooperative hydrogen bonds. *Angew. Chem. Int. Ed.*, 44(15):2270–2275, 2005.

[82] P. A. Staniec, L. M. A. Perdigão, A. Saywell, N. R. Champness, and P. H. Beton. Hierarchical organisation on a two-dimensional supramolecular network. *Chem. Phys. Chem.*, 8(15):2177–2181, Oct 2007.

[83] U. Schlickum, R. Decker, F. Klappenberger, G. Zoppellaro, S. Klyatskaya, W. Auwärter, S. Neppl, K. Kern, H. Brune, M. Ruben, and J. V. Barth. Chiral kagomé lattice from simple ditopic molecular bricks. *J. Am. Chem. Soc.*, 130(35):11778–11782, 2008.

[84] M. Ruben, U. Ziener, J. M. Lehn, V. Ksenofontov, P. Gutlich, and G. B. M. Vaughan. Hierarchical Self-assembly of Supramolecular Spintronic Modules into 1D-and 2D-Architectures with Emergence of Magnetic Properties. *Chem.-Eur. J.*, 11(1):94–100, Dec 2005.

[85] H. Spillmann, A. Dmitriev, N. Lin, P. Messina, J. V. Barth, and K. Kern. Hierarchical assembly of two-dimensional homochiral nanocavity arrays. *J. Am. Chem. Soc.*, 125(35):10725–10728, Sep 2003.

[86] C. Meier, K. Landfester, D. Kunzel, T. Markert, A. Gross, and U. Ziener. Hierarchically self-assembled host-guest network at the solid-liquid interface for single-molecule manipulation. *Angew. Chem.,Int. Edit.*, 47(20):3821–3825, 2008.

[87] M. de Wild, S. Berner, H. Suzuki, H. Yanagi, D. Schlettwein, S. Ivan, A. Baratoff, H. J. Guentherodt, and T. A. Jung. A novel route to molecular self-assembly: Self-intermixed monolayer phases. *ChemPhysChem*, 3(10):881–885, Oct 2002.

[88] M. Ruiz-Osés, N. González-Lakunza, I. Silanes, A. Gourdon, A. Arnau, and J. E. Ortega. Self-assembly of heterogeneous supramolecular structures with uniaxial anisotropy. *J. Phys. Chem. B*, 110(51):25573–25577, Dec 2006.

[89] J. A. Theobald, N. S. Oxtoby, M. A. Phillips, N. R. Champness, and P. H. Beton. Controlling molecular deposition and layer structure with supramolecular surface assemblies. *Nature*, 424(6952):1029–1031, Aug 2003.

[90] M. E. Cañas-Ventura, W. Xiao, D. Wasserfallen, K. Müllen, H. Brune, J. V. Barth, and R. Fasel. Self-assembly of periodic bicomponent wires and ribbons. *Angew. Chem., Int. Ed.*, 46(11):1814–1818, 2007.

[91] E. Barrena, D. G. de Oteyza, H. Dosch, and Y. Wakayama. 2D Supramolecular Self-Assembly of Binary Organic Monolayers. *Chem. Phys. Chem.*, 8(13):1915–1918, Sep 2007.

[92] K. W. Hipps, L. Scudiero, D. E. Barlow, and M. P. Cooke. A self-organized 2-dimensional bifunctional structure formed by supramolecular design. *J. Am. Chem. Soc.*, 124(10):2126–2127, Mar 2002.

[93] F. Klappenberger, M. E. Cañas-Ventura, S. Clair, S. Pons, U. Schlickum, Z. R. Qu, T. Strunskus, A. Comisso, C. Wöll, H. Brune, K. Kern, A. DeVita, M. Ruben, and J. V. Barth. Does the surface matter? Hydrogen bonded chain formation of an oxalic amide derivative in two and three dimensional environment. *Chem. Phys. Chem.*, 9:2522–2530, 2008.

[94] W. Krenner, F. Klappenberger, D. Kühne, K. Diller, Z. R. Qu, M. Ruben, and J. V. Barth. Positioning of single Co atoms steered by a self-assembled organic molecular template. *J. Phys. Chem. Lett.*, 2(13):1639–1645, 2011.

[95] F. Klappenberger, D. Kühne, W. Krenner, I. Silanes, A. Arnau, F. J. Garcia de Abajo, S. Klyatskaya, M. Ruben, and J. V. Barth. Dichotomous array of chiral quantum corrals by a self-assembled nanoporous kagome network. *Nano Lett.*, 9(10):3509–3514, Oct 2009.

[96] W. Krenner, Florian Klappenberger, N. Kepčija, E. Arras, Y. Makoudi, D. Kühne, S. Klyatskaya, M. Ruben, and J. V. Barth. Unraveling the hierarchic formation of open-porous bimolecular networks. *J. Phys. Chem. C*, 116(31):16421–16429, 2012.

[97] N. Henningsen, R. Rurali, K. J. Franke, I. Fernández-Torrente, and J. I. Pascual. Trans to Cis Isomerization of an Azobenzene Derivative on a Cu(100) Surface. *Appl. Phys. A: Mater. Sci. Process.*, 93(2):241–246, Nov 2008.

[98] M. Böhringer, K. Morgenstern, W. D. Schneider, R. Berndt, F. Mauri, A. De Vita, and R. Car. Two-dimensional self-assembly of supramolecular clusters and chains. *Phys. Rev. Lett.*, 83(2):324–327, Jul 1999.

[99] A. Dmitriev, N. Lin, J. Weckesser, J. V. Barth, and K. Kern. Supramolecular Assemblies of Trimesic Acid on a Cu(100) Surface. *J. Phys. Chem. B*, 106(27):6907–6912, Jul 2002.

[100] J. Weckesser, J. V. Barth, and K. Kern. Direct Observation of Surface Diffusion of Large Organic Molecules at Metal Surfaces: PVBA on Pd(110). *J. Chem. Phys.*, 110(11):5351–5354, Mar 1999.

[101] M. E. Cañas-Ventura, F. Klappenberger, S. Clair, S. Pons, K. Kern, H. Brune, T. Strunskus, C. Wöll, R. Fasel, and J. V. Barth. Coexistence of one- and two-dimensional supramolecular assemblies of terephthalic acid on Pd(111) due to self-limiting deprotonation. *J. Chem. Phys.*, 125(18):184710, Nov 2006.

[102] D. Kühne, F. Klappenberger, W. Krenner, S. Klyatskaya, M. Ruben, and J. V. Barth. Rotational and constitutional dynamics of caged supramolecules. *Proc. Natl. Acad. Sci. USA*, 50(107):21332–21336, 2010.

[103] A. E. Baber, H. L. Tierney, and E. C. H. Sykes. A quantitative single-molecule study of thioether molecular rotors. *ACS Nano*, 2(11):2385–2391, 2008.

[104] J. V. Barth, J. Weckesser, C. Cai, P. Günter, L. Bürgi, O. Jeandupeux, and K. Kern. Building supramolecular nanostructures at surfaces by hydrogen bonding. *Angew. Chem., Int. Ed.*, 39(7):1230–1234, 2000.

[105] A. Schiffrin, A. Riemann, W. Auwärter, Y. Pennec, A. Weber-Bargioni, D. Cvetko, A. Cossaro, A. Morgante, and J. V. Barth. Zwitterionic Self-Asembly of l-Methionine Nanogratings on the Ag(111) Surface. *Proc. Natl. Acad. Sci. USA*, 104(13):5279–5284, 2007.

[106] A Schiffrin, J. Reichert, W. Auwärter, G. Jahnz, Y. Pennec, A. Weber-Bargioni, V. S. Stepanyuk, L. Niebergall, P. Bruno, and J. V. Barth. Self-aligning atomic strings in surface-supported biomolecular gratings. *Phys. Rev. B*, 78:035424, Jul 2008.

[107] J. Weckesser, A. De Vita, J. V. Barth, C. Cai, and K. Kern. Mesoscopic correlation of supramolecular chirality in one-dimensional hydrogen-bonded assemblies. *Phys. Rev. Lett.*, 87:096101, Aug 2001.

[108] J. V. Barth, J. Weckesser, G. Trimarchi, M. Vladimirova, A. De Vita, C. Cai, H. Brune, P. Günter, and K. Kern. Stereochemical Effects in Supramolecular Self-Assembly at Surfaces: 1-D versus 2-D Enantiomorphic Ordering for PVBA and PEBA on Ag(111). *J. Am. Chem. Soc.*, 124(27):7991–8000, 2002.

[109] D. C. Senft and G. Ehrlich. Long jumps in the surface-diffusion - one-dimensional migration of isolated adatoms. *Phys. Rev. Lett.*, 74(2):294–297, Jan 1995.

[110] H. Röder, E. Hahn, H. Brune, J. P. Bucher, and K. Kern. Building one-dimensional and 2-dimensional nanostructures by diffusion-controlled aggregation at surfaces. *Nature*, 366(6451):141–143, Nov 1993.

[111] B. G. Briner, M. Doering, H.-P. Rust, and A. M. Bradshaw. Microscopic molecular diffusion enhanced by adsorbate interactions. *Science*, 278(5336):257–260, Oct 1997.

[112] M. Schunack, T. R. Linderoth, F. Rosei, E. Laegsgaard, I. Stensgaard, and F. Besenbacher. Long jumps in the surface diffusion of large molecules. *Phys. Rev. Lett.*, 88(15):156102, Apr 2002.

[113] K. Y. Kwon, K. L. Wong, G. Pawin, L. Bartels, S. Stolbov, and T. S. Rahman. Unidirectional adsorbate motion on a high-symmetry surface: "walking" molecules can stay the course. *Phys. Rev. Lett.*, 95:166101, Oct 2005.

[114] J. Weckesser, J. V. Barth, and K. Kern. Mobility and bonding transition of C_{60} on Pd(110). *Phys. Rev. B*, 64:161403, Sep 2001.

[115] X. Gonze, G.-M. Rignanese, M. Verstraete, J.-M. Beuken, Y. Pouillon, R. Caracas, F. Jollet, M. Torrent, G. Zerah, M. Mikami, Ph. Ghosez, M. Veithen, J.-Y. Raty, V. Olevano, F. Bruneval, L. Reining, R. Godby, G. Onida, D.R. Hamann, D.C. Allan, G. Zerah, F. Jollet, M. Torrent, A. Roy, M. Mikami, Ph. Ghosez, J.-Y. Raty, and D.C. Allan. A brief introduction to the abinit software package. *Zeit. Kristallogr.*, 220:558–562, 2005.

[116] M. Torrent, F. Jollet, F. Bottin, G. Zerah, and X. Gonze. Implementation of the Projector Augmented-Wave Method in the ABINIT code. Application to the study of iron under pressure. *Comput. Mat. Sci.*, 42:337, 2008.

[117] F. Klappenberger, D. Kühne, M. Marschall, S. Neppl, W. Krenner, A. Nefedov, T. Strunskus, K. Fink, C. Wöl, S. Klyatskaya, O. Fuhr, M. Ruben, and J. V. Barth. Uniform π-system alignment in thin films of template-grown dicarbonitrile-oligophenyls. *Adv. Funct. Mater.*, 21(9):1631–1642, 2011.

[118] M. Nishio. CH/π hydrogen bonds in crystals. *Crystengcomm*, 6:130–158, May 2004.

[119] M. Nishio. The CH/π hydrogen bond in chemistry. Conformation, supramolecules, optical resolution and interactions involving carbohydrates. *Phys. Chem. Chem. Phys.*, 13(31):13873–13900, 2011.

[120] T. Steiner. Cooperative C≡C-H$\cdots$C≡C-H interactions - crystal-structure of dl-prop-2-ynylglycine and database study of terminal alkynes. *J. Chem. Soc.-Chem. Commun.*, (1):95–96, Jan 1995.

[121] V. Benghiat and L. Leiserowitz. Molecular packing modes. part viii. crystal and molecular structures of but-3-ynoic acid. *J. Chem. Soc.-Perkin Trans. 2*, (12):1772–1778, 1972.

[122] T. Steiner, E. B. Starikov, A. M. Amado, and J. J. C. Teixeiradias. Weak hydrogen bonding. Part 2. The hydrogen bonding nature of short C-H$\cdots\pi$ contacts: crystallographic, spectroscopic and quantum mechanical studies of some terminal alkynes. *J. Chem. Soc.-Perkin Trans. 2*, (7):1321–1326, Jul 1995.

[123] T. Steiner, E. B. Starikov, and M. Tamm. Weak hydrogen bonding . Part 3. A benzyl group accepting equally strong hydrogen bonds from O-H and C-H donors: 5-ethynyl-5H-dibenzo[a,d]cyclohepten-5-ol. *J. Chem. Soc.-Perkin Trans. 2*, (1):67–71, Jan 1996.

[124] H. C. Weiss, D. Bläser, R. Boese, B. M. Doughan, and M. M. Haley. C-H-π interactions in ethynybenzenes: the crystal structures of ethynylbenzene and 1,3,5-triethynylbenzene, and a redetermination of the structure of 1,4-diethynylbenzene. *Chemm. Commun.*, page 1703, 1997.

[125] J. M. A. Robinson, B. M. Kariuki, R. J. Gough, K. D. M. Harris, and D. Philp. Preferential formation of C≡C-H$\cdots\pi$(C-C) interactions in the solid state. *J. Solid State Chem.*, 134(1):203–206, Nov 1997.

[126] S. Kumar, K. Subramanian, R. Srinivasan, K. Rajagopalan, and T. Steiner. Crystal structure of N-cyano-N-prop-2-ynyl-aniline and structural data on C≡C-H$\cdots$N hydrogen bonds. *J. Mol. Struct.*, 471(1-3):251–255, Nov 1998.

[127] T. Steiner, M. Tamm, A. Grzegorzewski, N. Schulte, N. Veldman, A. M. M. Schreurs, J. A. Kanters, J. Kroon, J. van der Maas, and B. Lutz. Weak hydrogen bonding . part 5. experimental evidence for the long-range nature of C≡C-H$\cdots\pi$ interactions: Crystallographic and spectroscopic studies of three terminal alkynes. *J. Chem. Soc.-Perkin Trans. 2*, (11):2441–2446, Nov 1996.

[128] B. K. Saha and A. Nangia. Ethynyl group as a supramolecular halogen and C equivalent to C-H=C equivalent to C trimer synthon in 2,4,6-tris(4-ethynylphenoxy)-1,3,5-triazine. *Cryst. Growth Des.*, 7(2):393–401, Feb 2007.

[129] G. A. Jeffrey and W. Saenger. *Hydrogen Bonding in Biological Structures*. Springer, Berlin, 1991.

[130] T. Steiner, M. Tamm, B. Lutz, and J. van der Maas. First example of cooperative O-H$\cdots$C C-H Ph hydrogen bonding: Crystalline 7-ethynyl-6,8-diphenyl-7H-benzocyclohepten-7-ol. *Chem. Commun.*, (10):1127–1128, May 1996.

[131] S. Kumar, K. Subramanian, R. Srinivasan, K. Rajagopalan, A. M. M. Schreurs, J. Kroon, G. Koellner, and T. Steiner. N-H$\cdots$C$\equiv$C-H hydrogen bonds as part of cooperative networks: crystal structure of N-(p-methylphenyl)-N-prop-2-ynylurea. *J. Mol. Struct.*, 448(1):51–55, Jul 1998.

[132] D. Philp and J. M. A. Robinson. A computational investigation of cooperativity in weakly hydrogen-bonded assemblies. *J. Chem. Soc.-Perkin Trans. 2*, (7):1643–1650, Jul 1998.

[133] T. Kudernac, S. B. Lei, J. A. A. W. Elemans, and S. De Feyter. Two-dimensional supramolecular self-assembly: nanoporous networks on surfaces. *Chem. Soc. Rev.*, 38(2):402–421, 2009.

[134] M. Furukawa, H. Tanaka, and T. Kawai. Formation mechanism of low-dimensional superstructure of adenine molecules and its control by chemical modification: a low-temperature scanning tunneling microscopy study. *Surf. Sci.*, 445(1):1–10, Jan 2000.

[135] T. Yokoyama, T. Kamikado, S. Yokoyama, and S. Mashiko. Conformation selective assembly of carboxyphenyl substituted porphyrins on Au (111). *J. Chem. Phys.*, 121(23):11993–11997, Dec 2004.

[136] T. Yokoyama, S. Yokoyama, T. Kamikado, Y. Okuno, and S. Mashiko. Selective assembly on a surface of supramolecular aggregates with controlled size and shape. *Nature*, 413(6856):619–621, Oct 2001.

[137] Q. Li, C. B. Han, S. R. Horton, M. Fuentes-Cabrera, B. G. Sumpter, W. C. Lu, J. Bernholc, P. Maksymovych, and M. H. Pan. Supramolecular self-assembly of π-conjugated hydrocarbons via 2D cooperative CH/π interaction. *ACS Nano*, 6(1):566–572, Jan 2012.

[138] G. Polzonetti, V. Carravetta, M. V. Russo, G. Contini, P. Parent, and C. Laffon. Phenylacetylene chemisorbed on Pt (111), reactivity and molecular orientation as probed by NEXAFS. Comparison with condensed multilayer and polyphenylacetylene. *J. Electron Spectrosc. Relat. Phenom.*, 99:175–187, Jan 1999.

[139] G. Iucci, V. Carravetta, P. Altamura, M. V. Russo, G. Paolucci, A. Goldoni, and G. Polzonetti. XPS, NEXAFS and theoretical study of phenylacetylene adsorbed on Cu(100). *Chem. Phys.*, 302(1-3):43–52, Jul 2004.

[140] Y. Sohn, W. Wei, and J. M. White. Phenylacetylene on Cu(111): Adsorption geometry, interfacial electronic structures and thermal chemistry. *J. Phys. Chem. C*, 111(13):5101–5110, Apr 2007.

[141] D. Écija, M. Trelka, C. Urban, P. de Mendoza, E. Mateo-Marti, C. Rogero, J. A. Martin-Gago, A. M. Echavarren, R. Otero, J. M. Gallego, and R. Miranda. Molecular conformation, organizational chirality, and iron metalation of meso-tetramesitylporphyrins on Cu(100). *J. Phys. Chem. C*, 112(24):8988–8994, 2008.

[142] C. Bombis, S. Weigelt, M. M. Knudsen, M. Norgaard, C. Busse, E. Laegsgaard, F. Besenbacher, K. V. Gothelf, and T. R. Linderoth. Steering Organizational and Conformational Surface Chirality by Controlling Molecular Chemical Functionality. *ACS Nano*, 4(1):297–311, 2010.

[143] J. Klimeš, D. R. Bowler, and A. Michaelides. Van der Waals density functionals applied to solids. *Phys. Rev. B*, 83(19):195131, May 2011.

[144] E. Arunan, G. R. Desiraju, A. R. Klein, J. Sadlej, S. Scheiner, I. Alkorta, D. C. Clary, R. H. Crabtree, J. J. Dannenberg, P. Hobza, H. G. Kjaergaard, A. C. Legon, B. Mennucci, and D.J.

Nesbitt. Definition of the hydrogen bond (IUPAC Recommendations 2011). *Pure Appl. Chem.*, 83(8):1637–1641, 2011.

[145] C. Glaser. Beiträge zur Kenntnis des Acetenylbenzols. *Ber. Dtsch. Chem. Ges.*, 2:422, 1896.

[146] W. Chodkiewicz. Synthesis of acetylenic compounds. *Ann. Chim. (Paris)*, 2:819, 1957.

[147] G. Eglinton and A. R. Galbraith. Cyclic diynes. *Chem. Ind.*, 28:737–738, 1956.

[148] A. S. Hay. Oxidative coupling of acetylenes 2. *J.Org.Chem.*, 27:3320–3321, 1962.

[149] F. Sondheimer. Annulenes. 5:81–91, 1972.

[150] F. Diederich. Carbon scaffolding - building acetylenic all-carbon and carbon-rich compounds. *Nature*, 369:199–207, 1994.

[151] U. H. F. Bunz, Y. Rubin, and Y. Tobe. Polyethynylated cyclic π-systems: scaffoldings for novel two and three-dimensional carbon networks. *Chem. Soc. Rev.*, 28:107–119, 1999.

[152] F. Diederich and M. Kivala. All-carbon scaffolds by rational design. *Adv. Mater.*, 22:803–812, 2010.

[153] M. J. Schultz, X. Y. Zhang, S. Unarunotai, D. Y. Khang, Q. Cao, C. J. Wang, C. H. Lei, S. MacLaren, J. A. N. T. Soares, I. Petrov, J. S. Moore, and J. A. Rogers. Synthesis of linked carbon monolayers: Films, balloons, tubes, and pleated sheets. *Proc. Natl. Acad. Sci. USA*, 105:7353–7358, 2008.

[154] J. Méndez, M. F. López, and J. A. Martín-Gago. On-surface synthesis of cyclic organic molecules. *Chem. Soc. Rev.*, 40:4578–4590, 2011.

[155] L. Grill, M. Dyer, L. Lafferentz, M. Persson, M. V. Peters, and S. Hecht. Nano-architectures by covalent assembly of molecular building blocks. *Nat. Nanotechnol.*, 2:687–691, 2007.

[156] R. Gutzler, H. Walch, G. Eder, S. Kloft, W. M. Heckl, and M. Lackinger. Surface mediated synthesis of 2D covalent organic frameworks: 1,3,5-tris(4-bromophenyl)benzene on graphite(001), Cu(111), and Ag(110). *Chem. Commun.*, 29:4456–4458, 2009.

[157] J. A. Lipton-Duffin, J. A. Miwa, M. Kondratenko, F. Cicoira, B. G. Sumpter, V. Meunier, D. F. Perepichka, and F. Rosei. Step-by-step growth of epitaxially aligned polythiophene by surface-confined reaction. *Proc. Natl. Acad. Sci. USA*, 107:11200–11204, 2010.

[158] G. Franc and A. Gourdon. Covalent networks through on-surface chemistry in ultra-high vacuum: state-of-the-art and recent developments. *Phys. Chem. Chem. Phys.*, 13:14283–14292, 2011.

[159] C. A. Palma and P. Samori. Blueprinting macromolecular electronics. *Nat. Chem.*, 3:431–436, 2011.

[160] M. Abel, S. Clair, O. Ourdjini, M. Mossoyan, and L. Porte. Single layer of polymeric fephthalocyanine: An organometallic sheet on metal and thin insulating film. *J. Am. Chem. Soc.*, 133:1203–1205, 2011.

[161] M. Treier, C. A. Pignedoli, T. Laino, R. Rieger, K. Müllen, D. Passerone, and R. Fasel. Surface-assisted cyclodehydrogenation provides a synthetic route towards easily processable and chemically tailored nanographenes. *Nat. Chem.*, 3:61–67, 2011.

[162] D. Y. Zhong, J. H. Franke, S. K. Podiyanachari, T. Blomker, H. M. Zhang, G. Kehr, G. Erker, H. Fuchs, and L. F. Chi. Linear alkane polymerization on a gold surface. *Science*, 334:213–216, 2011.

[163] V. K. Kanuru, G. Kyriakou, S. K. Beaumont, A. C. Papageorgiou, D. J. Watson, and R. M. Lambert. Sonogashira coupling on an extended gold surface in vacuo: Reaction of phenylacetylene with iodobenzene on Au(111). *J. Am. Chem. Soc.*, 132:8081–8086, 2010.

[164] U. Halbes-Letinois, J. M. Weibel, and P. Pale. The organic chemistry of silver acetylides. *Chem. Soc. Rev.*, 36:759–769, 2007.

[165] Y. Yamamoto. Silver-catalyzed C_{sp}-H and C_{sp}-Si bond transformations and related processes. *Chem. Rev.*, 108:3199–3222, 2008.

[166] Z. Ma and F. Zaera. Organic chemistry on solid surfaces. *Surf. Sci. Rep.*, 61:229–281, 2006.

[167] N. Lin, A. Dmitriev, J. Weckesser, J. V. Barth, and K. Kern. Real-time single-molecule imaging of the formation and dynamics of coordination compounds. *Angew. Chem. Int. Ed.*, 41:4779–4783, 2002.

[168] M. Matena, T. Riehm, M. Stöhr, T. A. Jung, and L. H. Gade. Transforming surface coordination polymers into covalent surface polymers: Linked polycondensed aromatics through oligomerization of N-heterocyclic carbene intermediates. *Angew. Chem. Int. Ed.*, 47:2414–2417, 2008.

[169] D. Heim, K. Seufert, W. Auwarter, C. Aurisicchio, C. Fabbro, D. Bonifazi, and J. V. Barth. Surface-assisted assembly of discrete porphyrin-based cyclic supramolecules. *Nano Lett.*, 10:122–128, 2010.

[170] N. Lin, D. Payer, A. Dmitriev, T. Strunskus, C. Wöll, J. V. Barth, and K. Kern. Two-dimensional adatom gas bestowing dynamic heterogeneity on surfaces. *Ang. Chem. Int. Ed.*, 44:1488–1491, 2005.

[171] X. L. Zhou, J. M. White, and B. E. Koel. Chemisorption of atomic-hydrogen on clean and Cl-covered Ag(111). *Surf. Sci.*, 218:201–210, 1989.

[172] M. T. Nguyen, C. A. Pignedoli, and D. Passerone. An ab initio insight into the Cu(111)-mediated Ullmann reaction. *Phys. Chem. Chem. Phys.*, 13:154–160, 2011.

[173] A. E. King, L. M. Huffman, A. Casitas, M. Costas, X. Ribas, and S. S. Stahl. Copper-catalyzed aerobic oxidative functionalization of an arene C-H bond: Evidence for an aryl-copper(III) intermediate. *J. Am. Chem. Soc.*, 132:12068–12073, 2010.

[174] J. Björk, S. Strafström, and F. Hanke. Zipping up: Cooperativity drives the synthesis of graphene nanoribbons. *J. Am. Chem. Soc.*, 133:14884–14887, 2011.

[175] G. Henkelman, B. Uberuaga, and H. Jónsson. A climbing image nudged elastic band method for finding saddle points and minimum energy paths. *J. Chem. Phys.*, 113:9901–9904, 2000.

[176] G. Henkelman and H. Jónsson. A dimer method for finding saddle points on high dimensional potential surfaces using only first derivatives. *J. Chem. Phys.*, 111:7010–7022, 1999.

[177] J. Kästner and P. Sherwood. Superlinearly converging dimer method for transition state search. *J. Chem. Phys.*, 128:014106–014111, 2008.

[178] M. Bieri, M. T. Nguyen, O. Groning, J. M. Cai, M. Treier, K. Ait-Mansour, P. Ruffieux, C. A. Pignedoli, D. Passerone, M. Kastler, K. Mullen, and R. Fasel. Two-dimensional polymer formation on surfaces: Insight into the roles of precursor mobility and reactivity. *J. Am. Chem. Soc.*, 132:16669–16676, 2010.

[179] L. Lafferentz, V. Eberhardt, C. Dri, C. Africh, G. Comelli, F. Esch, S. Hecht, and L. Grill. Controlling on-surface polymerization by hierarchical and substrate-directed growth. *Nat. Chem.*, 4:215–220, 2012.

[180] O. Ourdjini, R. Pawlak, M. Abel, S. Clair, L. Chen, N. Bergeon, M. Sassi, V. Oison, J. M. Debierre, R Coratger, and L. Porte. Substrate-mediated ordering and defect analysis of a surface covalent organic framework. *Phys. Rev. B.*, 84:125421–(1–9), 2011.

[181] J. Sakamoto, J. van Heijst, O. Lukin, and A. D. Schlüter. Two-dimensional polymers: Just a dream of synthetic chemists? 48:1030–1069, 2009.

[182] J. A. Rogers, M. G. Lagally, and R. G. Nuzzo. Synthesis, assembly and applications of semiconductor nanomembranes. *Nature*, 477:45–53, 2011.

[183] W. Eck, A. Kuller, M. Grunze, B. Volkel, and A. Golzhauser. Freestanding nanosheets from crosslinked biphenyl self-assembled monolayers. *Adv. Mater.*, 17:2583–2587, 2005.

[184] P. Kissel, R. Erni, W. B. Schweizer, M. D. Rossell, B. T. King, T. Bauer, S. Götzinger, A. D. Schlüter, and J. Sakamoto. A two-dimensional polymer prepared by organic synthesis. *Nat. Chem.*, 4:287–291, 2012.

[185] H. Kung, S. M. Wu, Y. J. Wu, Y. W. Yang, and C. M. Chiang. Tracking the chemistry of unsaturated C_3H_3 groups adsorbed on a silver surface: Propargyl-allenyl-acetylide triple bond migration, self-hydrogenation, and carbon-carbon bond formation. *J. Am. Chem. Soc.*, 130:10263–10273, 2008.

[186] L. Köhler and G. Kresse. Density functional study of CO on Rh(111). *Phys. Rev. B.*, 70:165405–(1–9), 2004.

[187] A. C. Papageorgiou, S. Fischer, J. Reichert, K. Diller, F. Blobner, F. Klappenberger, F. Allegretti, A. P. Seitsonen, and J. V. Barth. Chemical transformations drive complex self-assembly of uracil on close-packed coinage metal surfaces. *ACS Nano*, 6:2477–2486, 2012.

[188] M. Matena, M. Stöhr, T. Riehm, J. Björk, S. Martens, M. S. Dyer, M. Persson, J. Lobo-Checa, K. Müller, M. Enache, H. Wadepohl, J. Zegenhagen, T. A. Jung, and L. H. Gade. Aggregation and contingent metal/surface reactivity of 1,3,8,10-tetraazaperopyrene (TAPP) on Cu(111). *Chem. Eur. J.*, 16:2079–2091, 2010.

[189] K. Judai, A. S. Worz, S. Abbet, J. M. Antonietti, U. Heiz, A. Del Vitto, L. Giordano, and G. Pacchioni. Acetylene trimerization on Ag, Pd and Rh atoms deposited on MgO thin flms. *Phys. Chem. Chem. Phys.*, 7:955–962, 2005.

[190] R. J. Lagow, J. J. Kampa, H. C. Wei, S. L. Battle, J. W. Genge, D. A. Laude, C. J. Harper, R. Bau, R. C. Stevens, J. F. Haw, and E. Munson. Synthesis of linear acetylenic carbon - the sp carbon allotrope. *Science*, 267:362–367, 1995.

[191] W. A. Chalifoux and R. R. Tykwinski. Synthesis of polyynes to model the sp-carbon allotrope carbyne. *Nat. Chem.*, 2:967–971, 2010.

[192] E. Weber, M. Hecker, E. Koepp, W. Orlia, M. Czugler, and I. Csoregh. New trigonal lattice hosts: stoicheiometric crystal inclusions of laterally trisubstituted benzenes - x-ray crystal structure of 1,3,5-tris-(4-carboxyphenyl)benzene-dimethylformamide. *J. Chem. Soc., Perkin. Trans.*, 2:1251–1257, 1988.

[193] F. Klappenberger, D. Kühne, W. Krenner, I. Silanes, A. Arnau, F. J. García de Abajo, S. Klyatskaya, M. Ruben, and J. V. Barth. Tunable quantum dot arrays formed from self-assembled metal-organic networks. *Phys. Rev. Lett.*, 106:026802, Jan 2011.

[194] N. Kepčija, F. Klappenberger, and J. V. Barth. Quantum confinement in 2D nanoporous honeycomb networks at close-packed metal surfaces. *submitted*, 100:123–456, 2013.

[195] J. T. Li, W. D. Schneider, R. Berndt, O. R. Bryant, and S. Crampin. Surface-state lifetime measured by scanning tunneling spectroscopy. *Phys. Rev. Lett.*, 81(20):4464–4467, Nov 1998.

[196] F. Reinert, G. Nicolay, S. Schmidt, D. Ehm, and S. Hufner. Direct measurements of the L-gap surface states on the (111) face of noble metals by photoelectron spectroscopy. *Phys. Rev. B.*, 63(11):115415–115415, Mar 15 2001.

[197] R. Paniago, R. Matzdorf, G. Meister, and A. Goldmann. Temperature dependence of Shockley-type surface energy bands on Cu(111), Ag(111) and Au(111). *Surf. Sci.*, 336(1-2):113–122, Aug 1995.

[198] Y. Hasegawa and P. Avouris. Direct observation of standing-wave formation at surface steps using scanning tunneling spectroscopy. *Phys. Rev. Lett.*, 71(7):1071–1074, AUG 16 1993.

[199] J. T. Li, W. D. Schneider, and R. Berndt. Local density of states from spectroscopic scanning-tunneling-microscope images: Ag(111). *Phys. Rev. B*, 56(12):7656–7659, Sep 1997.

[200] E. J. Heller, M. F. Crommie, C. P. Lutz, and D. M. Eigler. Scattering and absorption of surface electron waves in quantum corrals. *Nature*, 369(6480):464–466, Jun 1994.

[201] K. F. Braun and K. H. Rieder. Engineering electronic lifetimes in artificial atomic structures. *Phys. Rev. Lett.*, 88(9):096801–096801, Mar 4 2002.

[202] J. Kliewer, R. Berndt, and S. Crampin. Controlled modification of individual adsorbate electronic structure. *Phys. Rev. Lett.*, 85(23):4936–4939, DEC 4 2000.

[203] M. C. Barr, M. P. Zaletel, and E. J. Heller. Quantum corral resonance widths: Lossy scattering as acoustics. *Nano Lett.*, 10(9):3253–3260, 2010.

[204] A. Singha, M. Gibertini, B. Karmakar, S. Yuan, M. Polini, G. Vignale, M. I. Katsnelson, A. Pinczuk, L. N. Pfeiffer, K. W. West, and V. Pellegrini. Two-dimensional mott-hubbard electrons in an artificial honeycomb lattice. *Science*, 332(6034):1176–1179, JUN 3 2011.

[205] H. C. Manoharan, C. P. Lutz, and D. M. Eigler. Quantum mirages formed by coherent projection of electronic structure. *Nature*, 40(6769):512–515, FEB 3 2000.

[206] A. A. Correa, F. A. Reboredo, and C. A. Balseiro. Quantum corral wave-function engineering. *Phys. Rev. B*, 71(3):035418–035418, Jan 2005.

[207] G. A. Fiete and E. J. Heller. Colloquium: Theory of quantum corrals and quantum mirages. *Rev. Mod. Phys.*, 75(3):933–948, JUL 2003.

[208] R. Stiufiuc, L. M. A. Perdigão, B. Grandidier, D. Deresmes, G. Allan, C. Delerue, D. Stievenard, P. H. Beton, S. C. Erwin, M. Sassi, V. Oison, and J. M. Debierre. Above-barrier surface electron resonances induced by a molecular network. *Phys. Rev. B*, 81(4):045421–5, JAN 2010.

[209] C. F. Hirjibehedin, C. P. Lutz, and A. J. Heinrich. Spin coupling in engineered atomic structures. *Science*, 312(5776):1021–1024, MAY 19 2006.

[210] A Mugarza and JE Ortega. Electronic states at vicinal surfaces. *J. Phys.: Condens. Matter*, 15(47):S3281–S3310, DEC 3 2003.

[211] A. Mugarza, A. Mascaraque, V. Perez-Dieste, V. Repain, S. Rousset, F. J. G. de Abajo, and J. E. Ortega. Electron confinement in surface states on a stepped gold surface revealed by angle-resolved photoemission. *Phys. Rev. Let.*, 87(10):107601, SEP 3 2001.

[212] L Gross, F Moresco, L Savio, A Gourdon, C Joachim, and KH Rieder. Scattering of surface state electrons at large organic molecules. *Phys. Rev. Lett.*, 93(5):056103–056103, JUL 30 2004.

[213] J. Lobo-Checa, M. Matena, K. Müller, J. H. Dil, F. Meier, L. H. Gade, T. A. Jung, and M. Stöhr. Band formation from coupled quantum dots formed by a nanoporous network on a copper surface. *Science*, 325(5938):300–303, Jul 2009.

[214] Zh. Cheng, J. Wyrick, M. Luo, D. Sun, D. Kim, Y. Zhu, W. Lu, K. Kim, T. L. Einstein, and L. Bartels. Adsorbates in a box: Titration of substrate electronic states. *Phys. Rev. Lett.*, 105(6):066104, AUG 6 2010.

[215] M. Pivetta, Giulia E. Pacchioni, U. Schlickum, J. V. Barth, and H. Brune. Formation of Fe Cluster Superlattice in a Metal-Organic Quantum-Box Network. *Phys. Rev. Lett.*, 110(8):086102, FEB 19 2013.

[216] S. Gasiorowicz. *Quantum physics*. John Wiley & Sons, 2003.

[217] S. Crampin, H. Jensen, J. Kröger, L. Limot, and R. Berndt. Resonator design for use in scanning tunneling spectroscopy studies of surface electron lifetimes. *Phys. Rev. B*, 72(3):035443–035443, Jul 2005.

[218] H. K. Harbury and W. Porod. Elastic scattering theory for electronic waves in quantum corrals. *Phys. Rev. B*, 53(23):15455–15458, JUN 15 1996.

[219] A.I. Rahachou and I.V. Zozoulenko. Elastic scattering of surface electron waves in quantum corrals: Importance of the shape of the adatom potential. *Phys. Rev. B*, 70:233409–1–4, 15 Dec. 2004.

[220] E.A. Wood. The 80 diperiodic groups in three dimensions. *Bell Syst. Tech. J.*, 43:541–559, 1964.

[221] J. Peng and S. S. Li. Band structures of graphene hexagonal lattice semiconductor quantum dots. *Appl. Phys. Lett.*, 97(24):242105–242105, DEC 13 2010.

[222] M. Stöhr, M. Wahl, C. H. Galka, T. Riehm, T. A. Jung, and L. H. Gade. Controlling molecular assembly in two dimensions: The concentration dependence of thermally induced 2d aggregation of molecules on a metal surface. *Angew. Chem. Int. Ed.*, 44(45):7394–7398, 2005.